

## MULTICHANNEL SQUID BIOMAGNETIC SYSTEMS

JIRI VRBA

*CTF Systems Inc.*

*15-1750 McLean Ave, Port Coquitlam, B.C., Canada, V3C 1M9*

**Abstract.** The field of biomagnetism advanced considerably since the first recordings of magnetic fields of the human heart in 1963 and of the human brain in 1968. Since the introduction of whole-cortex magnetoencephalography (MEG) systems in 1992, the number of installed channels has dramatically increased, and the magnetic evaluation of the human brain has been gradually finding its place in clinical work. MEG is presently the most important biomagnetic application, and sophisticated MEG systems with large numbers of channels have been developed commercially. The MEG systems must meet certain specifications on noise, dynamic range, slew rate and linearity because they are exposed to environmental noise even when they are operated within shielded rooms. The systems are designed to meet these specifications through optimized design of SQUID flux transformers, SQUID control electronics and data acquisition, and development of various synthetic noise cancellation techniques. The interpretation of the resulting magnetic data is enhanced by combining the MEG results with information from electroencephalography (EEG) and other imaging modalities. In addition, an engineering effort is devoted to the development of various items of MEG peripheral equipment (stimulators, patient support, head positioning, etc.).

*Table of contents:*

1. Introduction
2. MEG and EEG signals
3. General structure and configuration of biomagnetic systems
4. Noise and noise cancellation in biomagnetic measurements
  - 4.1. *Noise description*
  - 4.2. *Shielding of environmental noise*
  - 4.3. *Active noise cancellation*
  - 4.4. *Synthetic noise cancellation*
  - 4.5. *Sensor space filtering*
5. Character and acquisition of biomagnetic data
6. Flux transformers for biomagnetic sensors
  - 6.1. *Method of sensor comparison*
  - 6.2. *Radial and vector magnetometers*
  - 6.3. *Radial gradiometers*
  - 6.4. *Radial and planar gradiometers*
  - 6.5. *Conclusions of sensor discussion*
7. Miscellaneous system considerations
8. Examples of MEG applications
9. Conclusions
  - Acknowledgment
  - References

## 1. Introduction

The detection of the electromagnetic activity of the human heart and brain has a long history. The first known recording of the human electrocardiogram (ECG) was reported in 1887 [1], and more extensive recordings were made early in the 20th century after the perfection of the string galvanometer [2]. However, it took nearly 80 years after the first reported ECG before the first magnetocardiogram (MCG) was recorded using conventional coils with large numbers of turns [3]. Similarly, the electroencephalogram (EEG) was discovered in 1929 [4] and its magnetic counterpart, the magnetoencephalogram (MEG) was first recorded about 40 years later in 1968 using room-temperature coils [5].

In order to perform more detailed measurements of biomagnetic fields, more sensitive instruments were needed. The significant increase in sensitivity was made possible by the Nobel-prize-winning discovery of the Josephson effect in 1962 [6] and the subsequent development of highly sensitive detectors of magnetic field, called SQUIDs (Superconducting QUantum Interference Devices) [7 - 11] in 1964. SQUIDs were first used for detection of MCG in 1970 [12], and for detection of MEG in 1972 [13].

The time-line of the ECG/MCG and EEG/MEG history is shown in Figure 1.1. The first magnetic recordings with superconducting SQUID detectors were made using simple systems consisting of one or a few channels, and it was about two decades later before the present multi-channel systems were developed.

Since the first recordings of the magnetic fields of the human heart and brain were made by SQUID detectors, magnetic fields were detected from numerous other body organs, for example from the eye (magnetooculogram and magnetoretinogram), the stomach (magnetogastrogram, MGG), the small intestine (magnetoenterogram, MENG), the skeletal muscle (magnetomyogram, MMG), the peripheral nerves (magnetoneurogram, MNG), the fetal heart (fMCG), the fetal brain (fMEG), the lungs (magnetopneurogram), etc. The biomagnetic fields range from 10 fT for the spinal chord to more than a nT for magnetized lungs, and the frequency range is from less than 0.1 Hz to several hundreds of Hz [14, 15] - see Figure 1.2.

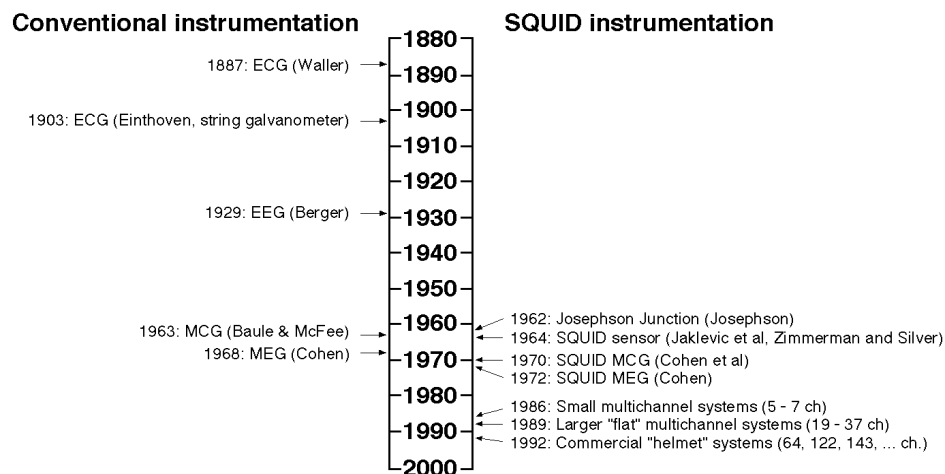


Figure 1.1. Time-line of the history of biomagnetism.

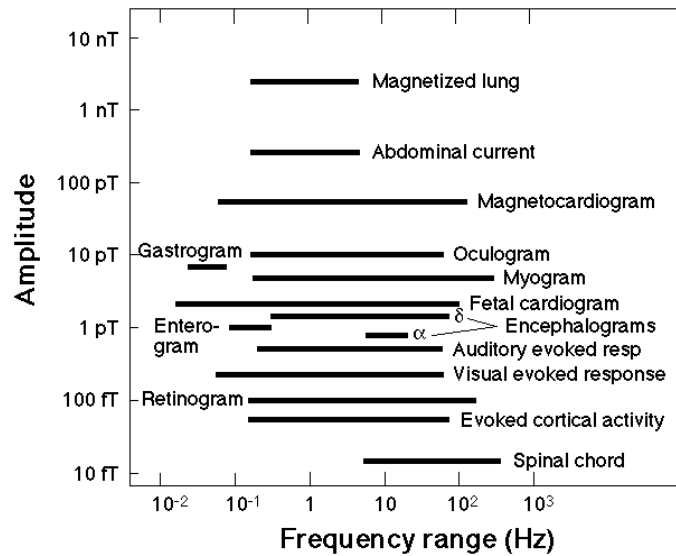


Figure 1.2. Representative biomagnetic fields and their frequency ranges. From references [14 and 15].

Even though magnetic fields were detected from many organs, so far the most important application of biomagnetism has been to the brain, and MEG recordings have been gradually moving from research laboratories to clinical practice. Examples of clinical or near-clinical applications are use of MEG in pre-surgical mapping [16], localization of epileptic seizure foci [17], and the detection of abnormal slow waves associated with stroke, head trauma, and transient ischemic attack in the brain [18-21].

Since MEG is presently the most important biomagnetic application, and since it encompasses the smallest signal range and a large span of frequencies, it will be used as a model for discussion of biomagnetic systems - problems and technological solutions for other biomagnetic applications are similar to that encountered in MEG. MEG also has spurred intensive technological development in the commercial sector, which has led to the development of sophisticated MEG systems with large numbers of channels which cover the whole head surface. These helmet systems became commercially available in 1992 [22, 23, 24]. Presently, there are three commercial suppliers of MEG systems in Europe and North America (Biomagnetic Technologies, Inc. [25], CTF Systems, Inc. [26] and Neuromag Ltd. [27]), and approximately 30 whole-head systems have been sold worldwide to date.

The introduction of the helmet-type MEG systems has led to a dramatic increase in the use of SQUID sensors. It is estimated that the present number of SQUID sensors in the commercially-sold whole-cortex MEG systems is approximately 4,300. This number should be put into perspective by considering that before 1992 (a period of 22 years since 1970 when the first SQUID recording of the magnetic field of human heart was made) the total number of functional SQUIDs in all applications was only slightly more than 1,000 [15]. Even though the SQUID sensors and superconducting components are the "enabling" devices for biomagnetism, and without them the detection of small magnetic fields would not be possible, they constitute only a small part of the

overall cost of the present MEG systems (about 3 to 4 %), while the cost of nonsuperconducting components (cryogenics, electronics, software, peripheral equipment and shielding) is dominant.

Currently, all commercial MEG systems are based on low-temperature SQUIDS, however, systems based on high-temperature superconductors also are being developed. Even though the present high-temperature SQUIDS are not as reliable and sensitive as their low-temperature counterparts, their performance is steadily improving, and they are already suitable for some applications.

In addition to commercial activity, SQUID biomagnetometers with large numbers of channels have been constructed in a number of laboratories world-wide using both low- and high-temperature superconductors. A few examples, not intended to be exhaustive, of such systems based on low-temperature superconductors and cooled by liquid helium are: 19-channel system developed at the University of Twente [30], a double 14-channel system developed by Dornier [31, 32], a 19-channel system build by the Russian company, Cryoton [33], an 83-channel system developed at PTB Berlin [34], a double 31-channel system built by Philips [35], a double 37-channel system commercially produced by BTi [25], a 129-channel system by Shimadzu [36], a 128-channel system developed by the Superconducting Sensor Laboratory in Japan [37]; systems based on low-temperature sensors, but cooled by cryocoolers: 32- and 61-channel systems by Daikin Industries Ltd. [38, 39]; and systems based on high-temperature superconductors and cooled by liquid nitrogen: e.g., a 32-channel system by a Japanese group [40].

The MEG system measures magnetic fields on the head surface. However, to the user, the more relevant information is the current distribution in the brain responsible for the measured fields. Unfortunately, the field inversion problem is ill-posed - the inversion is not unique - and the MEG data must be supplemented by additional information or additional physiological constraints, or the mathematical source models must be simplified.

One way to supply more useful information is to use also the EEG [28], an older electrical counterpart of MEG. Both MEG and EEG measure the same sources of neuronal activity, and their information is complementary and additive [29]. For these reasons, EEG is usually also included as a part of a biomagnetic system. Additional information to assist the field inversion also can be supplied by other imaging techniques. For structural information one uses the brain atlas [41], magnetic resonance imaging (MRI, [43-47]), and computed axial tomography (CAT or CT, [42]); for functional information one uses positron emission tomography (PET, [48, 49]), single photon emission computed tomography (SPECT, [48 - 50]), and functional MRI (fMRI, [43, 49, 51-53]).

MEG and EEG provide a direct measure of neuronal electrical activity with excellent temporal resolution, but spatial characterization is dependent on a non-unique inverse problem. MRI and CT provide high-resolution volumetric data defining anatomy, and PET, SPECT, and fMRI provide a 3-dimensional representation of functional activity in the brain in terms of metabolic and hemodynamic variables. In comparison with MEG and EEG, the PET, SPECT and fMRI are limited by the slow time-course of the metabolic and hemodynamic processes, and by the poorly defined relationship between them and neural activation.

A comparison of temporal and spatial resolutions of various imaging methods is shown in Figure 1.3. CT and MRI provide the best spatial resolutions ( $\approx 1$  mm), but they can be used only for the determination of anatomical structures. MEG, fMRI, and

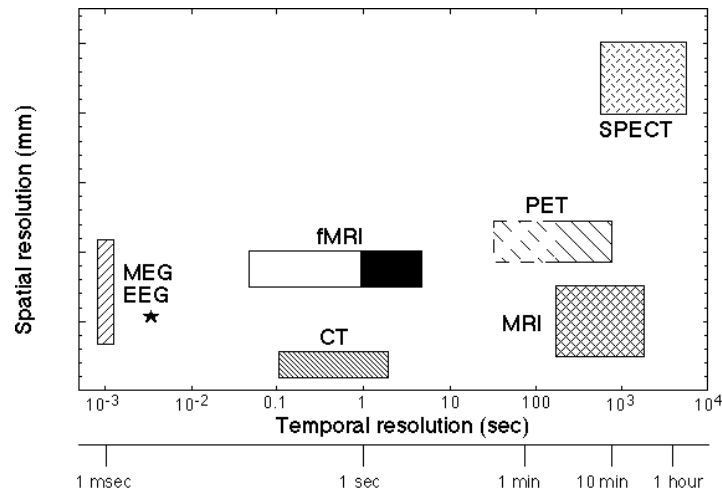


Figure 1.3. Comparison of temporal and spatial resolutions for various imaging techniques (\* the inversion problem for MEG and EEG is poorly defined). PET temporal resolution ranges from about 30 sec to 10 min, where longer times are required for good S/N ratio. The temporal resolution for SPECT is given by the long lifetime of the radioisotopes used. CT does not provide functional imaging and its temporal resolution only reflects the scanning time. Light shaded area for fMRI extends to the minimum scan acquisition time of about 40 msec.

PET have comparable spatial resolutions of several mm - however, the MEG spatial resolution depends on a poorly-defined inverse problem. Standard SPECT has the worst spatial resolution, about 10 mm. The spatial resolutions of all methods are more or less comparable, yet their temporal resolutions are vastly different and suggest that the integration of spatially-robust techniques (MRI, fMRI and PET) with temporally superior techniques (MEG and EEG) has a potential to yield imaging capabilities with optimal spatial and temporal resolutions [54, 55].

Biomagnetometers are complex devices and their construction involves multidisciplinary engineering efforts in areas of sensor development, cryogenics, noise cancellation, electronics, system design, software, and data handling, interpretation and processing. The aspects of cryogenics, SQUID-sensor fundamentals, and biomagnetic signal analysis are covered by other chapters in this volume. The present chapter will concentrate on system questions associated with biomagnetic instrumentation. First, in Section 2 the origins of biomagnetic signals and the relationship between MEG and EEG will be discussed. The general configuration of a biomagnetic system will be shown in Section 3. Biomagnetometers are exposed to environmental noise, and the system design must allow for noise reduction, the electronics must be capable of handling the environmental dynamic ranges and slew rates, and flux transformers must be optimized for the best signal detection in the presence of noise. These questions will be discussed in Sections 4, 5 and 6. Miscellaneous features of biomagnetic systems (the number of channels, the measurement of head position, the registration with MRI images, stimulation equipment, patient support and handling, etc.) will be discussed in Section 7, and selected examples of MEG results will be shown in Section 8. Where applicable, the discussion of various design issues will be illustrated by examples of CTF's instrumentation, because the relevant technical details are accessible to the author.

## 2. MEG and EEG signals

In this section, the origins of magnetic fields generated by the brain are briefly recapitulated, and field patterns produced by a simple model of equivalent current dipole in a perfectly spherical medium are explained. A more detailed treatment of the cellular electrical properties can be found elsewhere [56-58]. The section is concluded by the discussion of the relationship between the magnetic (MEG) and electric (EEG) measurements of the brain.

The human brain is a poorly understood complex system. The cortex contains relatively well-aligned pyramidal cells organized in cortical columns. The cells consist of dendrites, a cell body and an axon, and there are approximately  $10^5$  to  $10^6$  cells in an area of about  $10 \text{ mm}^2$  of the cortex [59] - see Figure 2.1.a and b. There are many connections between various parts of the brain, mediated by the nerve fibers which impinge on other dendrites and cell bodies via synapses. There are approximately  $10^4$  synapses per cell, or about  $10^{10}$  synaptic connections in several cubic mm volume of cortex. In the whole brain there are more than  $10^{10}$  cells and about  $10^{14}$  synaptic connections.

In a pyramidal cell, the dendrite (or a cell body) can be thought of as a tube whose wall is a membrane. Because of the existence of the Na-K pump [56], there is an excess concentration of K inside and of Na outside the cell, and these concentration gradients cause diffusion of  $\text{K}^+$  and  $\text{Na}^+$  ions across the membrane. Since the membrane permeability to K is significantly larger than to Na, the cell characteristics are mostly determined by the dynamics of the  $\text{K}^+$  ions. According to the Nernst equation [56], the diffusion of  $\text{K}^+$  ions across the membrane leads to the establishment of negative potentials inside the cell with an equilibrium value of about  $-70 \text{ mV}$ .

Stimulation of the membrane potential (chemical, electrical or even mechanical) alters the transmembrane potential and can cause cell repolarisation. Such repolarisation happens, e.g., at the synapse, when neurotransmitters are released. Because the cell is conductive, there will be a current between the positive depolarized region and the normal negative region of the cell. The current flow inside the cell is called the impressed or intracellular current, and the return current flow outside the cell is called the volume or extracellular current - see Figure 2.1.c. In the most common detection situation, when the radial magnetic fields are measured, the detected fields (MEG) are produced by the impressed currents, while the volume currents are mostly responsible for the electric potentials (or EEG). The action potentials or axonal currents are usually not observable magnetically, because the polarization is symmetrical, and the associated magnetic fields have a fast spatial decay.

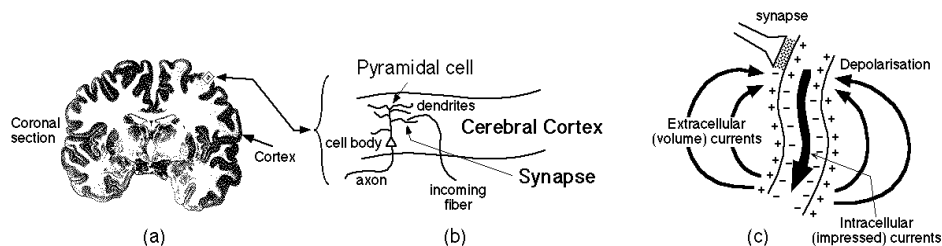


Figure 2.1. Origins of the brain's magnetic fields. (a) coronal section through the brain indicating the cortex consisting of gray matter; (b) small section of cortex expanded to indicate pyramidal cells, dendrites and synaptic connections; (c) intracellular and extracellular dendritic currents.

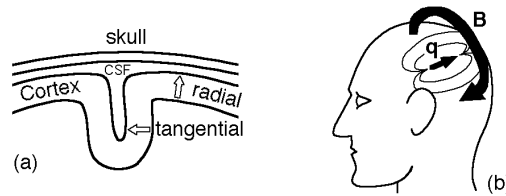


Figure 2.2. Generation of magnetic field by activated cortex. (a) the activation can be located either in sulci, resulting in tangential currents, or in gyri, resulting in radial currents. CSF - cerebrospinal fluid; (b) cortical currents produce fields detectable outside the head.

The impressed current flows in the dendritic area of the pyramidal cells, roughly perpendicular to the cortex - see Figure 2.2.a. The cortex has a complex shape and contains numerous sulci and gyri. As a result, the cortical current can be either tangential or radial to the outer surface of the brain. If the brain were modeled by a perfect sphere, then due to the symmetry, only the tangential impressed currents would produce fields outside the sphere, while the radial currents would produce zero magnetic field [63] - see Figure 2.3 or 2.2.b.

Current flow in a single cell cannot cause a sufficiently strong magnetic field to be detectable outside the head. To produce measurable fields, it is necessary to have nearly simultaneous activation of a large number of cells, typically in the range from  $10^4$  to several times  $10^5$  [57]. However, in some cases, this activation of a large number of cells can still be assumed spatially small and can be modeled by a point equivalent current dipole [64]. It has been shown that the maximum current dipole density is an invariant with magnitude in the range from 0.5 to 2 nA·m/mm<sup>2</sup> [60]. Consider an example of the Auditory Evoked Fields (AEF) as in Figure 4.22. When such fields are interpreted in terms of equivalent current dipoles, they yield dipole magnitudes of 20 to 80 nA·m [61], which in the framework of the maximum estimated current dipole density [60] corresponds to the activated area of the cortical tissue of the order of 1 cm<sup>2</sup>.

The equivalent current dipole is an approximation useful only in a situation where the magnetic field patterns are clearly dipolar, as in the case of various evoked fields. In general, the cortical currents are distributed, and a more sophisticated analysis of magnetic fields should be performed. The concept of current dipoles is, however, very simple and will be used for the purposes of this paper.

The magnetic field of an equivalent current dipole in a spherical medium can be computed analytically [62, 63]. For the geometry in Figure 2.4.c, where the current dipole  $\mathbf{q}$  is located at position  $\mathbf{a}$ , and the measurement is performed at  $\mathbf{r}$ , the field is given by

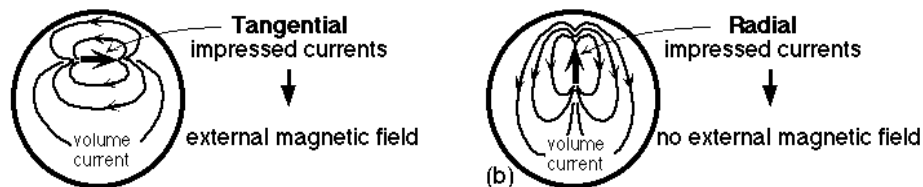


Figure 2.3. Tangential and radial currents in perfectly spherical conductors. (a) tangential impressed currents produce external magnetic field; (b) radial impressed currents do not produce external magnetic field.

$$\mathbf{B}(\mathbf{r}) = \frac{\mu_0}{4 F^2} (\mathbf{F} \mathbf{q} \times \mathbf{a} - \mathbf{q} \times \mathbf{a} \mathbf{r} \mathbf{F}) \quad (2.1)$$

where

$$\mathbf{r}_0 = \mathbf{r} - \mathbf{a} \quad (2.2)$$

$$F = r_0 (\mathbf{r} \cdot \mathbf{r}_0 + r^2 - \mathbf{a} \cdot \mathbf{r}) \quad (2.3)$$

$$F = (r^{-1} r_0^2 + r_0^{-1} \mathbf{r}_0 \cdot \mathbf{r} + 2r_0 + 2r) \mathbf{r} - (r_0 + 2r + r_0^{-1} \mathbf{r}_0 \cdot \mathbf{r}) \mathbf{a} \quad (2.4)$$

A further simplification of the expression for the current dipole field can be obtained if it is assumed that the measured field is radial. This is indeed the case as the majority of MEG detectors are configured to measure the radial or near-radial components of magnetic fields (or their derivatives) - see Section 6. If the sensor array is small, as in Figure 2.4.a, the approximation of radial detectors is quite good; if the sensor array is large, as in the helmet-type systems in Figure 2.4.b, the approximation of a radial detectors is not satisfied for all sensors (especially for the sensors close to the helmet rim). Nevertheless, a useful insight into the character of the brain fields can be obtained by examining the radial fields. Let  $\mathbf{u}_{\text{rad}}$  be a unit radial vector at the sensor location, then the radial magnetic field due to a tangential current dipole can be calculated using the Biot-Savart law

$$\mathbf{B}_{\text{rad}} = \mathbf{u}_{\text{rad}} \frac{\mu_0 \mathbf{q} \times \mathbf{r}_0}{4 r_0^3} \quad (2.5)$$

The radial field in a plane perpendicular to the dipole and passing through the dipole center is shown in Figures 2.5.a and b for shallow and deep current dipoles. The field exhibits two extrema of opposing polarity, and the magnitudes of the extrema and their spacing depend on the dipole depth. If it is assumed that the conducting medium fills half space with a planar boundary, the dipole depth is related to the separation between the dipoles by depth = separation/ 2 [64, 65]. An example of a dipolar field pattern, corresponding to brain response to the median nerve stimulation is shown in Figure 2.5.c. In this case the single dipole approximation is quite satisfactory.

So far, magnetic fields due to an equivalent current dipole have been discussed. Electric potentials (EEG) are related to magnetic fields (MEG) because both methods detect identical current generators - see Figure 2.6. The radial magnetic fields are mostly caused

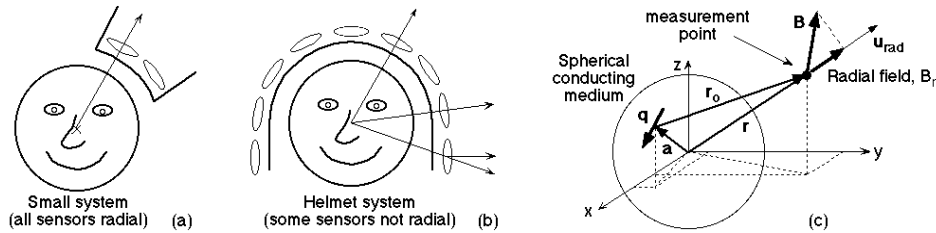


Figure 2.4. Geometry for calculation of the magnetic field of an equivalent current dipole. (a) small detector array, all sensors can be assumed radial; (b) helmet-type detector arrays, not all sensors can be assumed radial; (c) geometry for calculation of magnetic field.

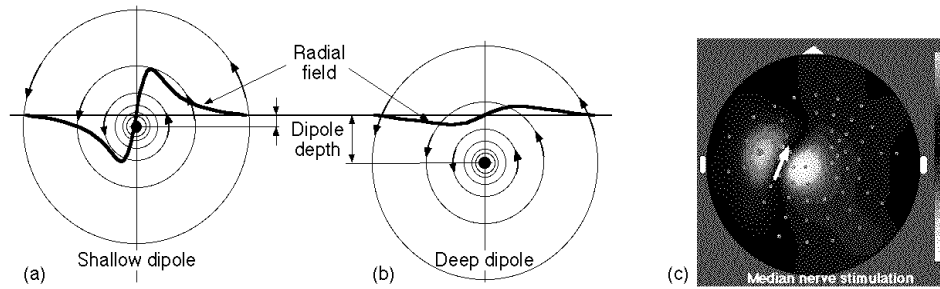


Figure 2.5. The pattern of radial magnetic fields generated by an equivalent current dipole. (a) for a shallow dipole, the field magnitude is large, and the field extrema are close together; (b) for a deep dipole, the field magnitude is small, and the field extrema are more separated; (c) an example of a field pattern due to median nerve stimulation, positions of magnetic sensors are indicated by dots. Aadapted from ref. [16].

by the impressed currents, while the electric fields are caused by the volume currents, and the magnetic field and electric potential patterns on the scalp surface are orthogonal [65]. Further, the equivalent current dipoles determined from the electric and magnetic measurements should be located at the same point, but with opposite directions [66].

An experimental example of such orthogonal electric and magnetic patterns is shown in Figure 2.7 (due to mechanical stimulation of the right index finger [66]). The contour maps of the measured fields are orthogonal, and the dipole directions determined from electrical and magnetic maps are opposite (but at the same location). Note that the magnetic field maps are more localized than the maps of electric potentials.

In conclusion, it was shown that the observable magnetic fields (MEG) are due to an almost simultaneous collective excitation of a large number of cells. The magnetic fields are mostly due to intracellular currents, while the electric potentials (EEG) are due to extracellular (volume) currents. MEG is predominantly sensitive to tangential current generators, and for radial generators, the magnetic fields cancel due to axial symmetry. EEG potentials are sensitive to both radial and tangential generators.

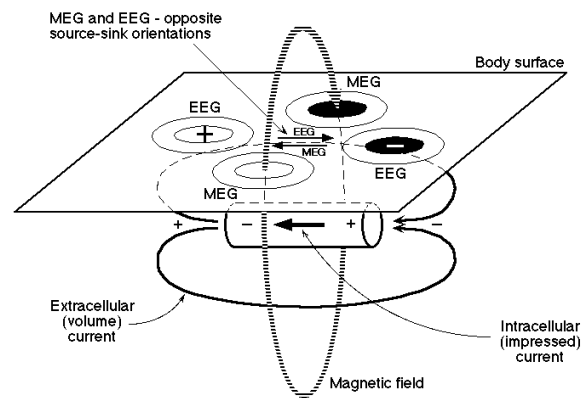


Figure 2.6. The generation of magnetic fields and electric potentials. The radial magnetic fields are caused by intracellular currents and electric potentials are caused by extracellular currents. The directions of currents determined from EEG and MEG are opposite.

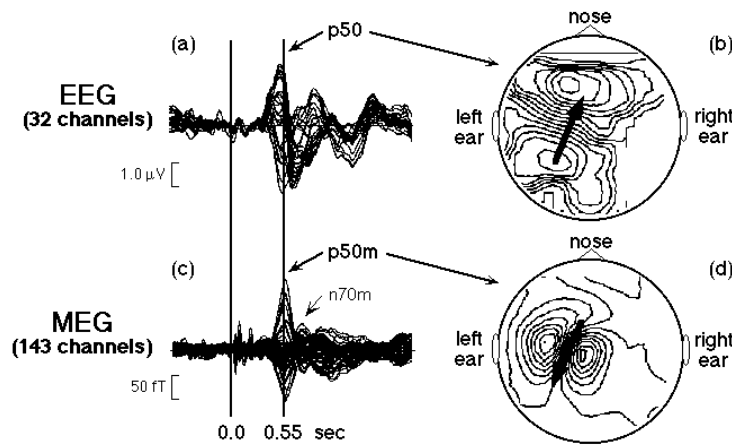


Figure 2.7. Comparison of EEG and MEG (unshielded, 3rd-order gradiometer) signals for the averaged response to mechanical stimulation of the right index finger, 32 channels of EEG and 143 channels of MEG. (a, c) superimposed EEG and MEG signals; (b) isocontour map of electrical field at the peak of p50 response, shaded area represents negative potential in steps of  $0.37 \mu\text{V}$ ; (d) isocontour map of magnetic field at the peak of p50m response, shaded area corresponds to in-going field, contour intervals  $23 \text{ fT}$ . Modified from reference [66].

### 3. General structure and configuration of biomagnetic systems

Biomagnetic systems are complex interdisciplinary engineering creations. In this section, the structure of biomagnetometers will be explained with emphasis on the magnetometer part of the instrument.

The biomagnetic detectors are based on SQUIDs which operate on quantum mechanical principles [67] and exhibit unsurpassed sensitivity to magnetic fields - see Figure 4.2. The basic element of the SQUID sensor is a Josephson junction [6 - 8]. Currently, the most popular version of the Josephson junction for low-temperature applications is a thin-film tunnel junction, shown in Figure 3.1.a. However, other types of junctions, especially in high-temperature superconducting work, are used [68, 69]. The Josephson junctions are employed to form either a DC or RF SQUID [7 - 11, 67]. The SQUID sensors themselves are not always most suitable for the direct detection of magnetic fields and typically, they are coupled to the measured fields using flux transform-

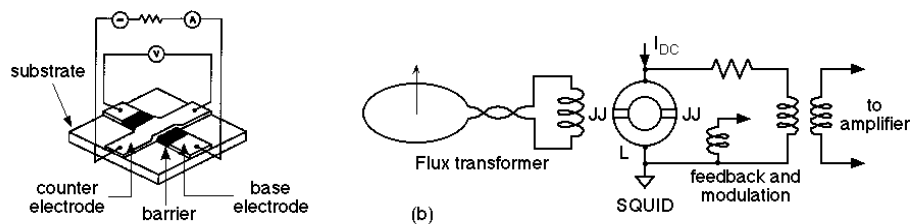


Figure 3.1. Basic elements of a SQUID magnetometer. (a) Josephson junction (thin film tunnel junction in this example); (b) magnetometer comprising flux transformer, DC SQUID with two Josephson junctions, and connections to the electronics.

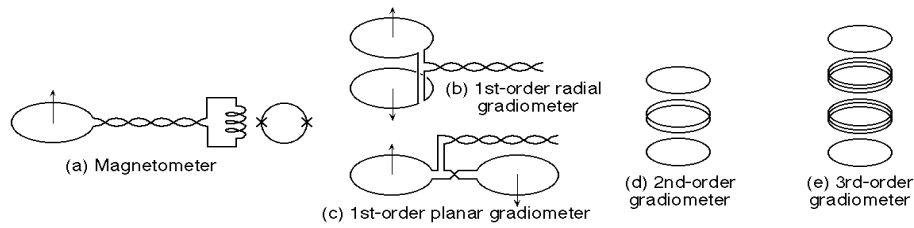


Figure 3.2. Examples of flux transformers. (a) magnetometer; (b) 1st-order radial gradiometer; (c) 1st-order planar gradiometer; (d) 2nd-order gradiometer; (e) 3rd-order gradiometer.

ers, as in Figure 3.1.b. In addition to providing the match to the measured fields, the flux transformers also provide noiseless gain, and their frequency response is flat from DC up to a maximum operating frequency (because the flux-transformer circuits are superconducting).

The flux transformer usually consists of pickup coils, which are exposed to the measured fields, leads and a coupling coil which inductively couples the flux-transformer current to the SQUID. Depending on the measurement objective, the flux transformers can have a variety of configurations, examples of some are shown in Figure 3.2 [70]. The simplest flux transformer is a magnetometer whose pick-up coil is a loop of wire (one or several turns), as in Figure 3.2.a. If the gradient of the magnetic field is required, the pick-up consists of two oppositely-wound coils coupled by a common lead to the SQUID sensor. The currents induced in the two coils subtract, and these devices detect the variation (or gradient) of the magnetic fields. Examples of radial and planar 1st-order gradiometer flux transformers are shown in Figures 3.2.b and c. Higher-order gradiometer flux transformers can be constructed by correctly combining larger number of coils; examples of 2nd- and 3rd-order hardware gradiometer flux transformers are shown in Figures 3.2.d and e.

The SQUID sensors with their associated flux transformers are the basic building blocks of magnetometers - see Figure 3.3. The flux transformers and SQUIDs are immersed in a cryogen within a cryogenic container (dewar). The cryogen is usually liquid

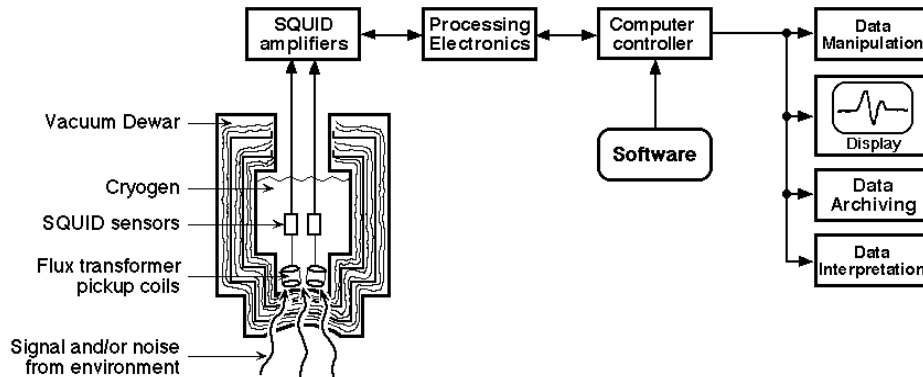


Figure 3.3. Block diagram of elements of a SQUID magnetometer. The cryogenic dewar must be electromagnetically transparent to eliminate distortions of measured fields.

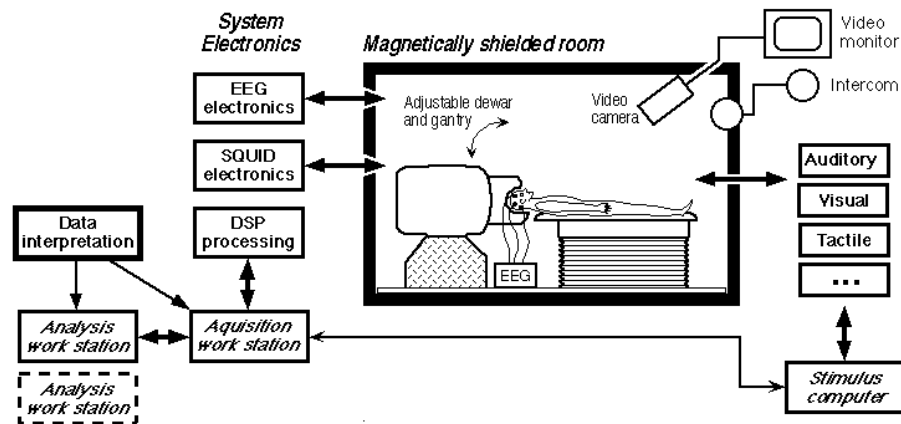


Figure 3.4. Block diagram of a typical MEG system. The MEG dewar is mounted in a gantry capable of seated and horizontal positions. The MEG and EEG detectors in a shielded room are interfaced to electronics and DSP preprocessed before the data are acquired by a computer. There are provisions for delivery of miscellaneous stimuli and for observation of and communication with the patient.

helium for low-temperature sensors and liquid nitrogen for high-temperature sensors. The dewar is a vacuum vessel with a complex set of various heat-shield components in its vacuum space. The signals from SQUID sensors are brought to room temperature by a transmission line, and are amplified and processed by SQUID electronics before acquisition by a computer [22, 23, 71]. Software is used to control the SQUID electronics (tuning, diagnostics, channel configurations, etc.) and data collection (sampling parameters, filtering, etc.). Data are then processed, displayed and archived.

The individual magnetometers then are used as building blocks for biomagnetometers (or specifically MEG) systems - see Figure 3.4. In an MEG system, the dewar is constructed in a helmet shape to cover as large an area of the cortex as possible [22, 23,



Figure 3.5. BTi Magnes® 2500 WH MEG system capable of recording in seated and fully-reclined position. Courtesy of Biomagnetic Technologies, Inc.

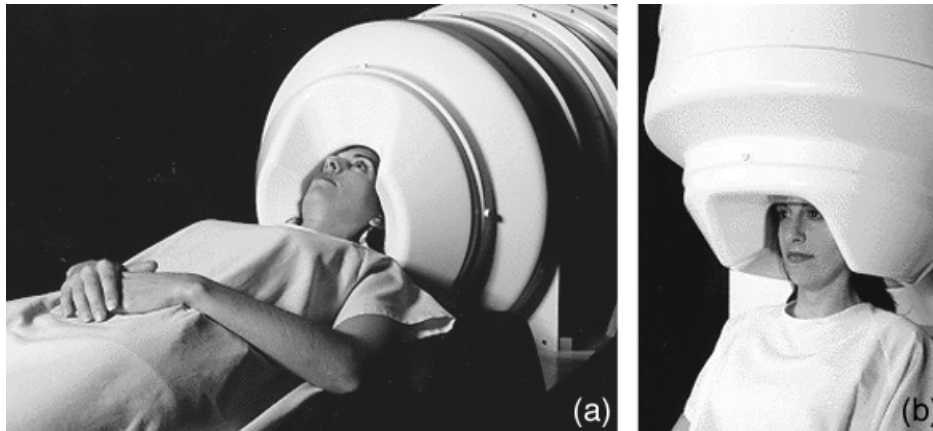


Figure 3.6. CTF Whole-Cortex MEG system. (a) fully supine position; (b) upright position.

24]. The dewar is mounted in a gantry which allows either a seated or horizontal patient position.

The dewar and the gantry may or may not be positioned in a shielded room. The MEG measurement is usually combined with EEG, and both MEG and EEG signals are brought out from the room to the processing electronics and data collection computer. In addition to data collection, there are usually several other computer work stations attached to the system to allow for data analysis while the MEG system is used for measurement. The system also contains a stimulus computer which is synchronized with the data acquisition and can drive various stimulus hardware. The installation is completed with video camera for patient observation and an intercom.

Examples of the existing and newly-announced commercial whole-head MEG systems are shown in Figures 3.5 to 3.7. The systems utilize magnetometers, radial or

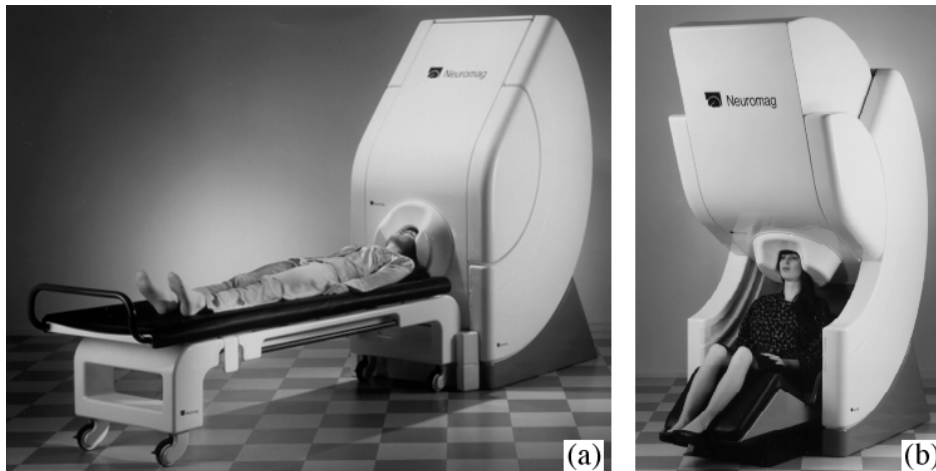


Figure 3.7. Neuromag Vectorview™ MEG system. (a) fully supine measurement position; (b) upright measurement position. Courtesy of Neuromag Ltd.

planar gradiometers, as well as a reference system for noise cancellation. The relative merits of various sensor configurations are discussed in Section 6.

The MEG systems contain a number of diverse technological elements: a shielded room and noise cancellation, SQUID sensor, flux transformers, cryogenics, mechanical supports, electronics and data acquisition, EEG system, peripheral systems, data analysis and interpretation. Each element represents its own interesting technology. The rest of the presentation in this chapter will concentrate in greater detail on noise cancellation and shielded rooms, flux transformers, and issues associated with biomagnetic data acquisition. The issues associated with various peripheral equipment and measuring practices will be dealt with in a less detailed manner.

#### 4. Noise and noise cancellation in biomagnetic measurements

Biomagnetometers (or MEG systems) are exposed to noise even when operated within shielded rooms. Therefore, it is important to understand the character of the noise and have good methods for its elimination. In this section, the noise will be first described and then several methods for its elimination will be discussed: shielding, active noise cancellation, synthetic noise cancellation (high-order gradiometers and adaptive methods), and signal space noise cancellation.

Many examples in this section will show high-order gradiometer results. It should be noted that the formation of high-order gradiometers is a synthetic method, and the gradient order of a particular sensor can be selected not only during the recording, but it can be arbitrarily changed off-line. Therefore, for a given recording, it is possible to simultaneously display the results transformed into several different gradiometer orders.

The noise levels for both magnetometers and gradiometers will be given in field units (T). For gradiometers, such units are obtained by multiplying the correct gradient unit by appropriate baseline lengths (e.g., the 1st gradient unit is [T/m]; however, the unit of 1st-order gradiometer output will be [T], which corresponds to the 1st gradient unit multiplied by baseline length [m]).

##### 4.1. NOISE DESCRIPTION

MEG systems are sensitive to all magnetic fields present in their measuring space. Of prime interest are the fields generated by the investigated brain region (wanted signal), e.g., region "S" in Figure 4.1. However, the measured fields also contain unwanted contributions from various environmental noise sources (e.g., moving cars, elevators, machinery, tools, or power-line signals), from parts of the brain which are not being investigated (e.g., extended background brain activity during investigation of evoked signals), or from other physiological activities (muscle contractions, eye movement, heart beats detected either directly or through ballistic effects, etc.). The objective of the noise cancellation is to separate the wanted brain signals from the contributions due to various unwanted sources.

It is assumed in the present discussion that the noise is of magnetic origin, i.e., the noise is introduced into the system only via the flux transformers - see Section 3. Noise generated by non-magnetic means is assumed to be eliminated by proper design of the biomagnetometer (e.g., any rf interference is eliminated by proper rf shielding within the instrument), and the system electronics is assumed to be perfect (i.e., it is fast

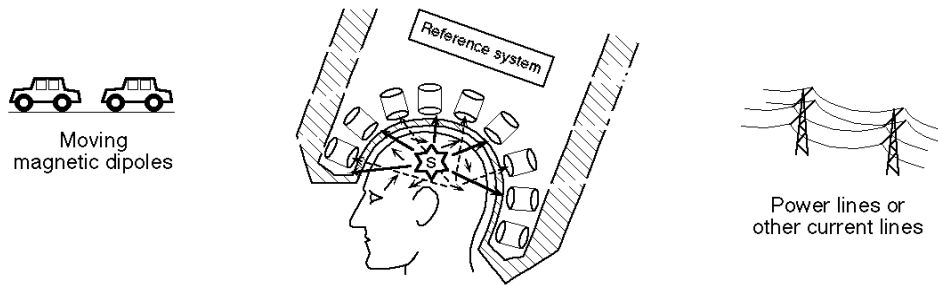


Figure 4.1. Magnetic sensors are subjected not only to the measured MEG signal S, but also to unwanted signals (environmental noise, signals from parts of brain not being measured and other body parts).

enough with sufficiently large dynamic range and good linearity, as described in Section 5). Also, it is assumed that the sensor mounting and the cryogenic vessel have low magnetic contamination and are sufficiently rigid such that the vibrational noise is negligible and various system coefficients are stable over long periods of time.

To appreciate the magnitude of environmental noise relative to biomagnetic fields, examples of both are displayed on the same diagram in Figure 4.2. For comparison, sensitivities of flux-gate [72, 73], optically-pumped [74], and SQUID [67] magnetometers also are shown in Figure 4.2, and it is obvious that only the SQUID magnetometers are sensitive enough for biomagnetic applications.

Environmental noise depends on the type of environment, the time of the day and

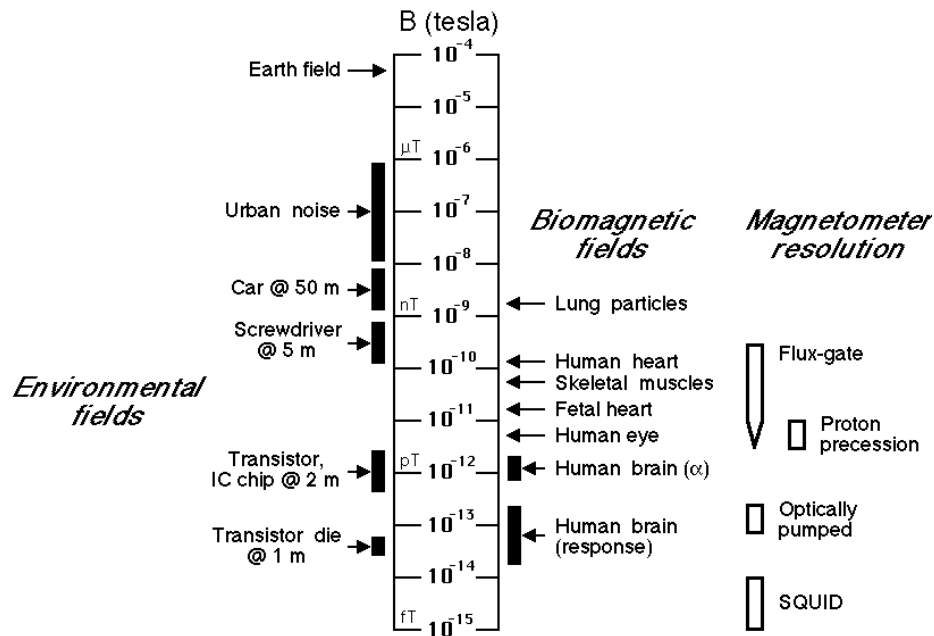


Figure 4.2. Comparison of biomagnetic fields, environmental noise, and sensitivity in 1Hz bandwidth of various types of magnetometers.

whether the system is shielded or unshielded. As a result, for each device and shielding condition, the observed noise shows a variability over several orders of magnitude. Noise cited in a range of papers has been summarised [75 - 81, 70], and its envelopes are presented in Figure 4.3 for magnetometers and 1st-order gradiometers in shielded and unshielded environments. In order to design a system with universally reliable performance, conditions close to the "worst case" in Figure 4.3 should be considered.

For comparison, noise in the 3rd-order gradiometer mode also is shown in Figure 4.3. The upper limit of the curve corresponds to the noise achievable in unshielded environments, and the lower limit corresponds to the noise achievable within shielded rooms. Also shown is a 5 fT rms/ Hz dashed line, which represents a required resolution of the MEG systems.

The "bumps" in the range from 10 to 30 Hz in Figure 4.3 correspond to vibrational noise calculated assuming magnitudes of  $10^{-5}$  rad for rotational and  $10 \mu\text{m}$  for translational vibrations, gradiometer common-mode vector  $C = 10^{-2}$ , baseline  $d = 5$  cm, and DC field and gradient magnitudes in an unshielded environment of  $B_{\text{Unsh}} = 50 \mu\text{T}$ ,  $G_{\text{Unsh}} = 200 \text{ nT/m}$  and within shielded rooms of  $B_{\text{Sh}} = 50 \text{ nT}$  and  $G_{\text{Sh}} = 10 \text{ nT/m}$  [70].

The sharp peaks at 50- to 60-Hz range in Figure 4.3 correspond to the largest observed amplitudes of power-line noise, which for unshielded environments are  $B_{\text{Unsh}} = 500 \text{ nT}$ ,  $G_{\text{Unsh}} = 1 \text{ nT/cm}$ , and in shielded environments  $B_{\text{Sh}} = 5 \text{ pT}$  and  $G_{\text{Sh}} = 40 \text{ fT/cm}$ . The power-line peaks are plotted as if their magnitudes were constant in a 1-Hz bandwidth. The relationship between the field and 1st gradient for power lines can be approximated by assuming that the field of the power-line source is  $B = M/R^n$ , where  $M$  is dipole density in proper units,  $R$  is distance from the power-line source, and  $n = 2$  for parallel wires ( $n = 1$  for a single wire and  $n = 3$  for a magnetic dipole). Then neglecting the vector and tensor character of the fields and gradients, the relationship between  $B$  and the 1st gradient  $G^{(1)}$  can be approximated by

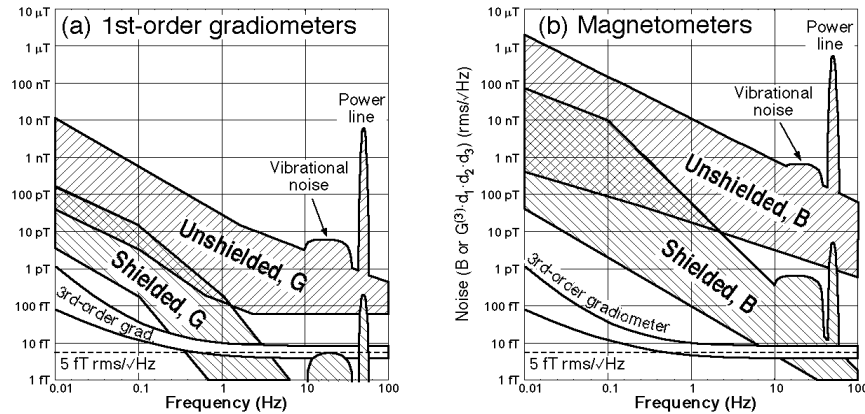


Figure 4.3. Summary of observed noise for balanced 1st-order gradiometers and magnetometers in shielded and unshielded environments. Shielded environments are assumed to be  $\mu$ -metal rooms with modest low frequency attenuation [86]. Bumps in the frequency range from 10 to 30 Hz represent vibrational noise, and the peaks in the range from 50 to 60 Hz represent power-line signals. These peaks represent signal amplitudes and are shown as if their amplitudes were constant in a 1-Hz bandwidth. Dashed line - required system white-noise level of 5 fT rms/ Hz. Gradiometer noise corresponds to gradient noise multiplied by appropriate baselines, i.e.,  $G^{(1)} \cdot d$  and  $G^{(3)} \cdot d_1 \cdot d_2 \cdot d_3$ . (a) 1st gradient noise (measured by a 1st-order gradiometer with baseline of  $d = 5$  cm and balanced to  $C = 10^{-2}$ ); (b) magnetic field noise. Adapted from [109].

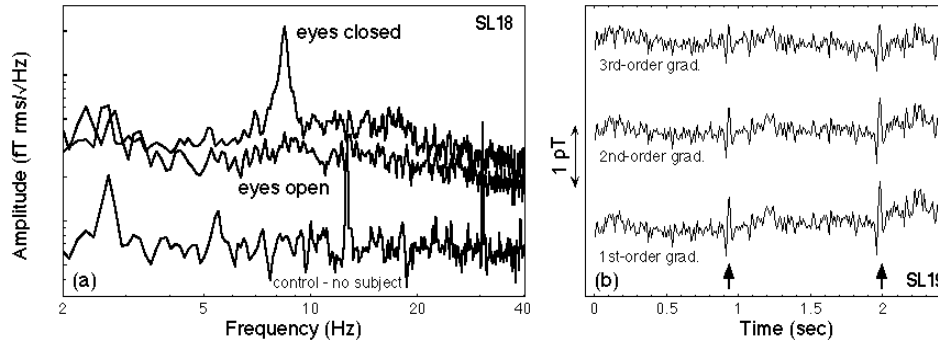


Figure 4.4. Interference signals originating within the human body. The primary sensors were hardware 1st-order gradiometers with 5-cm baseline. (a) spontaneous brain activity and the system noise measured in an unshielded environment (urban laboratory).  $f_s = 250$  samples/sec, collection bandwidth = DC to 50 Hz, frequency bin  $f_b = 0.122$  Hz, 3rd-order gradiometer, files: no subject - Oct 7:15 (93), eyes closed - Oct 7:17 (93), eyes open - Oct 7:18 (93). All traces are in the 3rd-order gradiometer mode; (b) heart beats recorded by a 64-channel MEG system inside a shielded room,  $f_s = 125$  samples/sec, bandwidth = DC to 40 Hz, file: Feb 9:6 (93), subject D.C., no averaging.

$$\frac{G^{(1)}d}{B} = n \frac{d}{R} \quad (4.1)$$

where  $d$  is the gradiometer baseline. Choosing  $d = 5$  cm,  $R = 5$  m,  $n = 2$ , the relationship between the above observed values of field and gradients both in shielded and unshielded environments can be predicted with an accuracy of about a factor of 2. Note that the distance  $R$  is different at different sites.

Examples of noise generated from within the subject's body are shown in Figure 4.4 for two disturbance types. Spontaneous brain activity measured without averaging (in an unshielded environment, 3rd-order gradiometer) is shown in Figure 4.4.a. The white-noise level with no subject is below 10 fT rms/ Hz - there are several environmental lines present which were not completely eliminated by the 3rd-order gradiometer because their sources were too close to the MEG system. With the subject's head in the helmet, the background noise level increases to about 30 fT rms/ Hz (brain noise). Additionally, when the eyes are closed, a spontaneous activity peak at approximately 8.5 Hz is visible. Similar brain noise has been observed [82].

Interference from the heart is shown in Figure 4.4.b - unaveraged data collected in a shielded room and displayed in 1st-, 2nd- and 3rd-order gradiometer modes. The peaks due to heart activity are indicated by arrows. The directly-detected heart signals represent a more severe problem when the gradiometer order is low, and are most disturbing when the measurements are done with magnetometers. Examples of other types of artifacts can be found in the literature, e.g., eye motion [83], or various stimulus artifacts [16, 66].

## 4.2. SHIELDING OF ENVIRONMENTAL NOISE

Magnetic shielding is the most straightforward, but not the least costly, method for reduction of environmental noise. Over the years a variety of shields (shielded rooms) have been used for biomagnetic applications - see Figure 4.5.a. The simplest shielding

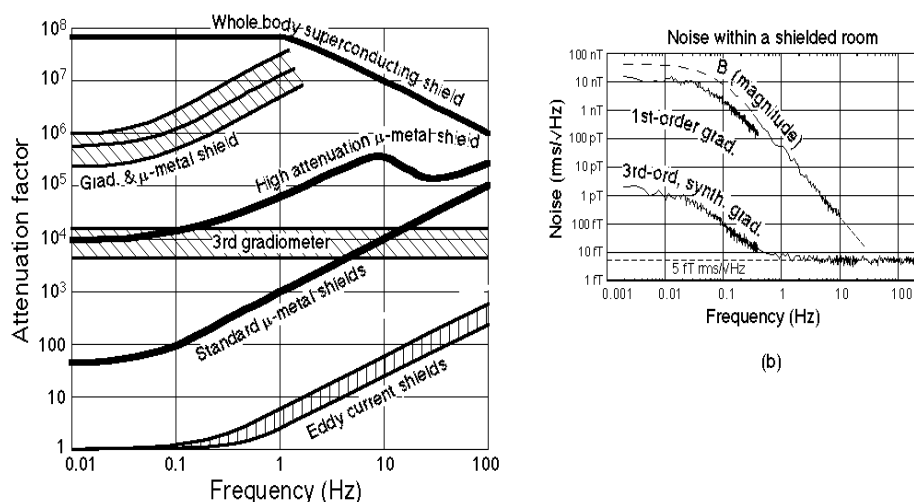


Figure 4.5. Performance of various shielded rooms. (a) noise attenuation factors for Al room, standard  $\mu$ -metal room, high attenuation  $\mu$ -metal room, whole body high-temperature superconducting shield, 3rd-order gradiometer, and 3rd-order gradiometer and combined standard  $\mu$ -metal room (also, see this figure (b) at frequency  $< 1$  Hz); (b) noise within a standard  $\mu$ -metal shielded room (in Vienna), magnetic field, 1st- and 3rd-order synthetic gradiometers.

is accomplished by eddy currents using a thick layer of high-conductivity metal [84, 85]. However, such shielding is not effective at low frequencies. The shielding using high-permeability  $\mu$ -metal provides low-frequency attenuation and is usually supplemented by eddy-current shielding to enhance high-frequency attenuation. The  $\mu$ -metal shields can be roughly divided into two groups: standard shielded rooms with a modest low-frequency shielding factor of less than 100 [86 - 89], and rooms with a large low-frequency shielding factor of  $10^4$  [90, 78]. The standard  $\mu$ -metal rooms are used most frequently in biomagnetism. Very high attenuation of environmental noise can be provided by superconducting shielding. An example is a whole-body, high- $T_C$  superconducting shield, already in operation [91], which provides a low-frequency shielding factor of nearly  $10^8$ .

An alternative to a shielded room is noise reduction by noise cancellation techniques, discussed in Sections 4.4 and 4.5. An example of such noise cancellation is the use of high-order synthetic gradiometers (Section 4.4.2). Depending on the distance distribution of the noise sources, the synthetic 3rd-order gradiometer can provide frequency-independent noise reduction by a factor of several times  $10^3$  to more than  $10^4$  [81, 70]. It has been shown that such noise cancellation also works within shielded rooms when the MEG system is located roughly at the center of the room (far from the room walls) - see Figure 4.5.b. Then the combined noise attenuation of a 3rd-order gradiometer and a standard  $\mu$ -metal room (with modest low-frequency attenuation) is in the range of about  $10^5$  to  $10^6$  [81, 70], better than that of high-attenuation  $\mu$ -metal shielded rooms. Also, the combined attenuation increases with frequency and reaches the attenuation of superconducting rooms at frequencies greater than about 1 Hz.

The environmental noise cannot be neglected even when the MEG system is operated within a shielded room. This is illustrated in Figure 4.5.b., where magnetic field,

1st and 3rd gradient noise are shown within a standard-attenuation  $\mu$ -metal room [81]. The magnetic field noise for frequencies below about 40 Hz, and 1st gradient noise for frequencies below about 4 Hz, are larger than 5 fT rms/ Hz. Since the majority of applications require low frequencies (1 Hz or lower), it is obvious that the shielded-room attenuation must be supplemented by additional noise cancellation.

### 4.3. ACTIVE NOISE CANCELLATION

Environmental noise can be reduced by means of active compensation. Such methods may be applied either without shielding [92], or can be used to supplement attenuation of shielded rooms [93 - 96]. Active compensation consists of a reference detector of magnetic field, feedback electronics and a set of compensating coils, and is usually operated at low frequencies. The sensors can be either SQUID magnetometers, flux-gate magnetometers or coils exposed to the environmental magnetic field, and the compensation can be provided via a system of coils, either surrounding the detection area or wrapped around a shielded room - see Figure 4.6.

When active compensation is used without any shielding [92], as in Figure 4.6.a, the power-line interference must be considered. The compensation can be designed to work either at low frequencies without compensating the power-line harmonics, or it may include the power-line harmonics, in which case it must work up to high frequencies, where the phase variation may be a problem (e.g., it has been observed that the amplitude of the 13th harmonic of 60 Hz can be as high as 1 nT). Generally, there has been very little work reported with active compensation in unshielded environments.

In shielded environments [93 - 96] the most common sensor for active compensation is a SQUID magnetometer located close to the measurement area. If the sensor is located within a distance of up to 1 m from the detection area, attenuation better than 40 dB below about 50 Hz can be achieved. Sensors far from the measurement area or outside the shielded room (e.g., flux gate magnetometers at some distance from the shielded room [94] or normal sensing coils outside the shielded room [96]) yield relatively small attenuation. It has been shown that SQUID gradiometers are not a good reference choice because of the independent relationship between the magnetic fields and gradients within the rooms, generated by the shielding eddy currents [95]. Compensation using gradiometer references produces only a small attenuation - about factor of 5.

Noise of the reference sensors, transformed through the feedback electronics, will contribute additional noise in the measurement area. If the MEG sensors are magne-

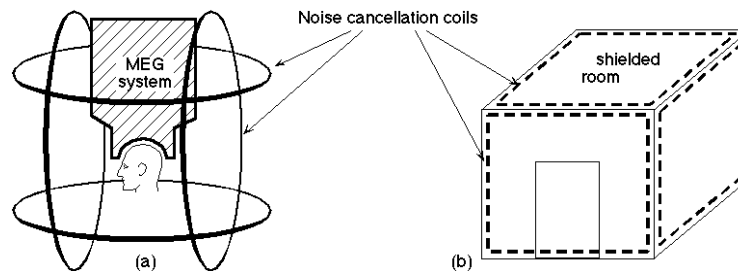


Figure 4.6. Active noise cancellation. (a) coil system in an unshielded environment; (b) coil system combined with a shielded room.

tometers, then the noise of the references is added to the MEG sensor noise [96] (e.g., if the total MEG sensor noise is required to be 5 fT rms/ Hz and if the MEG sensor noise without active compensation is 4 fT rms/ Hz, then the noise of the compensation reference detector should be 3 fT rms/ Hz). If the MEG sensors are gradiometers, then the noise contribution due to the reference is more complicated and will depend on the field uniformity produced by the compensation coils.

#### 4.4. SYNTHETIC NOISE CANCELLATION

Consider a sensor and a number of separate references located at different positions from the sensor. In such a system, synthetic noise cancellation will be understood to mean subtraction of the reference outputs from the sensor output, using subtraction coefficients constructed to accomplish a specified task, e.g., to minimize the norm of the resulting signal, or to construct a higher-order gradiometer, etc. Synthetic noise cancellation is quite flexible because results with different characteristics can be obtained from the same sensor and reference data. This is different from hardware noise cancellation, where the coefficients of the subtraction are predetermined by the hardware construction. For example, a 1st-order hardware radial gradiometer consists of two coils wound in opposite directions, the coil closer to the head may be considered to be a sensor, and the more distant coil, the reference. If the gradiometer is perfect, then the subtraction coefficient is determined by the gradiometer construction and is equal to 1.

First, a general discussion of synthetic noise cancellation will be presented and the differences between synthetic gradiometers and adaptive noise cancellation will be illustrated by an example of a magnetometer-based system. Then, the synthetic higher-order gradiometers will be examined in greater detail, gradiometer balancing will be discussed, and examples of noise cancellation by gradiometers will be shown. The discussion will be concluded by demonstration of adaptive noise cancellation for the frequency-independent and frequency-dependent situations.

##### 4.4.1. General discussion of synthetic noise cancellation

References of a synthetic noise-cancellation system span a wide range of complexity, from simple 3-component magnetometers to complex structures comprising magnetometers and gradiometers suitable for synthetic formation of higher-order gradiometers. The sensors can be either magnetometers (magnetometer-based systems as in Figure 4.7.a), or hardware 1st-order gradiometers (gradiometer-based systems as in Figures 4.7.b and c), or any other types of flux transformers (including that shown in Figures 4.15, 4.17 and 6.1).

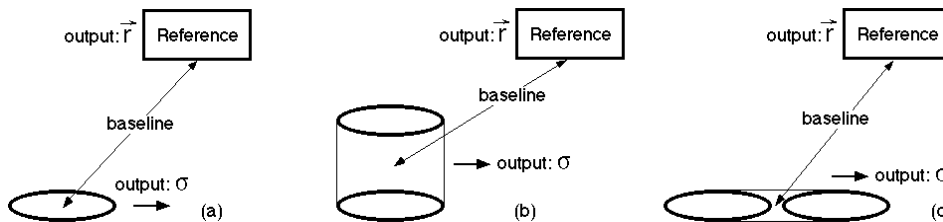


Figure 4.7. Synthetic noise-cancellation systems. (a) magnetometer-based system; (b) hardware 1st-order radial gradiometer-based system; (c) hardware 1st-order planar gradiometer-based system.

Output of the synthetic cancellation system,  $s$ , can be expressed in terms of the sensor output,  $\sigma$ , and reference outputs,  $r_i$ ,  $i = 1, \dots, R$  as

$$s = \sigma - \sum_{i=1}^R \alpha_i r_i \quad (4.2)$$

where  $\alpha_i$  are the subtraction coefficients characteristic of the synthetic process, and  $R$  is the number of references.

The character of the synthetic noise cancellation will be illustrated by an example of a magnetometer-based system with a simple 3-component magnetometer reference, as in Figure 4.8.a. Denote the magnetic field and 1st gradient tensor generated by the noise sources at the origin by  $\mathbf{B}_0$  and  $\mathbf{G}_0$  - the field is a vector and the 1st gradient is a 9-component tensor. If the magnetic sensor is located at the origin and oriented along a direction  $\mathbf{p}$  (unit vector), and the reference is positioned at a distance  $\mathbf{d}$  from the magnetic sensor center, and if 2nd and higher gradients are neglected, then the magnetic field at the reference center is given by

$$\mathbf{B} = \mathbf{B}_0 + \mathbf{G}_0 \mathbf{d} \quad (4.3)$$

Without loss of generality, it can be assumed that the gains of all reference magnetometers and also the sensing magnetometer are identical (and equal to 1), and that the reference magnetometers are perfectly orthogonal and are oriented along the coordinate axes. Then the three outputs from the reference magnetometers form a reference vector,  $\mathbf{b}_{\text{ref}}$ , and the reference and sensor outputs are given by

$$\mathbf{b}_{\text{ref}} = \mathbf{B} \mathbf{p} \quad (4.4)$$

$$\mathbf{b}_{\text{ref}} = \mathbf{B} = \mathbf{B}_0 + \mathbf{G}_0 \mathbf{d} \quad (4.5)$$

The output from the synthetic noise-cancellation process is then given by Eq.4.2 as

$$s = \sigma - \mathbf{b}_{\text{ref}} = \sigma - (\mathbf{B}_0 + \mathbf{G}_0 \mathbf{d}) \quad (4.6)$$

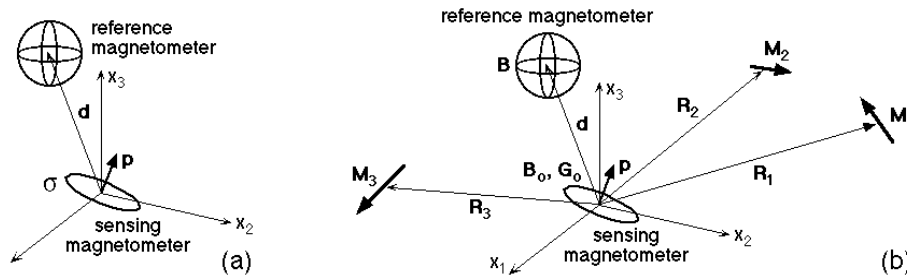


Figure 4.8. Magnetometer-based synthetic noise-cancellation system with vector magnetometer as a reference. (a) general detection configuration; (b) system exposed to a field consisting of a number of noise sources (dipoles  $\mathbf{M}_1$ ,  $\mathbf{M}_2$ , and  $\mathbf{M}_3$  in the present diagram; however, the sources are not limited to dipoles and there can be a number of sources different than three).

The output  $s$  in Eq.4.6 represents the device response to the noise after the noise has been cancelled - at this time only the noise is considered; no signals are applied. Eq.4.6 can be used immediately to determine "true" gradiometer coefficients. Recall, that the 1st-order gradiometer is designed to cancel the magnetic field. Therefore, putting  $\mathbf{G}_o = 0$  and requiring  $s = 0$  in Eq.4.6, the coefficients corresponding to the "true" gradiometer,  $^{\text{grad}}$ , are given by

$$^{\text{grad}} = \mathbf{p} \quad (4.7)$$

For a perfect gradiometer, the vector of the subtraction coefficients is equal to the orientation of the magnetometer sensor. This result is intuitively obvious, as the gradiometer subtraction coefficients will project the reference outputs to the vector  $\mathbf{p}$  and will effectively create a synthetic reference which is parallel to the sensor coil.

Assume that at a given time noise is generated by a collection of noise sources as in Figure 4.8.b. Sources need not be dipolar; dipoles were shown only for simplicity. Eq.4.6 may be rewritten for a time instant  $t_k$

$$s(t_k) = (t_k) - \mathbf{b}_{\text{ref}}(t_k) = \mathbf{B}_o(t_k) \mathbf{p} - \{ \mathbf{B}_o(t_k) + \mathbf{G}_o(t_k) \mathbf{d} \} \quad (4.8)$$

Assume that a number of measurements  $K$  are performed,  $k = 1, \dots, K$ . Define vectors

$$\mathbf{S} = \{s(t_1), s(t_2), \dots\} \quad (4.9.a)$$

$$= \{ (t_1), (t_2), \dots \} \quad (4.9.b)$$

$$\mathbf{B}_{oj} = \{B_{oj}(t_1), B_{oj}(t_2), \dots\}, \quad j = 1, 2, 3 \quad (4.9.c)$$

$$\mathbf{B}_{\text{ref}j} = \{b_{\text{ref}j}(t_1), b_{\text{ref}j}(t_2), \dots\}, \quad j = 1, 2, 3 \quad (4.9.d)$$

$$\mathbf{G}_j = \{(\mathbf{G}_o(t_1) \cdot \mathbf{d})_j, (\mathbf{G}_o(t_2) \cdot \mathbf{d})_j, \dots\}, \quad j = 1, 2, 3 \quad (4.9.e)$$

Also, define the norm of a vector as its magnitude squared. An example of the vector  $\mathbf{S}$  norm is

$$\|\mathbf{S}\| = \mathbf{S} \mathbf{S} = \sum_{k=1}^K s(t_k)^2 \quad (4.10)$$

The objective of the synthetic noise cancellation is to minimize the norm  $\|\mathbf{S}\|$ , or, using Eqs.4.8 and 4.10, to minimize

$$\|\mathbf{S}\| = \sum_{k=1}^K \sum_{i=1}^3 (B_{\text{ref}ik} - B_{ok})^2 \quad (4.11)$$

Further, if it is assumed that  $K$  is large and that the components of magnetic fields and gradients are independent, then the relationships between various vectors in Eqs.4.9 simplify to

$$\mathbf{B}_{oi} \cdot \mathbf{B}_{oj} = \delta_{ij} \|\mathbf{B}_{oi}\| \quad (4.12.a)$$

$$\mathbf{B}_{\text{ref } i} \cdot \mathbf{B}_{\text{ref } j} = \delta_{ij} \|\mathbf{B}_{\text{ref } i}\|^2 \quad (4.12.b)$$

$$\|\mathbf{I}\|^2 = \sum_{i=1}^3 p_i^2 \|\mathbf{B}_{oi}\|^2 \quad (4.12.c)$$

$$\mathbf{G}_i \cdot \mathbf{G}_j = \delta_{ij} \|\mathbf{G}_i\|^2 \quad (4.12.d)$$

$$\mathbf{B}_{oi} \cdot \mathbf{G}_j = 0 \quad (4.12.e)$$

$$\mathbf{B}_{\text{ref } j} \cdot \mathbf{G}_i = p_j \|\mathbf{B}_{oj}\|^2 \quad (4.12.f)$$

$$\|\mathbf{B}_{\text{ref } i}\|^2 = \|\mathbf{B}_{oi}\|^2 + \|\mathbf{G}_i\|^2 \quad (4.12.g)$$

and Eq.4.11 may be rewritten as

$$\|\mathbf{S}\|^2 = \sum_{i=1}^3 \left[ p_i^2 \|\mathbf{B}_{oi}\|^2 - 2 \delta_{ij} p_i p_j \|\mathbf{B}_{oi}\| \|\mathbf{B}_{oj}\| + \sum_i \left( \|\mathbf{B}_{oi}\|^2 + \|\mathbf{G}_i\|^2 \right) \right] \quad (4.13)$$

For large  $K$ , the minimization of Eq.4.11 (or 4.13) relative to the coefficients  $\delta_{ij}$ , yields

$$\delta_{ij} = \frac{p_i \|\mathbf{B}_{oi}\| \|\mathbf{B}_{oj}\|}{\|\mathbf{B}_{oi}\|^2 + \|\mathbf{G}_i\|^2}, \quad i = 1, 2, 3 \quad (4.14)$$

The coefficients in Eq.4.14 are different from the "true" gradiometer coefficients in Eq.4.7. The general solution in Eq.4.14 is equivalent to the gradiometer only if the norm of the gradient vector is zero,  $\|\mathbf{G}_i\| = 0$ , or if the minimization is performed in a uniform, gradient-free field (as in a good quality Helmholtz coil). Then the "true" gradiometer subtraction coefficients depend only on the geometry of the sensor (the orientation vector  $\mathbf{p}$ , Eq.4.7) and are *universal*, i.e., they do not have to be changed when the system is operated in environments with variable noise character (i.e., variable field and gradient composition).

In all other cases when the gradients are present during the minimization, the subtraction coefficients will be called the "adaptive coefficients." The adaptive coefficients are different from the true gradiometer coefficients because they contain information about the gradients present during the minimization. Thus, in the general case, the adaptive coefficients are *not universal* and have to be changed when the environmental character changes.

The difference between the "true" gradiometer and adaptive systems is shown graphically in Figure 4.9. In Figure 4.9.a, a general system consisting of a sensing coil and a reference is shown; the reference is assumed to be a 3-component magnetometer. In Figure 4.9.b a configuration corresponding to a "true" gradiometer is shown (Eq.4.7); the reference is projected to look like the sensing coil (with the same orientation and area), but displaced by the baseline  $\mathbf{d}$ . Figure 4.9.c corresponds to the general adaptation case. The projection of the reference is not parallel to the sensing coil (dashed line), but the difference is not large, especially when the gradient terms  $\|\mathbf{G}_i\|$  are small. Finally, the degenerate adaptation cases are shown in Figures 4.9.d<sub>1</sub> and d<sub>2</sub>. It was assumed during the derivation of Eq.4.14 that the number of measured noise states is large and that the relationships in Eqs.4.12 are valid. If, however, the number of noise states is less

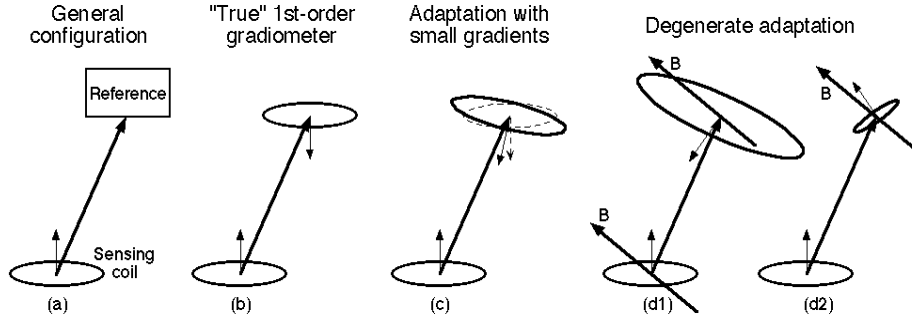


Figure 4.9. Magnetometer-based system, geometrical representation of the difference between various types of subtraction coefficients. (a) general magnetometer-based system; (b) equivalent diagram for a true gradiometer system; (c) adaptive system with adaptation performed with more than three noise states; (d<sub>1</sub>, d<sub>2</sub>) degenerate adaptation with less than three noise states.

than 4, Eq.4.11 can be solved exactly to yield  $\|\mathbf{S}\| = 0$ . If the number of noise states is 3, there is only one solution, and if it is less than 3, there is an infinite number of solutions. In these cases, the environmental reference can be cancelled perfectly by different reference configurations, e.g., a large coil nearly parallel to the applied field (Figure 4.9.d<sub>1</sub>) or a small coil nearly perpendicular to the field (Figure 4.9.d<sub>2</sub>). Such degenerate situations are obtained if short measurements are performed, or if the applied noise does not exercise enough degrees of freedom.

The minimized magnitudes of the norm  $\|\mathbf{S}\|$  for gradiometer and adaptive systems are obtained when the subtraction coefficients from Eqs.4.7 and 4.14 are substituted into Eq.4.13

$$\|\mathbf{S}\|_{\min}^{\text{adapt}} = \sum_{i=1}^3 p_i^2 \frac{\|\mathbf{B}_{oi}\| \|\mathbf{G}_i\|}{\|\mathbf{B}_{oi}\| + \|\mathbf{G}_i\|} \quad (4.15.a)$$

$$\|\mathbf{S}\|_{\min}^{\text{grad}} = \sum_{i=1}^3 p_i^2 \|\mathbf{G}_i\| \quad (4.15.b)$$

In the gradiometer case, the coefficients were determined to completely cancel the field, and therefore the residual  $\|\mathbf{S}\|$  contains gradient components projected to the directions of the baseline and the sensor-coil orientation. In the adaptive case the minimized  $\|\mathbf{S}\|$  contains a mixture of gradients and fields. All quantities in Eqs.4.15 are positive, and for a given component  $i$ , the adaptive term is smaller than the corresponding gradiometer term. Thus, the adaptive process yields better noise cancellation than the gradiometers, but only during the time period for which the noise character is not changing (norms of  $\mathbf{G}_i$ 's and  $\mathbf{B}_{oi}$ 's remain constant). When the noise character is changing rapidly, the gradiometers perform much better than the adaptive process - depending on the time of the day and location, the periods during which the noise character remains constant can be as short as a few seconds [70]. This conclusion also is true for higher-order gradiometers. In addition, it also is found that the higher-order gradiometers perform better than the lower-order adaptive systems.

Consider a simplified case where the magnetometer sensor is oriented along the  $x_3$  direction,  $\mathbf{p} = (0, 0, 1)$ , and introduce the ratio  $r_i = \|\mathbf{G}_i\|/\|\mathbf{B}_{oi}\|$ . Then Eqs.4.15 simplify to

$$\|\mathbf{S}\|_{\min}^{\text{adapt}} = \|\mathbf{B}_{03}\| \frac{r_3}{1+r_3} \quad (4.16.a)$$

$$\|\mathbf{S}\|_{\min}^{\text{grad}} = \|\mathbf{B}_{03}\| r_3 = \|\mathbf{G}_3\| \quad (4.16.b)$$

The amplitude of the mean residual noise is proportional to  $\|\mathbf{S}\|$  and is shown as a function of  $r_3$  in Figure 4.10. For small  $r_3$ 's the gradiometer and adaptive residual noise are comparable. For large  $r_3$ 's the adaptive residual noise is independent of  $r_3$  and is roughly equal to  $\|\mathbf{B}_{03}\|$ . This indicates that the adaptive coefficients are dominated by the environmental gradients and are structured to cancel them; the residual noise is mostly given by the magnetic fields (if  $r_3 \ll 1$ , then  $\|\mathbf{S}\|_{\min}^{\text{adapt}} \approx \|\mathbf{B}_{03}\|$  in Eq.4.16.a). The true gradiometer response is monotonically increasing with increasing  $r_3$ , as shown by Eq.4.16.b. The crossover between the small and large  $r_3$  happens for  $r_3 = 1$  or for  $\|\mathbf{B}_{03}\| = \|\mathbf{G}_3\|$ . At this point, the residual noise of the adaptive process is smaller than that of the gradiometer by a factor of  $1/\sqrt{2}$ .

Next, the equality  $\|\mathbf{B}_{03}\| = \|\mathbf{G}_3\|$  will be examined, and physical conditions for which  $r_3 < 1$  will be determined. Consider, for a moment, that the environmental noise is caused by a dipole source moving on the surface of a sphere with radius  $R$  and origin at the magnetic-field detector. The dipole has a constant moment  $M$ , and its orientations and positions on the sphere surface are random. The magnetic field and gradient at the sphere origin are given by [97]

$$\mathbf{B}_0 = \frac{M}{R^3} \mathbf{o} \quad (4.17.a)$$

$$\mathbf{G}_0 = \frac{3M}{R^4} \mathbf{o} \quad (4.17.b)$$

where the vector  $\mathbf{o}$  and tensor  $\mathbf{o}$  depend on dipole position and orientation and their norms are of the order of 1. The norms  $\|\mathbf{B}_{03}\|$  and  $\|\mathbf{G}_3\|$  can be calculated by substituting Eqs.4.17 to Eqs.4.9.c and e, and their ratio yields the coefficient  $r_3$  as

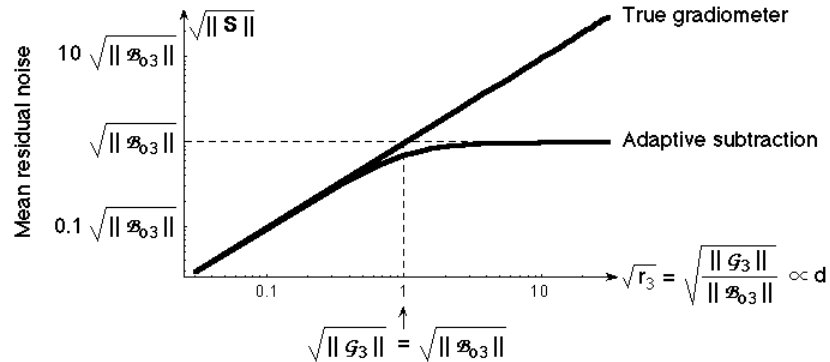


Figure 4.10. Magnetometer based system, mean residual noise for a "true gradiometer" and for an "adaptive system."

$$r_3 = \frac{3d}{R} \quad (4.18)$$

where  $r_3$  is a ratio of the sum of squares of the components of  $\mathbf{d}_o$  and  $\mathbf{d}_s$ , and its magnitude is of the order of 1:

$$r_3 = \frac{\sum_{k=1}^K \mathbf{d}_o(t_k) \cdot \mathbf{d}_s}{\sum_{k=1}^K \{ \mathbf{d}_o(t_k) \}^2} \quad (4.19)$$

The parameter  $r_3$  in Eq.4.18 is proportional to  $d^2$  and for small  $r_3$ , according to Eqs.4.16, the residual noise of both gradiometer and adaptive processes is proportional to the baseline - see also Figure 4.10.

The limit of large  $r_3$  is difficult to achieve in practice. Assume that the parameter is of the order of 1, and consider a longest possible baseline of  $d = 0.3$  m. Then, in order to realize  $r_3 = 1$ , the noise source (or the radius of the sphere) would have to be as close as  $R = 3d = 1$  m. However, in practice, the baselines are shorter and the noise sources are distributed over a much larger range of distances than 1 m. Thus, the coefficient  $r_3$  will always be less than 1, and the residual noise for both gradient and adaptive processes will be roughly proportional to the system baseline  $d$ .

In summary: the synthetic noise cancellation coefficients are different for the gradiometer and adaptive processes. Adaptive coefficients are not universal and cannot be transported to different noise environments. On the other hand, the gradiometer coefficients are universal and remain the same in all noise environments. As a consequence, the synthetic noise cancellation system is a gradiometer if and only if it has "fixed" coefficients. The adaptive coefficients perform better than the gradiometer coefficients during the time period for which the noise character remains constant. In practice, this time period may be very short (several seconds[70]). In all practical situations, the residual noise for both adaptive and gradiometer processes is proportional to the baseline. Only if the noise sources were restricted to the immediate vicinity of the system ( $< 1$  m) would the residual noise of the adaptive process become independent of the baseline. A classification of the noise cancellation processes discussed in this section - processes which depend on reference systems - is shown in Figure 4.11.

The behavior of higher-order processes is qualitatively similar to the simple example of the 1st-order process discussed in this section. The difference between the general adaptive and gradiometer processes is the following: a gradiometer of order  $n$  is designed to cancel the field and all gradients up to order  $n-1$ , and its output is proportional to the

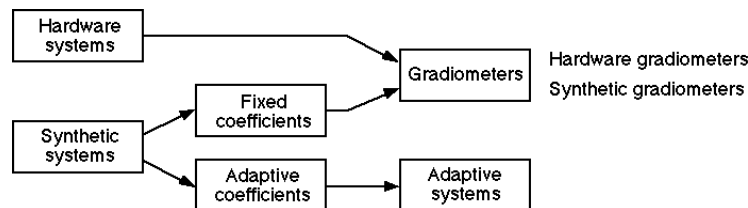


Figure 4.11. Classification of noise cancellation systems.

n-th gradient. On the other hand, the adaptive systems minimize applied fields and gradients of all orders, but the field and lower gradients are not canceled as well as by gradiometers.

#### 4.4.2. Synthetic gradiometers

In this section the noise cancellation and method of synthesis of higher-order gradiometers will be discussed [70]. Hardware higher-order gradiometers were shown to have a promising potential for noise cancellation [98]. However, they are bulky, complicated to construct and difficult to balance accurately, and their full potential was not realized until synthetic high-order gradiometers were introduced [99, 100]. Synthetic gradiometers of up to 3rd-order also were incorporated in whole-cortex MEG systems [22, 23].

Noise cancellation by higher-order gradiometers can be explained by assuming that the noise source has a dipolar character - the noise cancellation principles for other types of sources are similar. The magnetic field generated by a dipole source goes as  $R^{-3}$ , where  $R$  is the distance from the source, Eq.4.17.a, and the spatial gradients are obtained from the field by spatial differentiation. The gradients exhibit faster spatial decay than the magnetic field; increasing the gradient order by 1 increases the distance decay exponent also by 1, and the distance dependence of a k-th gradient is  $R^{-3-k}$ .

When the distance from the dipole source increases, the corresponding signal decays faster if the gradient order is higher. Thus, for a higher-order gradiometer, the dipole disturbance is attenuated faster than for lower-order gradiometers. This is demonstrated in Figure 4.12 for a dipole source with magnitude roughly equivalent to a passenger car (where the vector and tensor characters of the magnetic field and gradients have been neglected).

The hatched band around the 10-fT level indicates the approximate range of resolution (in a 1-Hz bandwidth) required for biomagnetic measurements. In the example in Figure 4.12, a magnetometer would be disturbed by a car up to distances of approximately 2 km. As the gradient order increases, the car disturbance decreases, and finally for 2nd- or 3rd-order gradiometers, the car represents a disturbance only if it is closer

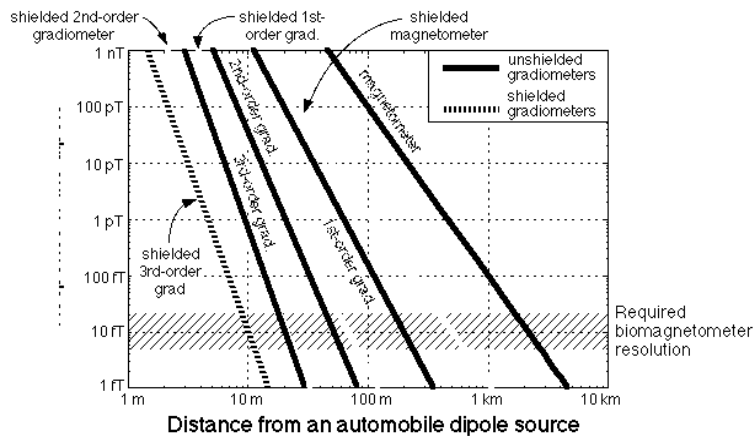


Figure 4.12. Response of spatial gradiometers to a dipole source. Dipole moment magnitude is  $M = 10^{17}$  fT-cm<sup>3</sup> (equivalent to a passenger car), gradiometer baseline unit = 5 cm, room shielding ratio = 70. The hatched band corresponds to the required range of biomagnetometer resolution in a 1-Hz bandwidth.

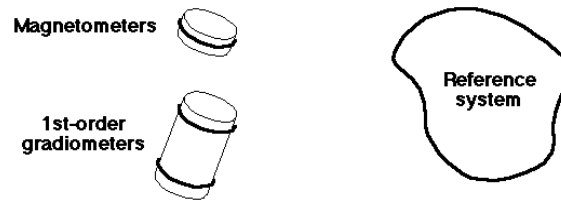


Figure 4.13. Synthetic higher-order gradiometers. The primary sensors are low-order gradiometers, either magnetometers (0th-order gradiometers) or hardware 1st-order gradiometers. The reference system contains a sufficient number of magnetometers and gradiometers to allow synthetic formation of 2nd-, 3rd-, or higher-order gradiometers.

than about 80 or 20 m from the detector, respectively.

Also shown in Figure 4.12 is the effect of a moderately-shielded environment on the dipole signals. If it is assumed that the shielded room does not distort the spatial character of the magnetic fields, then the addition of a shielding factor of 70 to the gradiometer noise cancellation is roughly equivalent to increasing the gradiometer order by 1. A shielded 2nd-order gradiometer therefore behaves as an unshielded 3rd-order gradiometer, while a shielded 3rd-order gradiometer could tolerate cars as close as 10 m from the detection instrument.

Noise elimination by higher-order gradiometers can be termed “spatial filtering” [101], and it functions by assuming that the noise sources are distant while the signal sources are near.

Practical synthetic gradiometers usually have a low-order gradiometer sensor, either a magnetometer (0th-order gradiometer) or a 1st-order hardware gradiometer. A reference system is placed at some distance away from the sensors, and contains a sufficient number of magnetometers and gradiometers to allow synthetic construction of gradiometers of the required order - see Figure 4.13.

The process of synthetic gradiometer formation will be first illustrated in the simplest case of a magnetometer-based 1st-order gradiometer. In this case, the primary sensor is a magnetometer, and the reference system is a three-component magnetometer, as in Figure 4.14 [31, 32, 70, 102]. For simplicity, it is assumed that all reference magnetometers have identical gains. The reference magnetometer outputs are given by

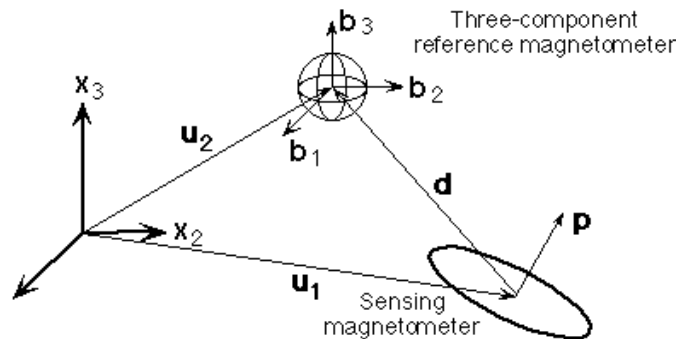


Figure 4.14. Synthetic 1st-order gradiometer based on magnetometer sensor and a vector magnetometer reference.

$$b_k = g_B B_k, \quad \text{where } k = 1, 2, 3 \quad (4.20)$$

where  $g_B$  is the reference gain, and  $B_k$  is one of the three orthogonal components of the applied magnetic field,  $\mathbf{B}$ . The reference magnetometer outputs,  $b_k$ , form a vector of reference outputs,  $\mathbf{b}$ . The sensing magnetometer output is given by the projection of the applied magnetic field on the sensing-magnetometer-coil normal,  $\mathbf{p}$  (as in Eq.4.4)

$$s = g_s (\mathbf{p} \cdot \mathbf{B}) \quad (4.21)$$

where  $g_s$  is the sensing magnetometer gain. To form a software gradiometer, the reference magnetometer outputs are projected on the direction  $\mathbf{p}$ , the projection is scaled by the sensor-to-reference magnetometer gain ratio, and the result is subtracted from the sensor output. Then, similar to Eq.4.5 (using the Taylor expansion for the magnetic field at a location  $\mathbf{u}$ , defining the gradiometer baseline as  $\mathbf{d} = \mathbf{u}_2 - \mathbf{u}_1$ , and shifting the origin to the center of the baseline), the synthetic 1st-order gradiometer output,  $g^{(1)}$ , can be derived as [70]

$$g^{(1)} = - \frac{g_s}{g_B} (\mathbf{p} \cdot \mathbf{b}) = - \frac{g_s}{g_B} \mathbf{p} \cdot \mathbf{G} \cdot \mathbf{d} \quad (4.22)$$

The output of the 1st-order gradiometer is equal to the projection of the 1st-gradient tensor to the vectors  $\mathbf{p}$  and  $\mathbf{d}$ . Examples of ideal 1st-order gradiometers are shown in Figure 4.15. Figure 4.15.a corresponds to an axial gradiometer where  $\mathbf{d} = d(0, 0, 1)$ ,  $\mathbf{p}_2 = -\mathbf{p}_1 = (0, 0, 1)$  and  $g^{(1)} = - \frac{g_s}{g_B} \mathbf{p} \cdot \mathbf{G} \cdot \mathbf{d} = - \frac{g_s}{g_B} d G_{33}$ . Figure 4.15.b corresponds to an off-axis (planar) gradiometer where  $\mathbf{d} = d(0, 1, 0)$ ,  $\mathbf{p}_2 = -\mathbf{p}_1 = (0, 0, 1)$  and  $g^{(1)} = - \frac{g_s}{g_B} d G_{23}$ . In Figure 4.15.c the coils and the baseline are not aligned,  $\mathbf{d} = d(0, 0, 1)$ ,  $\mathbf{p}_2 = -\mathbf{p}_1 = (0, 1/\sqrt{2}, 1/\sqrt{2})$  and  $g^{(1)} = - \frac{g_s}{g_B} d (G_{23} + G_{33}) / \sqrt{2}$ . In this last case, the gradiometer output is a linear combination of the 1st-gradient tensor components.

Software formation of a 2nd-order gradiometer is illustrated in Figure 4.16 [70, 100]. Two ideal 1st-order gradiometers are located at positions  $\mathbf{u}$  and  $\mathbf{u}'$ . The gradiometers have coil vectors  $\mathbf{p}$  and  $\mathbf{p}'$ , and baselines  $\mathbf{d}$  and  $\mathbf{d}'$ .

The Taylor expansion is used to express the gradient at a point  $\mathbf{u}$  in terms of the gradient at the origin as  $\mathbf{G}(\mathbf{u}) = \mathbf{G}_0 + \mathbf{G}^{(2)} \cdot \mathbf{u}$ , where  $\mathbf{G}_0$  and  $\mathbf{G}^{(2)}$  are the 1st and 2nd gradient tensors measured at the origin. The outputs of the ideal 1st-order gradiometers can then be written, using Eq.4.22, as

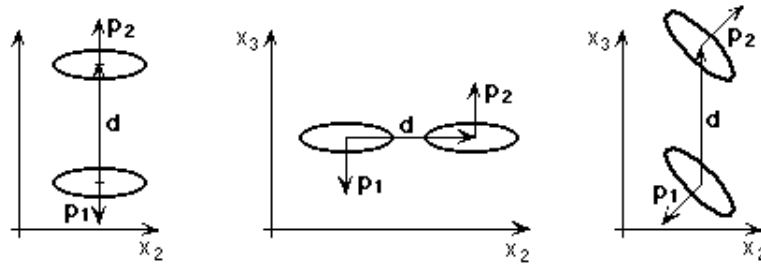


Figure 4.15. Examples of ideal 1st-order gradiometers. (a) axial (radial) gradiometer; (b) off-axis (planar) gradiometer; (c) gradiometer with tilted coils.

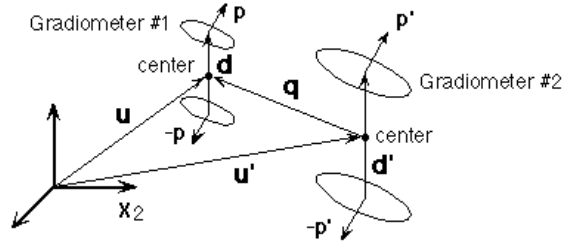


Figure 4.16. Synthetic formation of a 2nd-order gradiometer using two 1st-order gradiometers.

$$g = G \mathbf{p} \cdot (\mathbf{G}_0 + \mathbf{G}^{(2)} \cdot \mathbf{u}) \cdot \mathbf{d} \quad (4.23)$$

$$g' = G' \mathbf{p}' \cdot (\mathbf{G}_0 + \mathbf{G}^{(2)} \cdot \mathbf{u}') \cdot \mathbf{d}' \quad (4.24)$$

The software 2nd-order gradiometer output,  $g^{(2)}$ , with gain equivalent to the gain of gradiometer  $g$ , can be formed by scaling the output of  $g'$  by the ratio of the gains  $G/G'$  and by the ratio of the baselines  $d/d'$ , and by subtracting the scaled result from  $g$ . Assuming that the vectors  $\mathbf{p}$  and  $\mathbf{p}'$ , and  $\mathbf{d}$  and  $\mathbf{d}'$  are parallel, defining the 2nd-order gradiometer baseline as  $\mathbf{q} = \mathbf{u} - \mathbf{u}'$  and shifting the origin to the center of the 2nd-order gradiometer baseline, the 2nd-order gradiometer output can be expressed as

$$g^{(2)} = g - \frac{G}{G'} \frac{d}{d'} g' = G \mathbf{p} \cdot \mathbf{G}^{(2)} \cdot \mathbf{q} \cdot \mathbf{d} \quad (4.25)$$

The output of the synthetic 2nd-order gradiometer in Eq.4.25 is a projection of the 2nd gradient tensor onto the gradiometer vectors  $\mathbf{p}$ ,  $\mathbf{q}$ , and  $\mathbf{d}$ , where  $\mathbf{p}$  is a unit vector, and  $\mathbf{q}$  and  $\mathbf{d}$  have lengths associated with them.

The two 1st-order gradiometers used for the synthesis of the 2nd-order gradiometer can be constructed either in hardware, or either one or both can be formed synthetically. If the sensing 1st-order gradiometer is synthesised from magnetometers, then the above procedure describes the formation of a synthetic 2nd-order gradiometer based on a magnetometer sensor.

Examples of ideal 2nd-order gradiometers are shown in Figure 4.17. Figure 4.17.a corresponds to a 2nd-order gradiometer where all three principal vectors are parallel,  $\mathbf{p} \parallel$

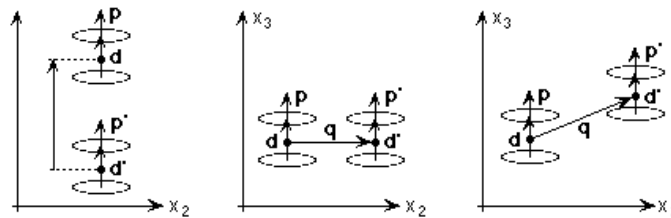


Figure 4.17. Examples of ideal 2nd-order gradiometers. (a) axial gradiometer  $G_{333}$ ; (b) gradiometer  $G_{233}$ ; (c) 2nd-order gradiometer with tilted baseline.

$\mathbf{d} \parallel \mathbf{q}$ , and  $\mathbf{p} = (0, 0, 1)$ . The 2nd-gradiometer output is then  $g^{(2)} = \mathbf{G}_2 \mathbf{p} \cdot \mathbf{G}^{(2)} \cdot \mathbf{q} \cdot \mathbf{d} = \mathbf{G}_2 \mathbf{q} \mathbf{d} \mathbf{G}_{333}$ . The gradiometer in Figure 4.17.b corresponds to the case where  $\mathbf{p} \parallel \mathbf{d} \perp \mathbf{q}$ , and  $\mathbf{p} = (0, 0, 1)$ ,  $\mathbf{q} = q(0, 1, 0)$  and  $g^{(2)} = \mathbf{G}_2 \mathbf{q} \mathbf{d} \mathbf{G}_{233}$ . The gradiometer in Figure 4.17.c has a tilted baseline  $\mathbf{q}$ , and  $\mathbf{p} \parallel \mathbf{d}$ , where  $\mathbf{p} = (0, 0, 1)$ ,  $\mathbf{q} = q(0, 1/\sqrt{2}, 1/\sqrt{2})$ , and the 2nd-order gradiometer output is  $g^{(2)} = \mathbf{G}_2 \mathbf{q} \mathbf{d} (\mathbf{G}_{233} + \mathbf{G}_{333})$ . In this case, the gradiometer output is a linear combination of the 2nd gradient tensor components.

In general, a synthetic 2nd-order gradiometer is formed using a reference system consisting of a 5-component 1st-order tensor gradiometer and a 3-component vector magnetometer. The sensor can be either a magnetometer or a hardware 1st-order gradiometer (Figure 4.13). If the sensor is a magnetometer, then the synthetic formation of the 2nd-order gradiometer proceeds in two steps: (1) a synthetic 1st-order gradiometer with vectors  $\mathbf{p}$  and  $\mathbf{d}$  is generated, and (2) a synthetic 2nd-order gradiometer is constructed by projecting the 1st gradient tensor onto the vectors  $\mathbf{p}$  and  $\mathbf{d}$ , scaling it suitably and subtracting the result from the output of the synthetic 1st-order gradiometer. If the sensor is a 1st-order hardware gradiometer, then step 1 above is omitted, and the 2nd-order gradiometer is directly synthesized as in step 2. Obviously, if the sensor is a magnetometer, steps 1 and 2 can be combined, and performed together as one step. Synthetic 3rd- or higher-order gradiometers are constructed using similar methods.

#### 4.4.3. Gradiometer balancing

In practice, gradiometers are not perfect, either because of manufacturing errors or due to the presence of normal conducting or superconducting objects in their vicinity. The gradiometer deviation from perfection can be described by means of common-mode and eddy-current vectors [70].

For a simple 1st-order gradiometer, the field common-mode vector,  $\mathbf{C}$ , describes the gradiometer residual sensitivity to magnetic field. The origins of the common-mode vector can be either mechanical (imperfect construction, as in Figure 4.18.a and b), or the common-mode vector can be induced by the presence of a superconducting object near the gradiometer (Figure 4.18.c). A normal metal in the gradiometer vicinity can be modeled as an R-L circuit, Figure 4.18.d. The time-varying applied fields will excite currents in it, which in turn will generate magnetic fields and affect the gradiometer. This effect depends on the time derivative of magnetic fields and can be described in terms of an eddy-current vector  $\mathbf{E}$ . Generally, the vectors  $\mathbf{C}$  and  $\mathbf{E}$  are frequency dependent [70], and for some purposes it may be convenient to combine them into a complex, frequency-dependent constant.

The common-mode and eddy-current vectors in the case of higher-order gradiometers are somewhat more complicated. An imperfect  $k$ -th-order gradiometer will have residual sensitivity not only to field, but also to all gradients of order lower than  $k$ . Similarly,

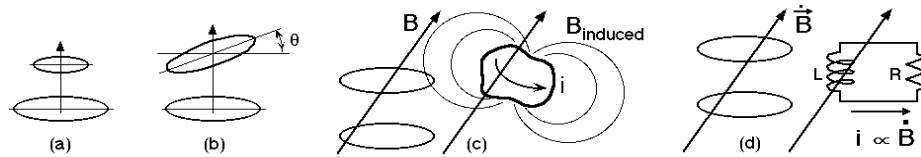


Figure 4.18. Sources of common-mode and eddy-current vectors. (a, b, c) common-mode vector sources; (a) inequality of coil areas; (b) coil tilt; (c) presence of a superconducting object near the gradiometer; (d) eddy-current vector source, presence of a normal-metal object near the gradiometer.

such a gradiometer also will have a residual eddy-current sensitivity to derivatives of field and to all gradients with order lower than  $k$ . If, for simplicity, only the eddy-current contributions due to the field derivatives are considered, the outputs of 1st-, 2nd- and 3rd-order gradiometers can be described as

$$g^{(1)} = G_1 \mathbf{C}_B \mathbf{B} + \mathbf{E} \dot{\mathbf{B}} + \mathbf{p} \mathbf{G}^{(1)} \mathbf{d}_1 \quad (4.26)$$

$$g^{(2)} = G_2 \mathbf{C}_B \mathbf{B} + \mathbf{E} \dot{\mathbf{B}} + \mathbf{C}_{G1} \mathbf{y}_1 \mathbf{d}_1 + \mathbf{p} \mathbf{G}^{(2)} \mathbf{d}_1 \mathbf{d}_2 \quad (4.27)$$

$$g^{(3)} = G_3 \mathbf{C}_B \mathbf{B} + \mathbf{E} \dot{\mathbf{B}} + \mathbf{C}_{G1} \mathbf{y}_1 \mathbf{d}_1 + \mathbf{C}_{G2} \mathbf{y}_2 \mathbf{d}_1 \mathbf{d}_2 + \mathbf{p} \mathbf{G}^{(3)} \mathbf{d}_1 \mathbf{d}_2 \mathbf{d}_3 \quad (4.28)$$

where  $\mathbf{d}_1$ ,  $\mathbf{d}_2$ , and  $\mathbf{d}_3$  have been used to denote the baselines of the 1st-, 2nd- and 3rd-order gradiometer;  $\mathbf{C}_B$ ,  $\mathbf{C}_{G1}$  and  $\mathbf{C}_{G2}$  are 3-, 5- and 7-component common-mode vectors;  $\mathbf{y}_1$  and  $\mathbf{y}_2$  are 5- and 7-component vectors with elements equal to the linearly-independent components of the 1st and 2nd gradient tensors; and  $\mathbf{G}^{(1)}$ ,  $\mathbf{G}^{(2)}$  and  $\mathbf{G}^{(3)}$  are the 1st, 2nd and 3rd gradient tensors. The outputs of gradiometers with order higher than 3 can be expressed similarly. For good noise cancellation the common-mode and eddy-current vectors must be measured, and their effects eliminated from the gradiometer output [70].

#### 4.4.4. Examples of noise elimination by synthetic gradiometers

The noise record [81] for a typical channel of a 143-channel MEG system in a shielded environment (Vienna, [86]) is shown in Figure 4.19.a. This 9-hour-long recording of a shielded 1st-order gradiometer exhibits peak-to-peak signal amplitude of about 175 pT. When the 3rd-order synthetic gradiometer is formed, the peak-to-peak noise is reduced to less than 4 pT (Figure 4.19.a and b). The noise spectra corresponding to approximately the first 3.5 hours of the record in Figure 4.19.a are shown in Figure 4.5.b, and also

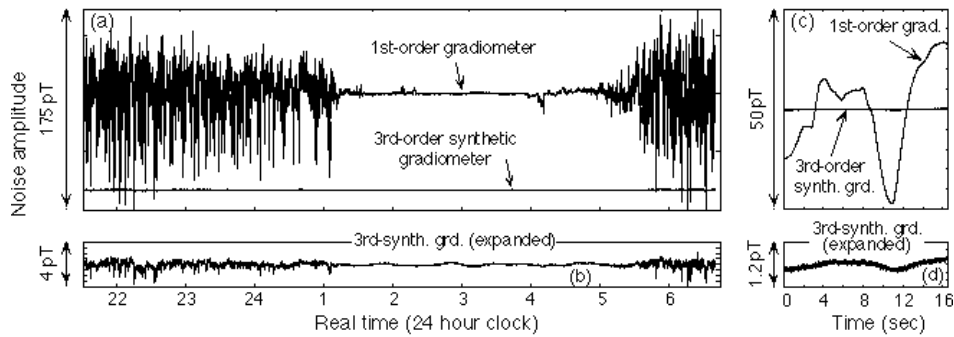


Figure 4.19. Time plots of a typical channel of 143-channel MEG system collected in a shielded room (Vienna). (a) over-night recording, about 9 hours,  $f_s = 1.25$  samples/sec, bandwidth = DC to 0.5 Hz, 1st- and 3rd-order synthetic gradiometers on the same scale (noise spectrum for the time from the beginning of the record to about 0:30 is shown in Figure 4.5.b); (b) expanded plot of 3rd-order synthetic gradiometer from (a); (c) short, about 16 sec, day-time record,  $f_s = 1250$  samples/sec, bandwidth = DC to 300 Hz, 1st- and 3rd-order synthetic gradiometers; (d) expanded plot of 3rd-order synthetic gradiometer from (c).

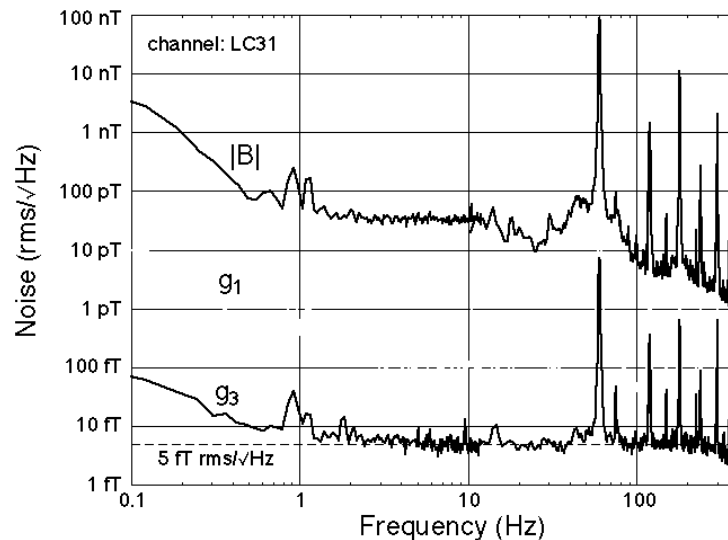


Figure 4.20. Noise spectra collected in unshielded environment (CTF laboratories), 143-channel system.  $|B|$  - magnitude of magnetic field,  $g_1$  - 1st-order gradiometer,  $g_3$  - 3rd-order gradiometer, dashed line - 5 fT rms/  $\sqrt{\text{Hz}}$ . Peak-to-peak amplitude of the magnetic field magnitude at 60 Hz is about 260 nT peak-to-peak.

demonstrate the noise reduction as the gradiometer order is increased. A short, 16-sec segment of data recorded in the same shielded room during the day is shown in Figure 4.19.c and d. Again, in the 1st-order gradiometer mode, the peak-to-peak noise is about 40 pT, and it reduces to less than 1 pT when the 3rd-order gradiometer is synthesized. Figure 4.19 demonstrates that even within shielded rooms, the environmental noise is high and can be successfully reduced by higher-order gradiometers.

The noise of higher-order gradiometers in unshielded environments is shown in Figure 4.20 in the frequency range from 0.1 to about 400 Hz. At lower frequencies, the noise amplitude of the 3rd-order gradiometer is about 4 orders of magnitude smaller than that of magnetometers, and is limited above 1 Hz by the noise floor of the SQUID sensor to about 5 fT rms/  $\sqrt{\text{Hz}}$ . Generally, the unshielded environmental noise has been reduced to below 10 fT rms/  $\sqrt{\text{Hz}}$  above 1 Hz, except for the environmental peaks due to close-by activity or due to power lines. In this example, the magnitude of the magnetic field at 60 Hz is about 260 nT peak-to-peak. Considering the 3rd-order gradiometer white noise level in a 1-Hz bandwidth of about 5 fT rms,  $q = 4$ , the dynamic range of the environmental signal is  $D = 8.3 \times 10^8$  or 178.4 dB (see Eq.5.1).

Further demonstration of the gradiometer performance is shown in Figure 4.21, where the frequency content of the signal and noise are roughly the same, and the signal cannot be separated from the noise by temporal filtering, yet it can be separated by spatial filtering using gradiometers. In Figure 4.21.a, the MCG signal [100] was measured in an unshielded environment. The detector was a synthetic gradiometer with hardware 1st-order gradiometer primary sensor and references capable of 2nd-order gradiometer formation (a 7-channel system, operated with RF SQUIDs and with sensitivity of only about 30 fT rms/  $\sqrt{\text{Hz}}$ ). The increase of gradiometer order from 1st to 2nd removed almost all noise resulting in a clear MCG signal. In Figure 4.21.b an Auditory Evoked

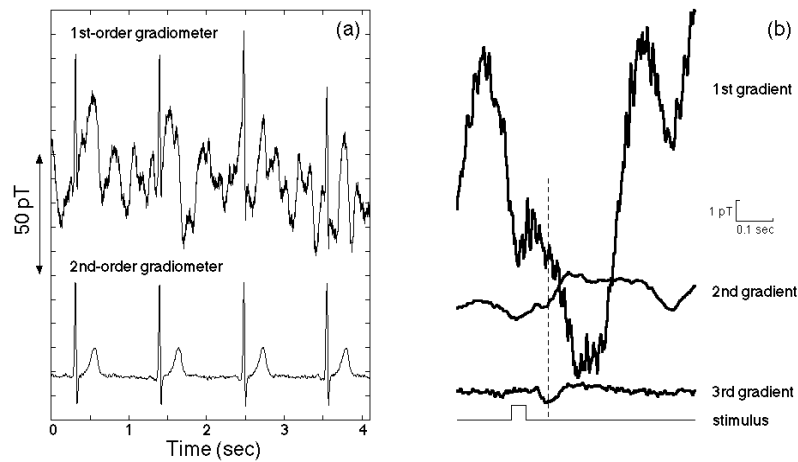


Figure 4.21. Noise cancellation by high-order gradiometers, unshielded environment. (a) heart signals in 1st- and 2nd-order gradiometer mode, bandwidth = DC to 40 Hz (collected using a 7 channel RF SQUID system, primary sensors were hardware 1st-order gradiometers with 5 cm baseline); (b) AEF experiment in an unshielded environment, channel SR44, 1 kHz tone, 50 msec duration, right ear,  $f_s = 625$  samples/sec, duration = 0.82 sec, bandwidth = DC to 70 Hz, 10 averages (collected using a 64 channel MEG system, [22, 23]).

Field (AEF) experiment was performed in the presence of large background magnetic noise (a whole-cortex 64-channel MEG system, operated with DC SQUIDs and with sensitivity of about 5 fT rms/ Hz). Increasing the gradiometer order from 1st to 3rd makes the AEF signal clearly resolvable even though only 10 trials were averaged.

The last example of noise cancellation by higher-order gradiometers in an unshielded environment using a 143-channel whole-cortex MEG system is shown in Figure 4.22 for an AEF experiment. The 3rd-order gradiometers makes the AEF signals clearly visible even in the unshielded environment, and the example shows that the same reference system can produce a consistent performance over all channels.

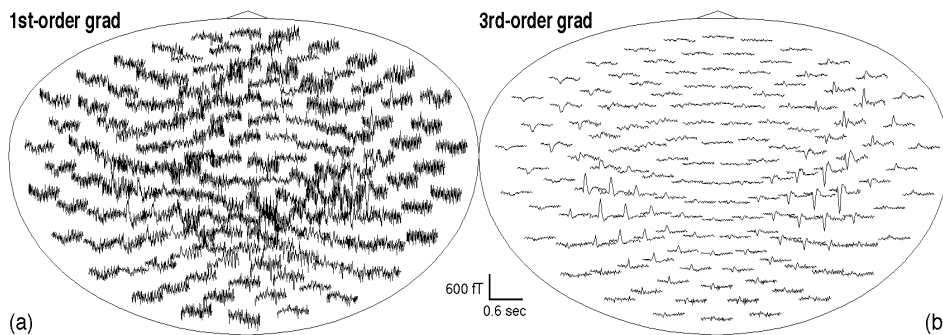


Figure 4.22. AEF experiment in an unshielded environment using 143-channel MEG system, 1 kHz tone, 100 msec duration, both ears, inter-stimulus-interval = 1.5 to 2 sec (random),  $f_s = 625$  samples/sec, bandwidth = DC to 40 Hz, 100 averages, file: Jan 1096:8. (a) 1st-order gradiometer; (b) 3rd-order gradiometer.

#### 4.4.5. Adaptive noise cancellation

Environmental noise also can be removed using adaptive noise cancellation. Similar to synthetic gradiometers, a linear combination of reference outputs is subtracted from each sensor output to remove environmental noise. To determine the adaptive coefficients, a system of sensors and references is observed during the application of some unwanted noise signals, and the subtraction of the references from the sensors is adjusted to minimize the effect of such signals - see Section 4.4.1. Adaptive noise cancellation is a useful tool only when the noise has a time-independent character; adaptive methods do not perform well when the character of the noise is rapidly changing, because the optimum adaptive coefficients also change; in contrast, the gradiometer coefficients are independent of the noise character. For noise sources with variable character, continuous re-adaptation methods should be used. The adaptive process can be either frequency independent or frequency dependent.

An example of frequency-independent adaptation is shown in Figure 4.23 (where the

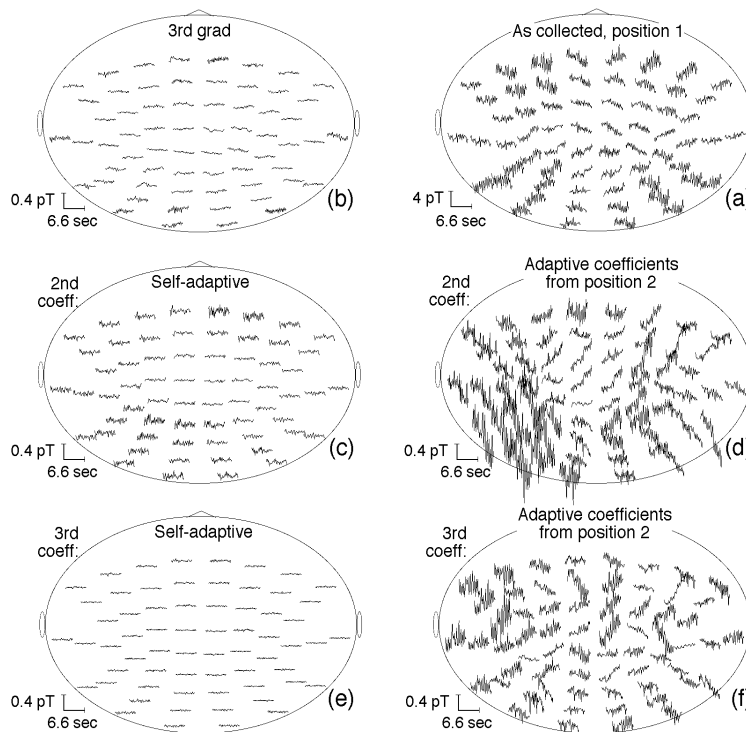


Figure 4.23. Comparison of noise cancellation by 3rd-order synthetic gradiometers and by adaptive subtraction. Unshielded environment,  $f_s = 250$  samples/sec, duration = 6.6 sec, bandwidth = DC to 3 Hz, file: Feb 10:10 (95), magnet in position 1. (a) as collected, 1st-order hardware gradiometer, not balanced; (b) 3rd-order synthetic gradiometer; (c) adaptive noise cancellation using coefficients determined from the data with magnet in position 1 (self-adaptation) and reference channels as for synthetic 2nd-order gradiometer; (d) adaptive noise cancellation using coefficients determined from data with magnet in position 2 and reference channels as for synthetic 2nd-order gradiometer; (e) adaptive noise cancellation using coefficients determined from the data with magnet in position 1 (self-adaptation) and reference channels as for synthetic 3rd-order gradiometer; (f) adaptive noise cancellation using coefficients determined from data with magnet in position 2 and reference channels as for synthetic 3rd-order gradiometer.

adaptive coefficients are frequency-independent constants). To demonstrate the characteristics of such an adaptive procedure, and the differences between the adaptive and higher-order gradiometers, an experiment was performed in an unshielded environment where a magnet with moment  $M = 4.8 \times 10^{13} \text{ fT}\cdot\text{cm}^3$  was moved randomly at a distance of 7 m from an MEG system, in different positions and orientations. Specifically, in position 1, the magnet was located on the  $x_1$  axis, oriented along the  $x_2$  axis and moved parallel to the  $x_2$  axis. In position 2, the magnet was located on the  $x_2$  axis, oriented along the  $x_1$  axis and moved parallel to the  $x_3$  axis.

All data shown in Figure 4.23 were collected in position 1, but were processed with coefficients obtained by different methods. In Figure 4.23.a the “as collected” data (1st-order gradiometer, no balancing, i.e., all coefficients = 0) are shown, and in Figure 4.23.b the same data in the 3rd-order gradiometer mode, with the scale expanded ten times, are shown. In Figures 4.23.c to f, the data after adaptive noise cancellation are shown on the same scale as the 3rd-order gradiometer data. In Figures 4.23.c and d the 2nd-order adaptive process was used, i.e., the adaptive references were identical to the references for the 2nd-order gradiometer. In Figure 4.23.c, the adaptive coefficients were determined from the data itself (i.e., self-adaptation), and the results are only slightly worse than for the 3rd-order gradiometers. In Figure 4.23.d, the adaptive coefficients were determined from data measured with the magnet in position 2. The results are rather poor, and the adaptation does not work well because the character of the noise has changed (when the magnet was moved to a different position).

In Figure 4.23.e and f, the 3rd-order adaptive process was used, i.e., the references were identical to the references for the 3rd-order gradiometer. In Figure 4.23.e, the adaptive coefficients were determined from the data itself (i.e., self-adaptation), producing very good results, even better than for the 3rd-order gradiometers. In Figure 4.23.f, the adaptive coefficients were determined from the data with magnet in position 2. Similar to the situation for Figure 4.23.d, the results are again poor, because the character of the noise has changed - coefficients were determined with the magnet moving in position 2 and then applied to the data collected with the magnet moving in position 1.

The results in Figure 4.23 indicate that it is necessary to have a sufficient number of references for successful noise removal by the adaptive method - the results in Figure 4.23.c are not as good as the results in Figure 4.23.e. Also, it was shown that the adaptive procedure works well only if the noise character remains constant; if the noise character changes, the adaptive coefficients become ineffective and must be re-measured.

If the transfer functions between references and sensors are frequency-dependent (as for  $H_{iy}(f)$  in Figure 4.24), then it is more appropriate to use frequency-dependent adapta-

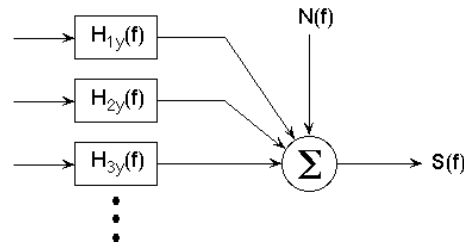


Figure 4.24. Frequency-dependent linear input-output model. The inputs (references R) can be mutually correlated. The sensor output, S, is modeled by summing the references (multiplied by appropriate frequency-dependent transfer functions) and the random noise N.

tion. The problem is solved by the ordered, conditioned input-output model [103]. In this model, the references are ordered by the magnitude of the ordinary coherence function between each reference and the sensor output, and the linear effects of the references  $R_1, R_2, \dots, R_{k-1}$  are removed from  $R_k$  by optimum linear least squares prediction techniques.

A comparison between frequency-dependent and frequency-independent adaptive noise cancellation is shown in Figure 4.25. In this example, the sensor is a magnetometer, and the references are 3 orthogonal magnetometers. The AEF signals were measured in a whole-body superconducting shield [91] with relatively large residual DC fields locked in the shield. Without any noise cancellation, the vibrations caused large noise, which completely obscured the AEF signals, Figure 4.25.a.

When frequency-dependent adaptive noise cancellation was applied, as shown in Figure 4.25.b, practically all vibrational noise was removed, and the AEF signal was detected - the magnetometer was not positioned at the AEF signal maximum, and therefore the signal was rather small. However, when only the frequency-independent adaptive method was used, as shown in Figure 4.25.c, only a small part of the vibrational noise was removed, and the AEF signal was not resolved. In this example, the frequency-dependent adaptive technique was essential for good noise elimination.

In some cases, the frequency-dependent adaptive technique is more successful than the frequency-independent technique. However, the changing noise character represents the same problem for both techniques, and in both cases the re-determination of the coefficients is necessary if the noise character changes.

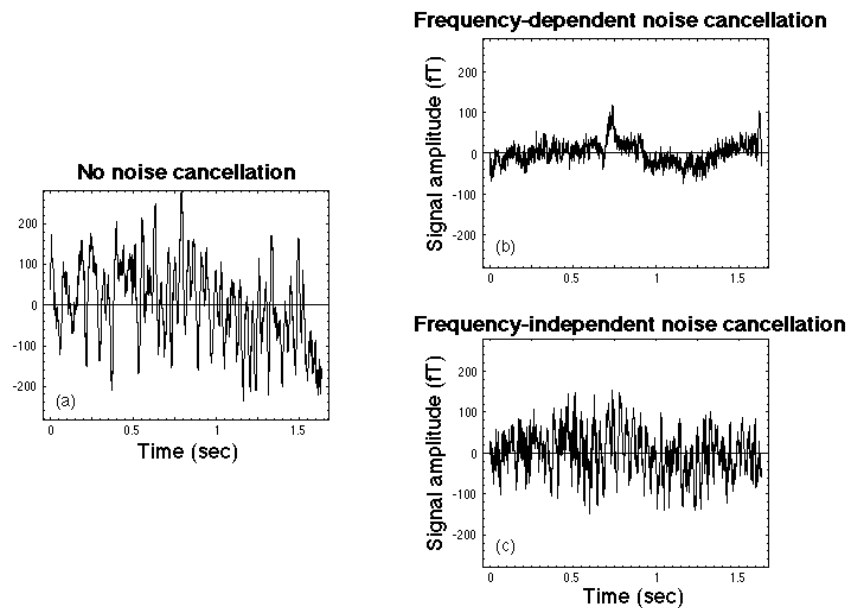


Figure 4.25. Comparison of frequency-dependent and frequency-independent adaptive noise cancellation. AEF experiment, sensor - magnetometer, references - 3 orthogonal magnetometers,  $f_s = 1250$  samples/sec, points per trial = 2048, bandwidth = DC to 300 Hz. Data represents an average of 50 trials, and the transfer functions were determined from 30 trials. (a) data as collected, no noise cancellation; (b) data after frequency-dependent noise cancellation; (c) data after frequency-independent noise cancellation.

#### 4.5. SENSOR SPACE FILTERING

These methods rely on the observation that different signal or noise sources are represented by vectors pointing in different directions in the sensor space - sensor space is a multidimensional space with dimension equal to the number of channels,  $N$ , where each coordinate represents measurement by one channel. Various sources then can be separated from each other by utilizing their different directionality in the sensor space.

One such method, called Signal-Space Projection (SSP) [104, 105] defines a source as a set of current elements with identical amplitudes as a function of time. The signal vector associated with the source is then called a component vector, and has a fixed orientation in the sensor space, only its amplitude is changing with time. A set of  $k$  ( $k < N$ ) component vectors is selected, and using the Decomposition Theorem [106], the sensor space is divided into two subspaces using the projection operators  $P_{\parallel}$  and  $P_{\perp}$ : application of the operator  $P_{\parallel}$  on the measurement selects a subspace spanned by the selected component vectors ( $k$ -dimensional subspace), and the application of the operator  $P_{\perp}$  selects the other subspace, whose elements cannot be produced by any combination of the selected component vectors ( $N-k$  dimensional subspace). The projection operators then are used either to isolate signals from the desired subspace, or to exclude from the signal known unwanted sources. The ability of the method to separate various sources is a function of the angle between the source vectors in the sensor space; if the angle is small, the sources cannot be well separated, while if the angle approaches  $\pi/2$ , a good separation can be obtained.

The method is illustrated in a 2-dimensional sensor space (or 2-channel system) in Figure 4.26, where the measurement vector  $\mathbf{m}$  is assumed to be composed of noise  $\mathbf{n}$  and signal  $\mathbf{s}$ . In Figure 4.26.a the noise is reduced by applying the operator  $P_{\parallel}$  (determined relative to the signal subspace) and constructing a component of  $\mathbf{m}$  in the direction of the "wanted" signal. Alternately, the same result can be obtained by applying  $P_{\perp}$  (relative to the signal subspace) and subtracting the result from the measurement. In Figure 4.26.b the noise is eliminated by application of the operator  $P_{\perp}$  (determined relative to the noise subspace). This procedure is equivalent to using  $P_{\parallel}$  (relative to the noise subspace) and subtracting the result from the measurement. The simple graphical representation in Figure 4.26 also indicates that if the angle between the noise and signal vectors is small, good separation cannot be achieved.

The selected component vectors can be estimated without using a model directly

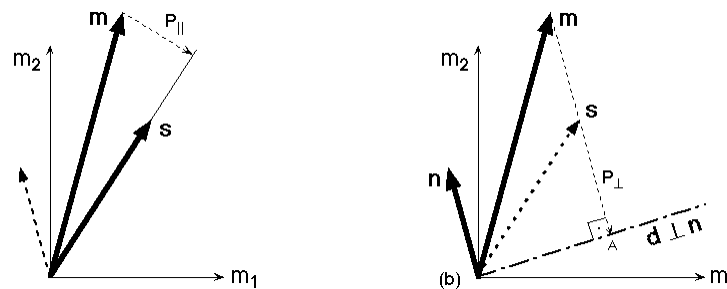


Figure 4.26. Signal space projection, measurement  $\mathbf{m} = (m_1, m_2)$ ,  $\mathbf{m} = \mathbf{n} + \mathbf{s}$ . (a) selection of "wanted" signal by operator  $P_{\parallel}$  (relative to the signal subspace); (b) rejection of "unwanted" noise by operator  $P_{\perp}$  (relative to the noise subspace).

from the measured signal  $\mathbf{m}$ , e.g., by selecting a time when the source of interest is known to be strong in comparison with other components of  $\mathbf{m}$ . Or the selection can be based on information from previous studies, or the constancy of the direction of the measured vector, or the modeling of the measured activity, or other information.

Synthetic Aperture Magnetometry (SAM) [107, 108] maximizes the sensitivity of the sensor array at a specified point in the brain, and minimizes the sensitivity to activities at other localities, and thus provides spatially-selective noise reduction. SAM creates a virtual sensor at the location of interest by means of a projection of the measurements, and the results are normalized to yield an rms value of the activity at the selected location. SAM's good spatial selectivity allows observation of the brain's activity without the need to average the data. The principle of the method also can be illustrated geometrically in a simplified 2-dimensional sensor space, as in Figure 4.27.

For a selected location in the brain, the measurement  $\mathbf{m}$  is assumed to be a sum of signal  $\mathbf{s}$  generated by the current at the selected location and a noise  $\mathbf{n}$  originating from a different source (either other locations in the brain or in the body, or an environmental noise). A forward solution model is used to determine the direction  $\mathbf{s}$  in the sensor space corresponding to the selected point in the 3D (real) space, as in Figure 4.27 (where for simplicity, the possibility of different current orientations at the selected real-space location is neglected in this discussion). When set to the highest spatial resolution, the method rejects the noise  $\mathbf{n}$  by projecting the measurement vector  $\mathbf{m}$  through the operator  $P$  (determined relative to the noise subspace), which in Figure 4.27 corresponds to the projection into a direction  $\mathbf{d}$  orthogonal to the noise  $\mathbf{n}$  (1). Then the result is projected to the forward solution direction  $\mathbf{s}$  (2) and scaled to assure unity gain (3). When the noise vector  $\mathbf{n}$  is close to the forward solution  $\mathbf{s}$ , the amplitude projected through (1) and (2) is small, and subsequent scaling may unacceptably amplify the uncorrelated sensor noise. A trade-off between the spatial selectivity and the resulting noise [106, 108] alleviates this problem and allows a smooth transition between the highest spatial resolution (accompanied by higher projected noise) and the lowest spatial resolution (with low projected noise). In the limit of the lowest spatial resolution the SAM method is similar to the SSP method.

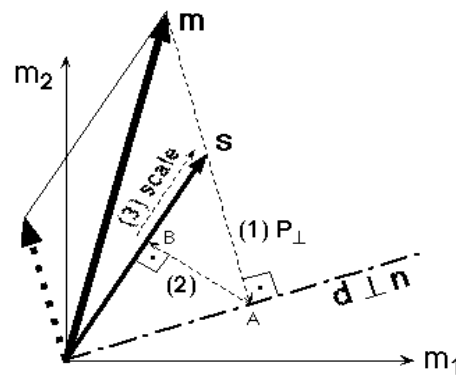


Figure 4.27. Synthetic-aperture magnetometry simplified to a 2-dimensional space (2 sensors).  $\mathbf{m}$  - measurement vector,  $\mathbf{s}$  - direction of interest (forward solution),  $\mathbf{n}$  - noise,  $\mathbf{m} = \mathbf{n} + \mathbf{s}$ ,  $\mathbf{d}$  - direction orthogonal (or nearly orthogonal) to the noise. The measurement,  $\mathbf{m}$ , is projected to the direction  $\mathbf{d}$  to eliminate noise and then the result is projected to the direction  $\mathbf{s}$  and scaled to recover unity gain.

## 5. Character and acquisition of biomagnetic data

Successful operation of MEG systems, both in shielded and unshielded environments, requires well-functioning noise cancellation and low levels of residual noise. These requirements impose certain limits on dynamic range, slew rate, linearity and inter-channel matching, which, together with the large number of channels, must be achieved by the processing electronics and data acquisition system.

In order to appreciate the special characteristics of biomagnetic data collection, it is necessary to put into perspective the relative amplitudes of biomagnetic signals and environmental noise, both for systems operated in shielded and unshielded environments. Also, it is necessary to have knowledge of the sensing flux transformer configuration, as it will affect the parameters of the data, and through it, the character of the processing electronics. Even though large-scale biomagnetometers have been used mostly in shielded environments and there exists only a limited number of examples in unshielded environments [22, 23], the analysis of biomagnetic systems for both shielded and unshielded environments will be carried out in parallel because of the increasing interest in unshielded systems sparked by the development of high- $T_C$  sensors.

The noise cancellation system consists of primary sensors and references (as in Section 4.4). If the primary sensors are magnetometers, the system will be called "magnetometer based," and the distance between the magnetometer coil and the reference will be called the baseline. If the primary sensors are hardware 1st-order gradiometers, the system will be called "gradiometer based."

It will be shown that in order to cancel successfully the environmental noise and to produce good quality data, the data collection system must meet certain criteria for the dynamic range, slew rate, linearity and inter-channel matching. These criteria are vastly different depending on whether the system is magnetometer or gradiometer based. The discussion will follow the path outlined in Figure 5.1. The MEG signals will be used to determine the required system white-noise levels, which together with the environmental noise will define the dynamic range and slew rate to which the MEG system is exposed. The information about the data-processing and noise-cancellation procedures, together with the required dynamic range, will define the linearity and inter-channel matching which must be met by the SQUID electronics. Finally, knowledge of how the data will be processed and the head coverage will define the number of channels, which together with the parameters of the SQUID electronics, define the data collection system [109].

The system white-noise level required for biomagnetic measurement depends on the

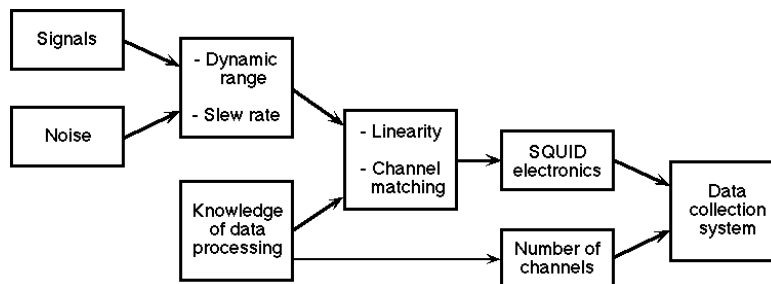


Figure 5.1. Procedure for definition of the data collection system.

magnitude of the measured signal. For the purposes of the present analysis, the system white-noise level will be determined by considering a simple spherical conductor with a point current dipole and requiring that the accuracy of the dipole localization is better than 0.1 cm when the peak signal amplitude is 100 fT. Further, it will be assumed that only the sensor random noise is present, the measurement bandwidth is 100 Hz, the number of averages is 100, and there are 150 channels distributed over a hemispherical sensor shell with radius of 10.7 cm. These assumptions result in the required system white-noise level of  $n_w = 5 \text{ fT rms/ } \sqrt{\text{Hz}}$  - see Eq.6.1.

The noise to which the biomagnetic systems are exposed depends on the type of environment, the time of the day, and whether the system is operated shielded [86] or unshielded [22, 23]. In shielded environments in Figure 4.3, the 1st gradient noise is  $5 \text{ fT/ } \sqrt{\text{Hz}}$  for frequencies greater than 1 to 4 Hz, while magnetic field noise is below that level for frequencies greater than 9 to 70 Hz. In both cases additional noise cancellation is required, and especially the magnetometers alone cannot be used for any meaningful measurement. When unshielded, the noise of both device types is even larger and their operation without noise cancellation is unthinkable.

The noise signals in Figure 4.3 can be used to calculate the signal dynamic range and slew rate. Dynamic range may be defined as the ratio of peak-to-peak (pp) signal amplitude to the system resolution. For a magnetometer-based system, the resolution  $B$  can be related to the white noise in a 1-Hz bandwidth,  $B = n_w \sqrt{1\text{Hz}}$ , by  $B = B_0/2^q$ , where  $q$  is the number of bits by which the resolution is different from the noise in a 1-Hz bandwidth (e.g.  $q = 4$  in [22, 23]). If  $B_0$  is the noise amplitude, the dynamic range for magnetometers is given by

$$D_B = \frac{2B_0}{B} = \frac{2B_0}{B_0} 2^q \quad (5.1)$$

For gradiometers, the dynamic range has a two-fold origin. First, the common-mode signals - see Section 4.4.3 - leak the magnetic field into the gradiometer, and the corresponding gradiometer dynamic range due to the common mode effects is

$$D_G^C = \frac{2CB_0}{Gd} 2^q \quad (5.2)$$

where  $C$  is the common-mode vector,  $d$  is the gradiometer baseline, and  $Gd$  is the gradiometer noise in a 1-Hz bandwidth (in fT rms/  $\sqrt{\text{Hz}}$ ). For the power-line noise, the gradiometer dynamic range due to the common-mode vector can be related to the magnetometer dynamic range in Eq.5.1 through the distance to the power-line source,  $R$ , by Eq.4.1. Second, the dynamic range due to the applied gradient  $G_0$  (T/m) is

$$D_G^{\text{grad}} = \frac{2G_0}{G} 2^q \quad (5.3)$$

where  $G$  is the gradient noise in a 1-Hz bandwidth (in T/m rms/  $\sqrt{\text{Hz}}$ ). The dynamic range calculation for low-frequency noise is slightly more complicated. The low-frequency noise pp amplitude must be determined by integration over the bandwidth of interest. Assume that the low-frequency noise rms value (per  $\sqrt{\text{Hz}}$ ) is

$$n_{\text{low}} = \frac{A}{f^k} \quad (5.4)$$

where  $k$  is the "slope" of the low-frequency noise (dependent on the type of environment [70]), and the dimension of the constant  $A$  is  $\text{fT rms}\cdot\text{Hz}^{k-0.5}$ . Integration of the noise power (or the square of Eq.5.4) should be carried from the lowest frequency of interest,  $f_1$ , to  $f_1 + \Delta f$ , where  $\Delta f$  is the measurement bandwidth. However, the low-frequency noise amplitude decreases rapidly with increasing frequency, and the low-frequency noise contributions at high frequencies are negligible. Therefore, the integration can be performed in the limit  $\Delta f \rightarrow \infty$  to yield the total rms low-frequency noise amplitude

$$n_{\text{rms}} = \frac{A}{f_1^k} \sqrt{\frac{f_1}{2k-1}} \quad (5.5)$$

Assume that the low-frequency noise value,  $n_{\text{low } 1}$  (rms/  $\sqrt{\text{Hz}}$ ) is determined at frequency  $f_1$ . Then substituting  $n_{\text{low } 1}$  and  $f_1$  into Eq.5.4, the constant  $A$  can be calculated. Further, if the pp and rms noise values are related by a factor of 5, then the pp amplitude of the low-frequency noise is obtained as

$$n_{\text{pp}} = 5n_{\text{low } 1} \sqrt{\frac{f_1}{2k-1}} \quad (5.6)$$

The peak-to-peak amplitude in Eq.5.6 now can be used to calculate the dynamic range of the low-frequency noise measured with the lowest frequency of interest  $f_1$ , as

$$D_{\text{Blow } f} = \frac{5n_{\text{Blow } 1}}{B} \sqrt{\frac{f_1}{2k-1}} 2^q \quad (5.7)$$

$$D_{\text{Glow } f} = \frac{5n_{\text{Glow } 1}}{Gd} \sqrt{\frac{f_1}{2k-1}} 2^q \quad (5.8)$$

The  $n_{\text{Blow } 1}$  and  $n_{\text{Glow } 1}$  in Eqs.5.7 and 5.8 correspond to the magnetometer and gradiometer low-frequency noise values at frequency  $f_1$ . The observed values of the constant  $k$  in shielded rooms are usually in the range from about 2 to 3. The value  $k = 2$  can be used in all cases, as the results for  $k = 3$  differ from  $k = 2$  by less than 1 bit.

For a magnetometer, the slew rate is defined as  $S = 2 \text{ fB}_0$  (T/sec), where  $f$  is the signal frequency. The slew rate in flux units is obtained from  $S$  by multiplication by the gain  $G = G/B$ , where  $G$  is the flux noise in  $\text{pT rms}/\sqrt{\text{Hz}}$ . Then, the flux slew rate (in  $\text{pT}/\text{sec}$ ) can be expressed in terms of the dynamic range as

$$S(\text{pT}/\text{sec}) = f 2^{-q} D. \quad (5.9)$$

A result similar to Eq.5.9 also is valid for gradiometers, provided that the gradiometer values for  $G$ ,  $D$  and  $q$  are used.

The dynamic range of the noise in Figure 4.3 as a function of frequency is shown by the hatched and crosshatched areas in Figure 5.2. Also shown are lines of constant slew rate calculated from Eq.5.9. For shielded systems, all noise sources exhibit negligible slew rates ( $< 10 \text{ pT}/\text{sec}$ ). However, the dynamic range of low-frequency noise is large, up to about 21.5 bits (129.4 dB) for gradiometers and up to 26.5 bits (159.5 dB) for magnetometers. For unshielded systems, both slew rate and dynamic range are large. Slew rate is dominant for power-line noise ( $\sim 2 \times 10^4 \text{ pT}/\text{sec}$  for gradiometers and  $\sim 10^6$

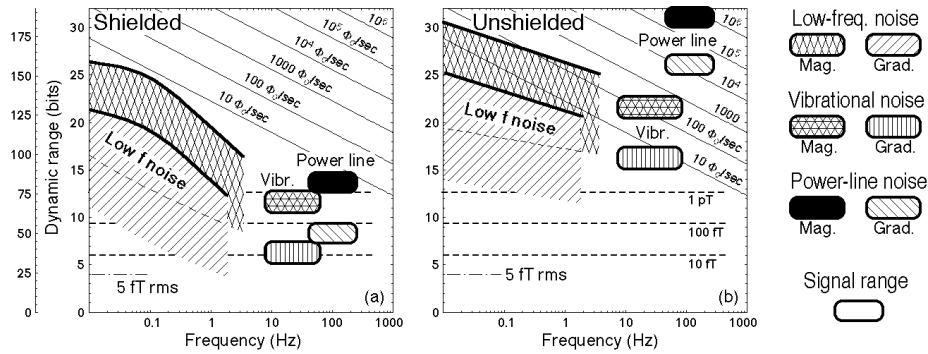


Figure 5.2. Dynamic range as a function of frequency for observed noise in Figure 4.3 for gradiometer- and magnetometer-based systems. The baseline of the hardware 1st-order gradiometer sensors is  $d = 5$  cm. The dynamic range of MEG signals is shown by dashed lines and shaded areas labeled by 10 fT, 100 fT, and 1 pT. Dash-dot line is white noise in 1-Hz bandwidth,  $B = 5$  fT rms,  $q = 4$ . Vibrational noise as described in connection with Figure 4.3, and field power-line amplitudes of 200 nT in unshielded and 2 pT in shielded environments were assumed. Modified from reference [109].

$\sqrt{\text{sec}}$  for magnetometers), and the dynamic ranges for the power-line and low-frequency noise are comparable, being slightly larger for the power-line noise, up to 26.5 bits (159.5 dB) for gradiometers and up to 31 bits (186.6 dB) for magnetometers.

Successful noise cancellation (as in Sections 4.4 and 4.5) and any other data processing are possible only if the system linearity is adequate. For magnetometers, the required linearity may be defined as a ratio of the white noise in a 1-Hz bandwidth,  $B$ , to the  $p$ -p applied signal, and it can be expressed in terms of  $D$  and  $q$  as

$$L = \frac{B}{2B_0} = \frac{2^q}{D} \quad (5.10)$$

The same relationship between the  $L$ ,  $D$  and  $q$ , as in Eq.5.10, also may be used for gradiometers.

In addition to the linearity, the delay between channels also must be sufficiently small. The delay tolerance may be estimated from a simplified model of common-mode vector balancing in the presence of delay between channels [70] and by requiring that the resulting error is less than the noise in a 1-Hz bandwidth - see Figure 5.3. Consider a simplified model of a magnetometer and a gradiometer in a uniform periodic magnetic field. The magnetometer output is equal to the applied magnetic field,  $B = B_0 \sin(\omega t)$  and the gradiometer output is solely determined by the common mode vector  $C_0$  and it is time shifted by  $\tau$  relative to magnetometer,  $G = C_0 B_0 \sin(\omega t + \tau)$ . The gradiometer output also can be expressed as

$$G = C B + E \dot{B} \quad (5.11)$$

where

$$C = C_0 \cos \omega \tau \quad (5.12.a)$$

$$E = C_0 \tau \frac{\sin \omega \tau}{\tau} \quad (5.12.b)$$

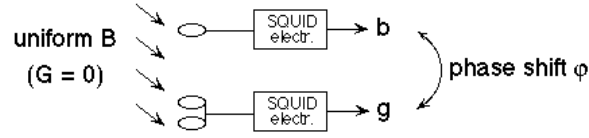


Figure 5.3. Delay or phase shift between SQUID channels.

First, assume that  $\tau \ll 1$ , such that  $C$  and  $E$  are frequency independent constants and the common-mode term in Eq.5.11 is balanced out. Then the eddy-current term in Eq.5.11 represents the delay error. Requiring that the error be smaller than the white-noise in 1-Hz bandwidth,  $B$ , the condition for acceptable delay  $\tau$  is

$$\tau \quad \tau^{(1)} = \frac{L}{fC_o} = \frac{2^q}{fC_oD} \quad (5.13)$$

Note that for magnetometers,  $C_o = 1$ , and the  $\tau^{(1)}$  is much smaller than for gradiometers. As an example, consider the power line frequency  $f = 60$  Hz. A magnetometer-based system with  $C_o = 1$  and  $L = 2^{-27}$  would require delay of 40 psec or less, while a gradiometer-based system with  $C_o = 5 \times 10^{-3}$  and  $L = 2^{-22.5}$  could tolerate delay as large as 170 nsec.

The eddy-current contribution in Eq.5.11 could also be balanced out by differentiating the measured fields and subtracting the eddy current term from the gradiometer output [70]. However, simple digital differentiators produces large errors and more accurate differentiators are computationally expensive or require high sampling rates [126]. Assuming that the differentiation problems can be overcome, then the common-mode and eddy-current terms in Eq.5.11 could both be cancelled by constant  $C$  and  $E$  and the resulting error would be caused only by the frequency dependence of the vectors  $C$  and  $E$ . Assuming that  $\tau$  is sufficiently small, such that expansion of Eqs.5.12 to quadratic terms in  $\tau$  is sufficient, and requiring that the residual error be less than  $B$ , the condition for acceptable delay becomes

$$\tau \quad \tau^{(2)} = \frac{2}{\sqrt{C_o}} \sqrt{\frac{L}{f}} = \sqrt{\frac{\tau^{(1)}}{f}} \quad (5.14)$$

The time  $\tau^{(2)}$  is longer than the time  $\tau^{(1)}$ , provided that  $\tau^{(1)} < (f)^{-1}$ . If for unshielded magnetometer-based system  $\tau^{(1)} = 40$  psec and  $f = 60$  Hz, then  $\tau^{(2)} = 461$  nsec. The delay would become completely unimportant if frequency dependent common-mode and eddy-current balancing was implemented (e.g. by using coherence methods [103]). Such methods are known to work well, but are computationally expensive.

The maximum dynamic range, slew rate and minimum acceptable inter-channel delay are summarized in Figure 5.4. The main results are: the dynamic range of the low-frequency noise is large (even for shielded systems), the slew rate magnitudes are large only for power-line noise in unshielded environments, and the time-delays between channels must be most accurately controlled for unshielded magnetometer-based systems. The time-delay is one of the more difficult parameters to satisfy. If delays of about  $> 100$  nsec are considered to be readily achievable in practice, then the delay  $\tau^{(1)}$  is outside this range for the unshielded power-line noise for both magnetometer- and

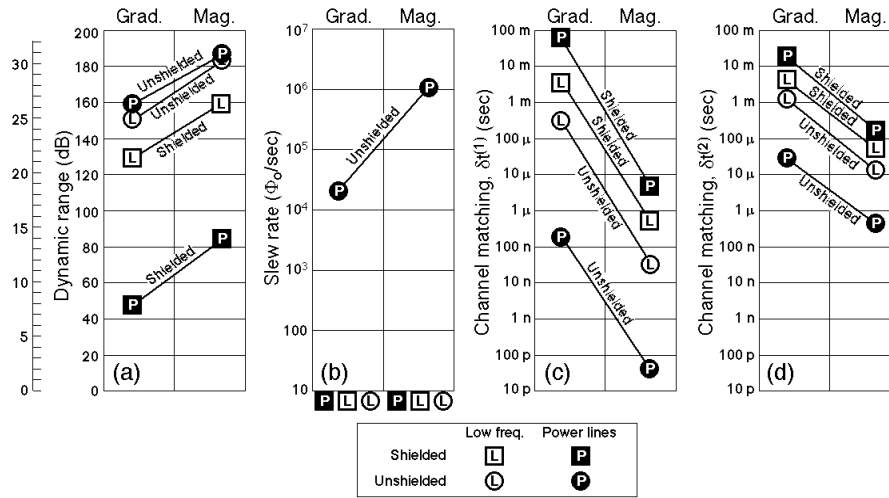


Figure 5.4. Summary of dynamic range, slew rate and acceptable inter-channel delay for 1st-order gradiometer- and magnetometer-based systems.  $C_o = 5 \times 10^{-3}$  (gradiometers),  $C_o = 1$  (magnetometers),  $q = 4$ . Frequencies for calculation of acceptable delay: low-frequency noise  $f = 0.1$  Hz, power-line signals  $f = 60$  Hz. Dynamic range values: gradiometers - shielded low-frequency noise = 21.5 bits, shielded power-line signals = 8 bits, unshielded low-frequency noise = 25 bits, unshielded power-line signals = 26.5 bits; magnetometers - shielded low-frequency noise = 26.5 bits, shielded power-line signals = 14 bits, unshielded low-frequency noise = 30.5 bits, unshielded power-line signals = 31 bits. (a) dynamic range; (b) slew rate; (c) acceptable delay  $t^{(1)}$  - Eq.5.13, assuming that the eddy-current term is not balanced; (d) acceptable delay  $t^{(2)}$  - Eq.5.14, assuming that accurate differentiation is available and both common-mode and eddy-current terms are balanced. Modified from reference [109].

gradiometer-based systems, and for low-frequency noise for unshielded magnetometer-based systems. The time-delay  $t^{(2)}$  is always larger than several 100 nsec, and it is shortest for unshielded magnetometer-based systems and power-line signals. The time-delay specifications can be put into perspective by considering that the propagation delay on 1 m of transmission line is about 5 nsec (with propagation velocity equal to 2/3 of the speed of light) and the shortest delay specification of 25 psec for unshielded magnetometers in Figure 5.4.c corresponds to a transmission-line length of about 0.5 cm.

The MEG electronics manufactured by CTF Systems Inc. will be discussed as an example of a system designed to meet the specifications derived on the basis of the environmental noise for both shielded and unshielded cases.

The dynamic range of the SQUID feedback loop was extended by utilizing the flux periodicity of the SQUID transfer function [110], Figure 5.5.a, and the loop was completed with a digital integrator in order to assure optimum channel-to-channel matching [71], as shown in Figure 5.5.b. The loop is locked at an extremum of the SQUID transfer function and remains locked for the applied flux in the range of  $\pm 1 \mu\text{T}$ . Figure 5.5.a. When this range is exceeded, the locking point is shifted by  $1 \mu\text{T}$  along the transfer function. The flux transitions up and down the transfer function are counted and are combined with the signal from the digital integrator to yield a dynamic range of 32 bits (192.7 dB). The linearity of the system was measured to be better than  $10^{-6}$  at a signal amplitude of  $1000 \mu\text{T}$ . It is not known if the resulting linearity limit is due to the SQUIDS, electronics system or the measuring apparatus.

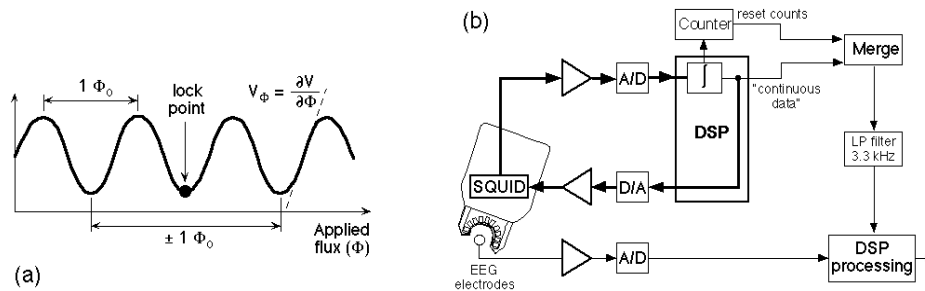


Figure 5.5. Operation of SQUID feedback loop (CTF Systems Inc.). (a) SQUID transfer function with periodicity of  $1 \Phi_0$  and  $\pm 1 \Phi_0$  locking range; (b) schematic diagram of SQUID feedback loop. The loop is completed digitally to assure optimum channel-to-channel matching. Outputs from the SQUID MEG and EEG channels are subjected to identical DSP processing. Modified from reference [109].

The operation of the digital loop is shown in more detail in Figure 5.6. In Figure 5.6.a the input sinusoidal signal is shown with a vertical scale in  $\Phi_0$ . Whenever an integer multiple of  $\Phi_0$  is traversed, the loop lock is released, the loop is internally reset to zero, and either a plus or minus count is added to the counter. The internal loop signal is shown by the solid line, and the counter is shown by the gray line in Figure 5.6.b. The internal loop signal is recorded with a resolution of 20 bits per  $1 \Phi_0$ , and the counter has a range of 12 bits, yielding a data word with a 32-bit range.

Biomagnetic systems also must be capable of handling large numbers of channels. The presently-operated commercial whole-cortex MEG systems contain well over 100 SQUID channels - see Section 3 - and in addition, CTF's versions also are equipped with references, ranging from a few to as many as 29 channels, auxiliary A/D and D/A channels, and in many cases with up to 64 EEG channels.

An example of the CTF electronics architecture for a large number of channels is shown in Fig. 5.7 [71]. The electronics is organized into banks of plug-in units, one unit in each bank devoted to data communications, and twenty units for up to 20 SQUID channels. Variable numbers of banks can be connected via the internal bus to allow for variable numbers of SQUID channels. Usually, some plug-in units also are required to perform A/D and D/A functions. There is also a bank which allows connection of EEG channels and a bank with DSP processors for real-time data processing before transmission to a host computer. A block diagram of the complete electronic system is shown in Figure 5.8.

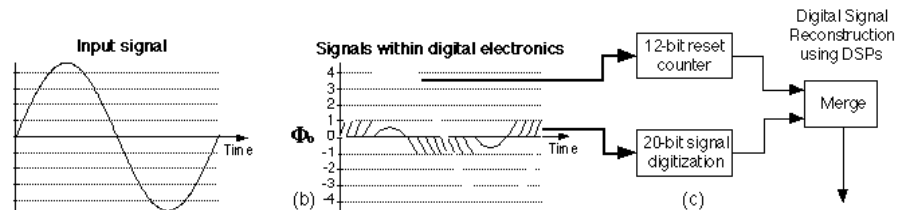


Figure 5.6. Operation of digital SQUID electronics (CTF Systems Inc.). (a) input sinusoidal signal; (b) solid line - signal within the locking range of  $\pm 1 \Phi_0$ , gray line - counter signal (counts of flux transitions along the transfer function); (c) 20-bit digitization of  $\pm 1 \Phi_0$  range and 12-bit counter, merged to yield 32-bit data word.

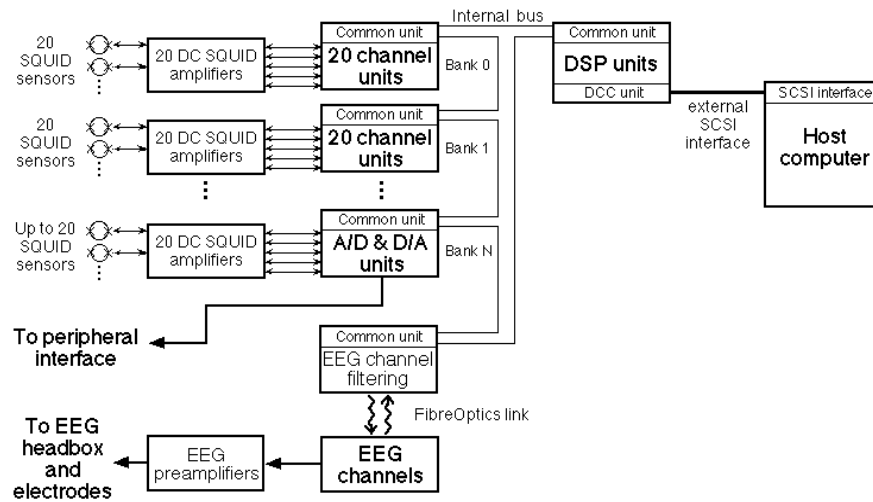


Figure 5.7. Architecture of a biomagnetic data collection system including optional EEG (or ECG) channels (CTF Systems Inc.). Modified from reference [109].

To estimate data throughput, consider an example of a system with 200 SQUID channels with 4 bytes/channel, 64 EEG channels with 2 bytes/channel, and 16 additional A/D and D/A channels, also with 2 bytes/channel, or in total, 960 bytes per sample. With a sample rate of about 2,000 samples/sec, such a system will generate a data rate of about 1.92 Mbytes/sec, and typically, about 1 to 10 Gbytes of data per day in normal use.

*In conclusion:* The signal and noise in biomagnetic measurements were examined and were used to determine the required system dynamic range, slew rate, linearity and delay between channels. An electronics architecture suitable for handling such require-

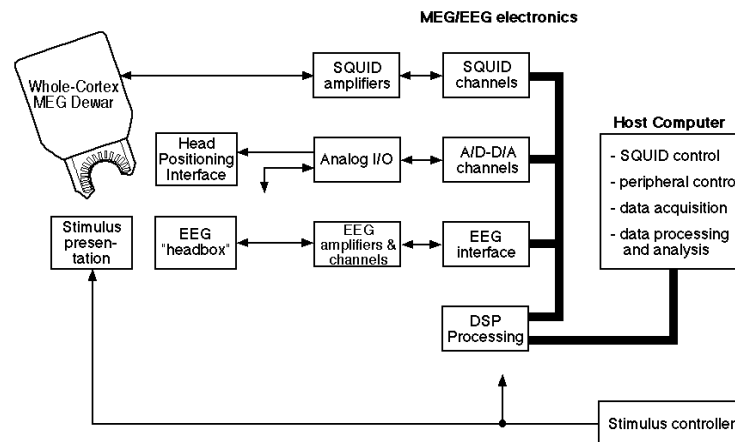


Figure 5.8. Block diagram of the electronics and data collection for an MEG/EEG system (CTF Systems Inc.).

ments, as well as large numbers of channels, was described. It was shown that magnetometer-based systems are subject to far more stringent requirements than gradiometer-based systems and that for magnetometer-based systems some specifications due to the observed environmental noise might be difficult to meet.

Failure to meet the specifications derived in this section would have the following consequences: (a) dynamic range for low-frequency noise - the system could still be operated, but it would have to be reset whenever the limit of the dynamic range was reached (or, in other words, the dynamic range would have to be extended); (b) dynamic range for power-line signals - the system would not be functional because the overflows caused by the dynamic range at the power-line frequencies cannot be handled well in practice; (c) linearity requirement (both for low-frequency and power-line noise) - the data quality would be degraded and accurate noise cancellation or other data processing would not be possible; (d) delay between channels - good noise cancellation would not be possible (the inter-channel time delays could potentially be corrected if the delay were constant and could be measured accurately).

Note that the system requirements also apply to all signal processing functions, e.g., filtering, balancing, etc. The linearity and inter-channel matching requirements drive the choice of digital feedback loops and digital filters, as the errors between analogue circuits can easily exceed the specified tolerances.

## 6. Flux transformers for biomagnetic sensors

The flux transformers of primary biomagnetic sensors can have a variety of forms: magnetometers, 1st-order hardware gradiometers, and in some cases even higher-order gradiometers. Magnetic field is a vector, and therefore, magnetometers can be oriented in three orthogonal directions. First gradient is a 9-component tensor with 5 linearly independent components [70] and usually only the following components of this tensor are used for biomagnetic detection: radial gradient of radial magnetic field, radial gradient of tangential magnetic field, and tangential gradient of radial magnetic field. Tensors of higher gradients have  $3 + 2k$  independent components, where  $k$  is the gradient order. Graphical representation of some primary sensors is shown in Figure 6.1.

MEG and biomagnetism in general are usually discussed in terms of magnetic fields. Yet, in most systems the detection flux transformers are gradiometers. When a uniform magnetic field is applied to a gradiometer, Figure 6.2.a, the currents generated in the two gradiometer coils are equal, and because the coils are connected in opposing direc-

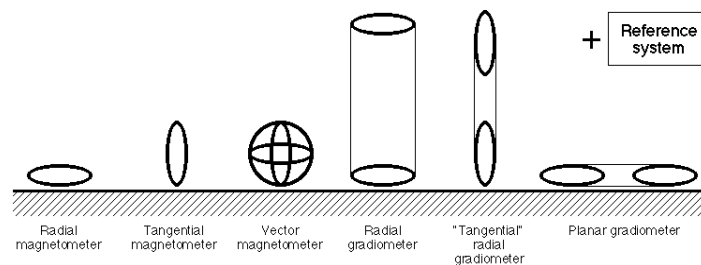


Figure 6.1. Examples of some possible configurations of primary sensor flux transformers.

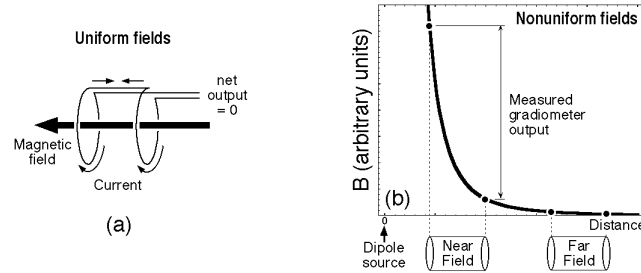


Figure 6.2. Measurement of biomagnetic fields by gradiometers. (a) uniform magnetic field produces zero gradiometer output; (b) gradiometer can be positioned either in near field or far field.

tions, they cancel, and the net output is zero. However, in biomagnetic practice, the fields are not uniform. This is illustrated in Figure 6.2.b, where the source is located at the origin. For a gradiometer positioned in the near field, the variation of the gradient over the gradiometer dimension (baseline) is large, the coil closer to the source sees a much larger field than the more distant coil, and the gradiometer output is roughly proportional to the magnetic field at the closest coil (in reality, the effect of the more distant coil is not neglected and is always included in any data analysis). In contrast, a gradiometer positioned in the far field is exposed to a nearly uniform gradient, and its output is proportional to the spatial derivative of the magnetic field. If the primary sensors are planar gradiometers, the detected signal is a tangential difference of fields (approximately equal to the tangential gradient), but even that information can be converted into a radial field [119].

In this section, various primary biomagnetic sensor configurations will be discussed. First, the method of sensor comparison will be reviewed in Section 6.1, radial and vector magnetometers will be compared in Section 6.2, and in Section 6.3, radial gradiometers will be optimized (baseline length optimization). Radial and planar gradiometers will be compared in Section 6.4, and the results of the sensor discussion will be summarized in Section 6.5.

## 6.1. METHOD OF SENSOR COMPARISON

Sensors will be compared by evaluating their signal-to-noise (S/N) ratio and their capability to accurately reconstruct one or several equivalent current dipoles in a spherical conducting medium. The reconstruction accuracy will be determined by Monte-Carlo simulations in the presence of either random or correlated noise, Figure 6.3. Generally, the reconstructed dipole positions produce an ellipsoidal cluster [111] with different standard deviations ( $\sigma_1, \sigma_2, \sigma_3$ ) along the three orthogonal directions. In the present discussion, the rms value of the three standard deviations,  $\sigma = [(\sigma_1^2 + \sigma_2^2 + \sigma_3^2)/3]$ , will be used as a measure of the dipole reconstruction accuracy.

The Monte-Carlo simulations were performed as a function of the number of channels,  $N$ , and for different rms noise levels. The  $N$  channels were distributed over  $N$  sites for magnetometers and radial gradiometers, over  $N/2$  sites for planar gradiometers (2 orthogonal sensors per site), and over  $N/3$  sites for vector magnetometers (3 orthogonal sensors per site). The sites were assumed to be uniformly distributed over a hemispherical sensor shell, Figure 6.4.a. The resulting  $\sigma$  as a function of the number of channels

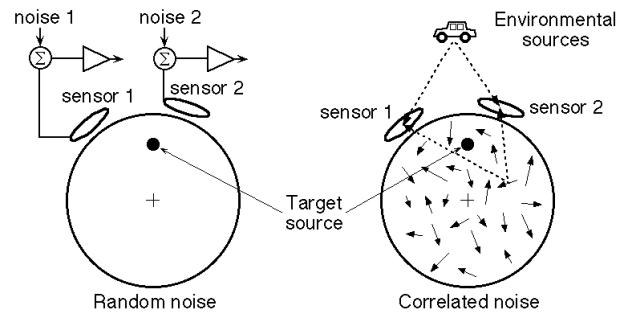


Figure 6.3. Biomagnetic sensors are exposed to random and correlated noise. (a) random noise sources usually originate in the SQUID sensors or electronics; (b) correlated noise can originate either within the brain or can be caused by environmental sources (e.g., moving dipoles, current wires, etc.).

is shown schematically in Figures 6.4.b and d for random and correlated noise. For random noise, the  $\sigma$  is decreasing with increasing number of channels as  $1/\sqrt{N}$ , and the random noise is spatially averaged. For correlated noise, the resulting  $\sigma$  becomes independent of the number of channels for large channel density. For correlated brain noise [24] the limiting  $\sigma$  is reached for  $N > 100$  channels, or for mean spacing between the channels of about 3 cm. This limiting channel density qualitatively corresponds to inter-channel spacing of the order of the noise correlation distance. Further increase of the channel density does not improve the S/N ratio, and the limiting error is reached.

The simulated results scale accurately with noise, and the standard deviation  $\sigma$  normalized by noise depends only on the number of channels, as in Figures 6.4.c and e. The scaling by noise also can be derived from expansion of the dipole equations in the vicinity of the true dipole position [112]. It has been found by examining the simulation results that the dependence of the standard deviation  $\sigma$  on the dipole depth and the sensor type can be explained approximately by inverse dependence on the peak signal [113],  $\text{Sig}_{\text{peak}}$ . Then the standard deviations for random,  $\sigma_r$ , and correlated,  $\sigma_c$ , noise can be expressed as

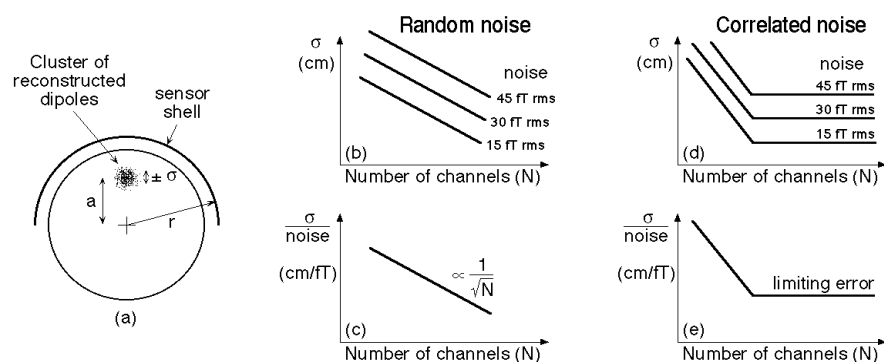


Figure 6.4. Dipole reconstruction accuracy (standard deviation,  $\sigma$ , of the cluster of reconstructed dipoles). (a) geometry for simulation of the effect of noise on dipole reconstruction accuracy,  $r = 10.7$  cm; (b, c) random noise; (d, e) correlated noise; (b, d)  $\sigma$  as a function of the number of channels,  $N$ , for noise levels of 15, 30 and 45 fT rms. Note the saturated (limiting)  $\sigma$  for larger number of channels ( $N > 100$ , or inter-sensor spacing of about 3 cm) for correlated noise; (c, e)  $\sigma/\text{noise}_{\text{rms}}$  as a function of  $N$ .

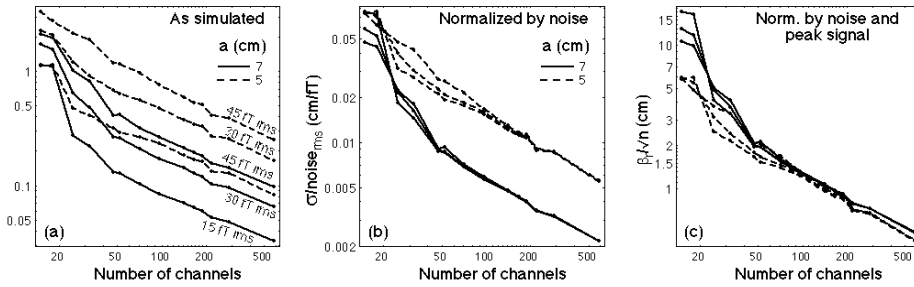


Figure 6.5. Demonstration of the effect of various normalizations on the dipole reconstruction error for random noise and radial magnetometers for dipole distances from the sphere center of  $a = 5$  and  $7$  cm. Random noise levels are  $15$ ,  $30$  and  $45$  fT rms, and the channels are uniformly distributed over the hemispherical sensor shell with radius  $r = 10.7$  cm,  $a = 5$  and  $7$  cm, dipole magnitude  $q = 10$  nA·m.

$$r \quad \frac{r \text{ noise}_{\text{rms}}}{\text{Sig}_{\text{peak}} \sqrt{n}} = \frac{r}{(S/N) \sqrt{n}} = \frac{d_r \text{ noise}_{\text{rms}}}{\text{Sig}_{\text{peak}} \sqrt{N}} \quad (6.1)$$

$$c \quad \frac{d_c \text{ noise}_{\text{rms}}}{\text{Sig}_{\text{peak}}} = \frac{d_c}{(S/N)} \quad (6.2)$$

where it has been assumed that for the correlated noise the number of channels is  $N > 100$  (for which  $d_c$  reaches the limiting error in Figure 6.4.e). The universal constants  $d_r$  and  $d_c$  are  $d_r = 0.44$  unitless and  $d_c = 2.5$  cm (or for a hemispherical sensor shell  $d_r = 12$  cm),  $n$  is the channel density ( $\text{cm}^{-2}$ ), and the signal-to-noise ratio,  $S/N$ , means the ratio of the peak signal,  $\text{Sig}_{\text{peak}}$ , to the rms noise,  $\text{noise}_{\text{rms}}$ . The accuracy of Eq.6.1 is illustrated in Figure 6.5 for radial magnetometers. In Figure 6.5.a the standard deviation, as

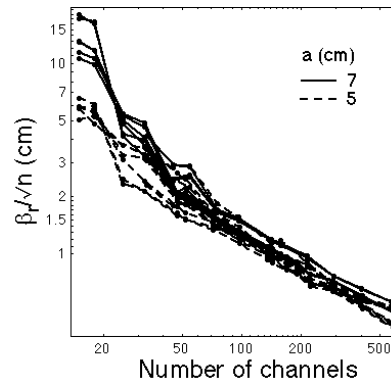


Figure 6.6. Dipole localization accuracy for random noise normalized by noise and by peak signal as a function of the number of channels and different sensor types. Dipole distances from the sphere center are  $a = 5$  and  $7$  cm, sensor shell is hemispherical with radius  $r = 10.7$  cm, and random noise levels are  $15$ ,  $30$  and  $45$  fT rms. Sensor types are: radial magnetometers, vector magnetometers, radial gradiometers ( $d = 5$  cm), and planar gradiometers ( $d = 1.65$  cm). The  $N$  channels are distributed over  $N$  sites for radial magnetometers and gradiometers, over  $N/3$  sites (3 orthogonal sensors per site) for vector magnetometers, and over  $N/2$  sites (2 orthogonal sensors per site) for planar gradiometers and the site distribution is uniform.

simulated, shows the dependence on noise and dipole distance from the sphere center,  $a$ . In Figure 6.5.b, the standard deviation normalized by noise is shown. The plots, for a larger number of channels, are independent of the noise level and depend only on dipole position,  $a$ . In Figure 6.5.c the complete normalization of  $\sigma$  by noise and by peak signal (quantity  $\sigma/\mu$ ) is shown. For  $N > 80$  (which corresponds to inter-sensor spacing of about 3.4 cm) the curves for all noise values and dipole positions coincide.

The accuracy of Eq.6.1 for different types of sensors (e.g., radial magnetometers, vector magnetometers, radial gradiometers and planar gradiometers) is shown in Figure 6.6. For  $N > 80$  the plots for all noise levels, dipole positions  $a = 5$  and 7 cm and all sensor types are very close together, and indicate that Eq.6.1 is reasonably universal. Similar results were obtained also for Eq.6.2.

## 6.2. RADIAL AND VECTOR MAGNETOMETERS

For random noise, the standard deviation normalized by noise for radial and vector magnetometers was computed as a function of the number of channels by simulation and also by using expansion of dipole equations [112]. The dipole source was located on the sensor array axis at two positions,  $a = 5$  cm (deep below the sphere surface) and  $a = 7$  cm (shallow, or close to the sphere surface). The results are plotted in Figure 6.7 and show that for both investigated dipole positions, the radial magnetometers give better results (i.e., smaller standard deviation  $\sigma$ ).

The comparison of dipole reconstruction accuracy when the dipole is not on the axis of the sensor array is shown in Figure 6.8 for random and correlated noise. For random noise, Figure 6.8.b, the radial magnetometers give better results (smaller  $\sigma$ ) for dipoles positioned even outside the sensor array (up to about 2.5 rad from the vertex for a hemispherical sensor shell). For correlated noise, Figure 6.8.c, the radial and vector magnetometers give similar results for dipoles located well within the sensor array (up to

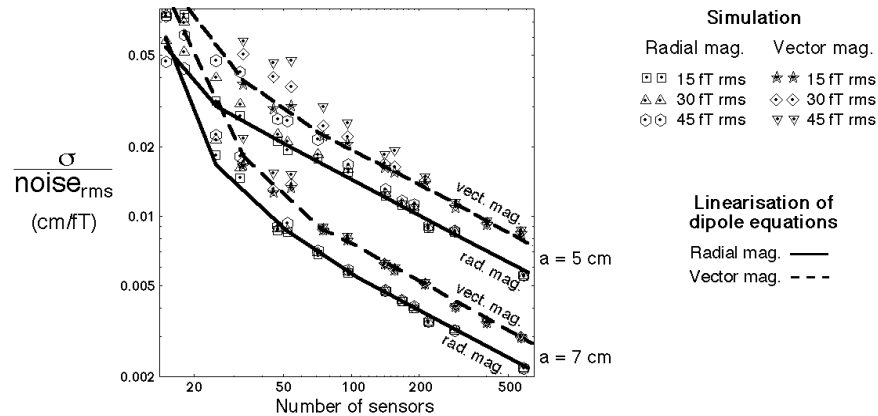


Figure 6.7. Comparison of standard deviation normalized by rms noise magnitude for radial and vector magnetometers as a function of the number of channels for Monte-Carlo simulation and direct calculation by linearisation of dipole equations. Random noise, 15, 30 and 45 fT rms,  $a = 7$  and 5 cm, hemispherical sensor shell  $r = 10.7$  cm, dipole moment  $q = 10$  nA-m, one radial magnetometer per site, three vector magnetometers per site, sites uniformly distributed over the sensor shell area. Solid and dashed lines - calculation from linearisation of dipole equations for radial and vector magnetometers, symbols - Monte-Carlo simulation.

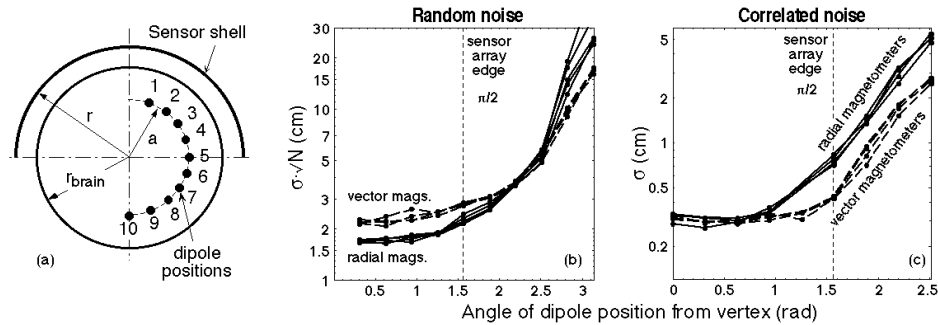


Figure 6.8. Comparison of radial and vector magnetometers at the sensor array edge, plot of  $\sigma_r/N$  for random and  $\sigma$  for correlated noise as a function of the angle of dipole position from vertex. Each value of  $\sigma_r/N$  was determined by 200 Monte-Carlo simulations and the correlated noise was simulated using 1,000 randomly distributed, random amplitude dipoles in the model sphere with radius  $r_{\text{brain}} = 8$  cm. Hemispherical sensor shell,  $r = 10.7$  cm,  $a = 7$  cm, position 1 corresponds to 18 deg from vertex, and all subsequent positions are in 18 deg increments, position 5 corresponds to the dipole at the sensor array edge. Number of radial magnetometers used  $N = 97, 142, 190, 289, 586$ , and the number of vector magnetometers used 96, 141, 291, 570 (number of vector magnetometer sites 32, 47, 97, 190), lines in (b) and (c) correspond to constant number of channels, solid lines - radial magnetometers, dashed lines - vector magnetometers. Thin vertical dashed line corresponds to sensor array edge. (a) geometry for the calculation; (b) results for random noise of 30 fT rms; (c) results for correlated noise of 30.4 fT rms for radial magnetometers and 22.5 fT rms for vector magnetometers (mean rms value over all three vector components), the two different noise values correspond to the same random distribution of dipoles.

about 1 rad from the vertex), but for the dipoles close to or outside the sensor array edge, the vector magnetometers give better results (smaller  $\sigma_r/N$ ). For correlated noise, the vector magnetometers are better at "extrapolating" when the dipole is far from the sensor array axis.

The results in Figure 6.8 are independent of the number of channels (each line corresponds to a constant number of channels, and the lines for different numbers of channels yield roughly the same results).

### 6.3. RADIAL GRADIOMETERS

It was shown in Section 4 that, even within shielded rooms, the detection of biomagnetic fields is not possible with magnetometers, and noise cancellation using references must be performed. The references are used to remove noise from magnetometers and can lead to 1st- or higher-order noise cancellation. Similarly, the primary sensors could be 1st-order hardware gradiometers, and references are used to provide higher-order noise cancellation. In both cases, the noise cancellation is performed with either gradiometer or adaptive coefficients. Both magnetometer and hardware 1st-order gradiometer sensors, after the first level of noise cancellation, represent a 1st-order system (either gradiometer or adaptive), and this section will discuss the optimization of the primary 1st-order baseline, defined as in Figure 6.9.

The baseline optimization will be developed first for hardware gradiometers, and then it will be extended to synthetic gradiometers and adaptive systems. The baseline will be optimized by considering an interplay between the detected signal strength and the device sensitivity to environmental noise.

It was shown in Section 4, that even within shielded rooms, the environmental noise is not negligible and affects the SQUID detectors. The detected noise is clearly of

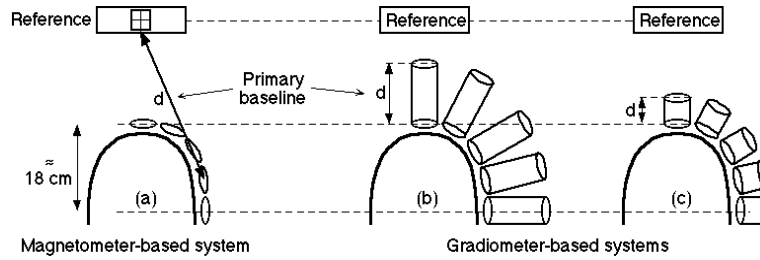


Figure 6.9. Distinction between magnetometer- and gradiometer-based systems, and between systems with different baseline lengths. (a) magnetometer-based system with sensors close to a helmet surface and reference at some distance away; the baselines are quite long, and both the 1st-order and high-order baselines are different for different channels; (b, c) hardware 1st-order gradiometer-based systems, the 1st-order gradiometer baseline is the same for all channels, only high-order gradiometer baselines are different for different channels; (b) longer 1st-order baseline; (c) shorter 1st-order baseline.

environmental origin, because it depends on the time of the day and can be reduced by high-order gradiometers (Figures 4.5.b and 4.19). A simple representation of SQUID detector noise is shown in Fig.6.10.a. The SQUID noise consists of white-noise (of instrumental origin) and of low-frequency noise (of environmental origin), Eq.5.4. The dependence of the low-frequency noise on baseline length - see Section 4.4 - can be expressed as

$$A = A_0 d / d_0 \quad (6.3)$$

where the constant  $A$  corresponds to baseline  $d$ , and constant  $A_0$ , to baseline  $d_0$ . The onset of low-frequency noise can be defined as a point where the white noise is equal to the low-frequency noise,  $n_w = n_{low}$ . If  $f_0$  is the low-frequency noise onset corresponding to baseline  $d_0$  and  $f_{od}$  to baseline  $d$ , then

$$f_{od} = k \sqrt{\frac{A_0}{n_w}} \frac{d}{d_0} = k \sqrt{\frac{A}{n_w}} = f_0 k \sqrt{\frac{d}{d_0}} \quad (6.4.a)$$

and

$$f_0 = k \sqrt{\frac{A_0}{n_w}} \quad (6.4.b)$$

Using Eqs.5.4, 6.3 and 6.4, the low-frequency noise may be expressed as

$$n_{low} = n_w \frac{d}{d_0} \left( \frac{f_0}{f} \right)^k \quad (6.5)$$

The total noise detected by the SQUID flux transformer is a combination of white and low-frequency noise,  $n_T^2 = n_{low}^2 + n_w^2$ , and

$$n_T^2 = \frac{n_w^2}{N_{ave}} \left( 1 + \frac{d}{d_0} \right)^2 \left( \frac{f_0}{f} \right)^{2k} \quad (6.6)$$

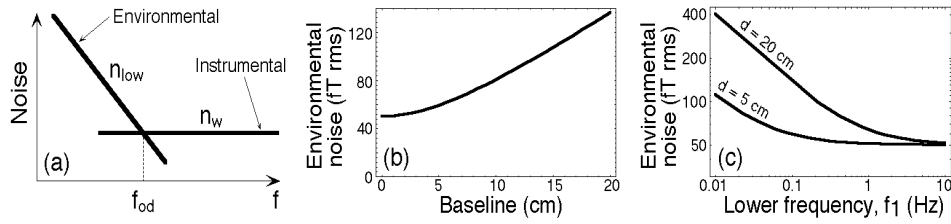


Figure 6.10. Noise of a SQUID detector exposed to low-frequency environmental noise.  $f_o = 2$  Hz,  $d_o = 5$  cm,  $n_w = 5$  fT rms/ Hz,  $N_{ave} = 1$ ,  $k = 1$ ,  $f = 100$  Hz. (a) representation of low-frequency and white noise on log-log plot; (b) total noise as a function of baseline length,  $f_1 = 0.1$  Hz; (c) total noise as a function of  $f_1$  for  $d = 5$  and 20 cm.

where it has been assumed that the measured signal was averaged  $N_{ave}$  times. Usually, the measurement is performed in a frequency range from  $f_1$  to  $f_1 + f$ . The total rms noise in this bandwidth is obtained by integration of Eq.6.6

$$n_{rms} = \sqrt{\int_{f_1}^{f_1+f} n_T^2 df} = \frac{n_w}{\sqrt{N_{ave}}} \sqrt{f + \frac{f_1}{(2k-1)} \frac{d}{d_o} \frac{f_o}{f_1} \frac{2k}{1 - \frac{f_1}{f_1+f}}} \quad (6.7)$$

The detected noise now depends on the noise parameters  $n_w$ ,  $f_o$ ,  $f_1$ ,  $f$ ,  $k$ , and baselines,  $d$  and  $d_o$ . The behavior of Eq.6.7 as a function of baseline,  $d$ , and the lowest frequency of interest,  $f_1$ , is shown graphically in Figures 6.10.b and c. The total noise is monotonically increasing as a function of baseline and is decreasing as the lowest frequency of interest is increasing. If the lowest frequency of interest is larger than the onset of low frequency noise,  $f_1 > f_{od}$ , then the system operation is completely in the white-noise region, Eq.6.7 simplifies to  $n_{rms} = n_w / \sqrt{N_{ave}}$  and there is no dependency of the detected noise on  $b$  or  $f_1$  (such situation is usually not observed in practice).

The dependence of signal strength on baseline can be determined by considering the peak signal magnitude of a single current dipole source in a spherical medium, as in Figure 6.11.a [63]. The peak signal was calculated as a function of radial gradiometer baseline, and the results were normalized by the peak magnetometer signal strength. The results are shown for different dipole distances from the sphere center in Figure 6.11.b.

As the baseline increases, the normalized gradiometer signal strength approaches 1 (magnetometer signal strength). The signal strength increase with baseline is fastest for

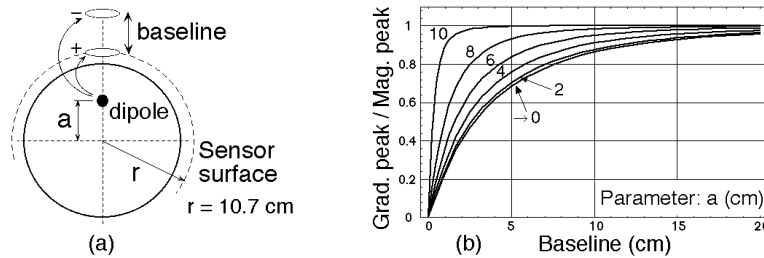


Figure 6.11. Determination of radial gradiometer peak signal as a function of baseline. (a) calculation geometry; (b) gradiometer peak signal normalized by magnetometer ( $d = 0$ ) peak signal. Adapted from reference [114].

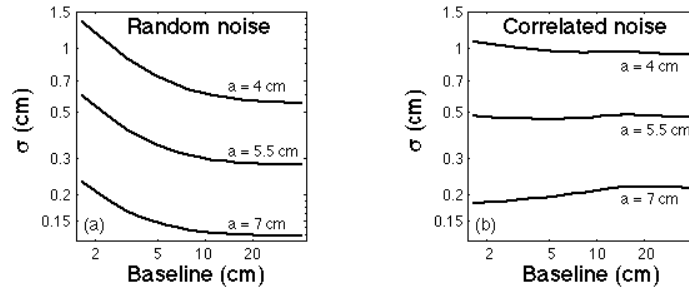


Figure 6.12. Comparison of dipole reconstruction accuracy,  $\sigma$ , for random and correlated brain noise as a function of baseline length. Sensor shell radius  $r = 11$  cm, dipole moment magnitude  $q = 20$  nA·m,  $n_w = 5$  fT rms/ Hz,  $a = 4, 5.5,$  and  $7$  cm. (a) random noise, number of sensors  $N = 150$ , bandwidth =  $100$  Hz,  $N_{ave} = 1$ ,  $d_c = 12$  cm; (b) correlated noise, bandwidth =  $100$  Hz,  $N_{ave} = 100$ ,  $d_c = 2.5$  cm, brain noise is given as a function of baseline as in Figure 6.23 at a distance from the head of  $1.9$  cm.

shallow dipoles and slowest for deepest dipoles. The curve marked by  $\infty$  in Figure 6.11.b corresponds to the limit where the current dipole approaches the sphere center.

Alternatively, the dependence of signal strength on baseline can be expressed in terms of the dipole reconstruction accuracy,  $\sigma$  - see Section 6.1. For random noise,  $\sigma$  as a function of baseline for different dipole distances from the sphere center  $a = 4, 5.5,$  and  $7$  cm is shown in Figure 6.12.a. As the baseline increases, the signal strength also increases (as in Figure 6.11.b), and the dipole reconstruction accuracy improves, i.e.,  $\sigma$  decreases. For correlated noise, Figure 6.12.b,  $\sigma$  is nearly independent of the baseline, as the calculations for the correlated noise were performed in the region of "limiting error" in Figure 6.4.e.

The signal strength also has been represented by the rms value of the signal computed over all channels. This representation was found to be close to the peak signal results and since the peak signal calculations are simpler, they were used for the present demonstration of the baseline optimization.

The principle of baseline optimization is shown in Figure 6.13 [114]. The detected noise and signal magnitudes both increase with increasing baseline, however, because of their functional differences, the S/N ratio peaks at a certain "optimal" baseline.

Examples of the actual S/N ratio curves are shown in Figure 6.14 for shallow and deep dipoles for different onsets of low-frequency noise,  $f_o$ . As  $f_o$  decreases, the positions of the S/N ratio maxima and therefore the optimal baselines increase. For no low-frequency noise ( $f_o = 0$  Hz), the optimal baseline is infinitely long. The optimization curves are only weakly dependent on the dipole depth, and their shapes are independent of the number of averages,  $N_{ave}$ .

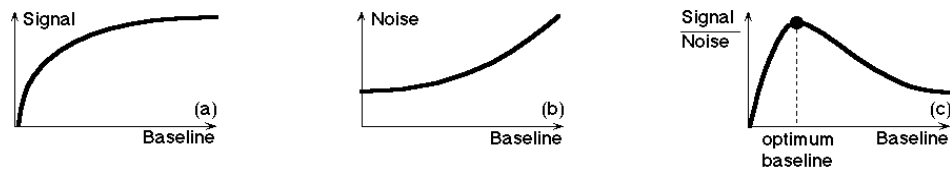


Figure 6.13. Principle of baseline optimization for hardware 1st-order gradiometers. (a) dependence of signal strength on baseline; (b) dependence of detected noise on baseline; (c) dependence of S/N ratio on baseline. Adapted from reference [114].

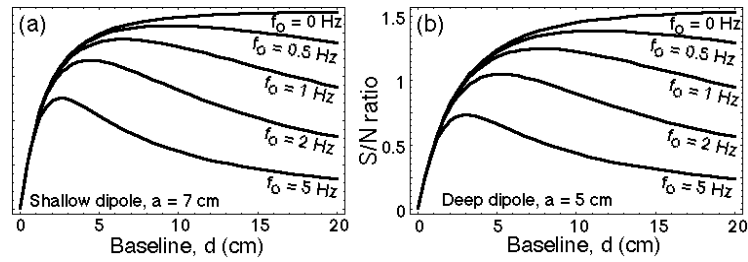


Figure 6.14. Plots of S/N ratio as a function of baseline length.  $d_0 = 5$  cm,  $k = 1$ ,  $n_w = 5$  fT rms/ Hz,  $f_1 = 0.1$  Hz,  $f = 100$  Hz,  $N_{\text{ave}} = 1$ ,  $r = 10.7$  cm,  $q = 10$  nA-m. (a) shallow dipole,  $a = 7$  cm; (b) deep dipole,  $a = 5$  cm.

The general baseline optimization method is shown in Figure 6.15. The S/N ratio surface as a function of  $f_0$  and  $d$  is constructed for given noise parameters and the required collection frequencies  $f_1$  and  $f$  (Figure 6.15.c). Then, for a given  $f_0$ , the maximum S/N ratio is found, and the corresponding optimal baseline is determined. This procedure yields short baselines for large values of  $f_0$  and longer baselines for small  $f_0$ 's.

The above baseline optimization was developed for 1st-order hardware radial gradiometers. Hardware gradiometers always reduce the detected signal magnitude, while the synthetic gradiometers may reduce or increase it. A simple model of this behavior is shown in Figure 6.16 where the synthetic gradiometers consist of magnetometer sensors and a vector magnetometer reference located at a fixed position, e.g., above the region of negative signal, as in Figure 6.16.b. The reference also will detect the negative signal and depending on whether it is subtracted from the magnetometers in the negative or positive regions, the total synthetic gradiometer output will be either reduced or increased. The above explanation is grossly simplified, as in reality the effective reference orientation will be different for different magnetometers. However, the character of the synthetic gradiometer behavior is correctly captured by this simple model.

Therefore, for synthetic 1st-order gradiometers, depending on the source position relative to the reference, the signal strength is the same or larger than for the hardware gradiometers (and the hardware gradiometers represent the worst-case limit of the synthetic gradiometers). Since the white-noise levels and the environmental noise rejection

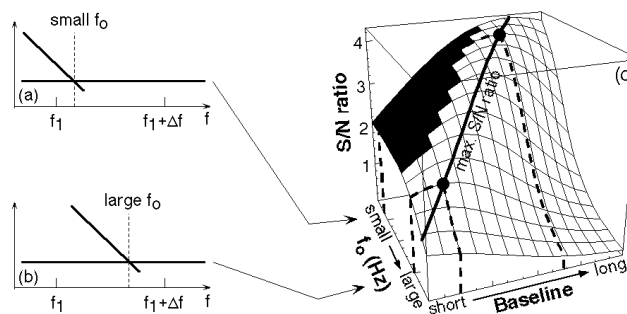


Figure 6.15. Method of baseline optimization. (a) small onset of low-frequency noise,  $f_0$ ; (b) large onset of low-frequency noise,  $f_0$ ; (c) plot of S/N ratio as a function of low-frequency noise onset,  $f_0$ , and baseline,  $d$ . Solid line indicates the maximum of S/N ratio. Adapted from reference [114].

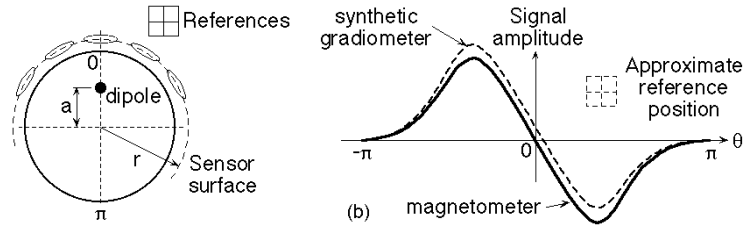


Figure 6.16. Simplified model demonstrating the effect of a synthetic gradiometer on the detected signal. (a) geometry of a 1st-order synthetic gradiometer; (b) magnetometer (solid line) and synthetic gradiometer (dashed line) signals. Adapted from reference [114].

are similar for both types of gradiometers, baseline optimization for synthetic gradiometers leads to the same or shorter baselines than for the hardware gradiometers. Since the optimization is most important in situations where the signals are weakest, the synthetic gradiometers should be optimized in their worst-case limit, which is the hardware gradiometer. Similar arguments also apply to adaptive systems.

Optimization of the primary sensor baseline for higher-order synthetic gradiometers is similar to the procedures for the 1st-order gradiometers. The effect of higher-order gradiometer references can generally be neglected [80], and these gradiometers are then optimized as 1st-order gradiometers, except that the noise parameters  $f_o$ ,  $k$ ,  $n_w$  correspond to the noise detected by the high-order gradiometers.

The noise character, as discussed above, also was verified experimentally. A standard 64-channel MEG system [80] with 1st-order hardware gradiometers as primary sensors ( $d = 5$  cm) has been equipped with high-sensitivity reference vector magnetometers and four additional magnetometer-based synthetic noise cancellation channels (as in Figure 4.7.a) with baselines of  $d = 10.7$ ,  $18.3$ ,  $24.4$ , and  $32.9$  cm. These additional channels were balanced as synthetic 1st- or 2nd-order gradiometers (fixed coefficients). Their level of balance was evaluated using a rotating magnet [115] and it was found to be similar to that of the standard gradiometer-based channels. Noise spectra of the synthetic gradiometers with different baselines, as measured in a shielded room, are shown in Figure 6.17.

The environmental low-frequency noise in Figure 6.17 increases with increasing baseline. The noise parameters were extracted at 0.5 Hz and are shown in Figure 6.18 as

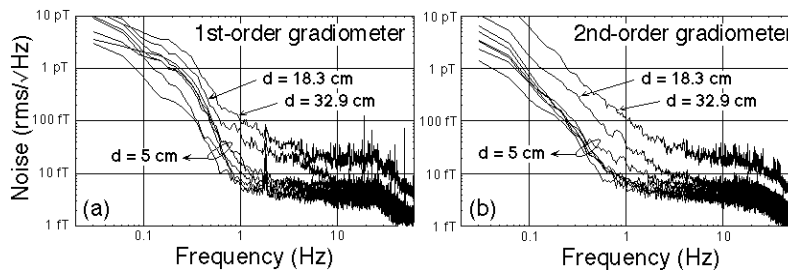


Figure 6.17. Spectra of hardware and synthetic gradiometers with different primary baselines, collected in a shielded room. Spectra of 6 gradiometer-based channels with the primary hardware baseline  $d = 5$  cm and two magnetometer-based channels with primary synthetic gradiometer baselines of  $d = 18.3$  and  $32.9$  cm are shown. (a) 1st-order hardware and synthetic gradiometers; (b) 2nd-order synthetic gradiometers. Adapted from reference [114].

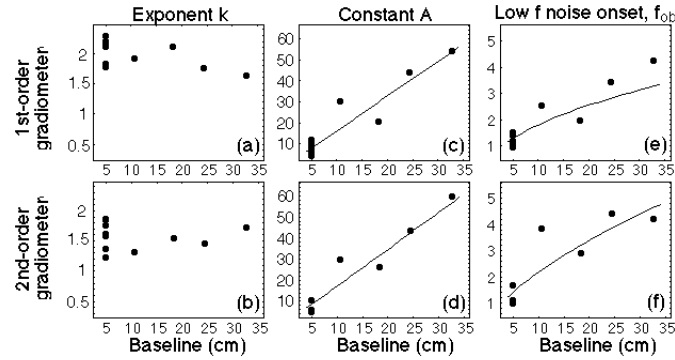


Figure 6.18. Low-frequency noise parameters measured at frequency  $f = 0.5$  Hz from noise spectra as in Figure 6.16. (a, b) low-frequency noise slope  $k$ ; (c, d) constant  $A$  ( $\text{fT}\cdot\text{Hz}^{k-0.5}$ ); (e, f) low-frequency noise onset  $f_{\text{od}}$  (Hz). Adapted from reference [114].

a function of baseline. The exponent  $k$  in Figures 6.18.a and b is nearly constant,  $k = 2$  and  $k = 1.5$  for 1st- and 2nd-order gradiometers, respectively. The measured constant  $A$  (dots) and a linear least-squares fit according to Eq.6.3 (straight line) are shown in Figures 6.18.c and d. The measured onset of low-frequency noise projected to  $n_w = 5$  fT rms/ Hz is shown in Figures 6.18.e and f (dots) together with the expected dependence on baseline ( $f_{\text{od}} \propto b^{1/k}$  or  $A^{1/k}$ , Eq.6.4) using parameters from Figures 6.18.a to d (solid line). In all cases the correspondence between the measurement and expectation based on Eqs.5.4, 6.3 and 6.5 is satisfactory.

Noise parameters determined in shielded rooms at four different MEG sites are listed in Table 6.1. Because they depend on the time of the day and the environmental activity level, they are shown as ranges.

Location		Gradiometer order		
		1st	2nd	3rd
Osaka <sup>a</sup>	$f_o$ (Hz)	1	0.6	0.5 - 1
	$k$	2	1.5 - 1.8	1
Sendai	$f_o$ (Hz)	1	0.5	0.3
	$k$	2.5 - 3	2.5	1 - 1.2
Vienna	$f_o$ (Hz)	1 - 4	---	0.5 - 2
	$k$	2.5	---	0.9 - 2
Amsterdam	$f_o$ (Hz)	1.3 - 2	1.4 - 2	---
	$k$	1.8 - 2.6	1.6 - 1.9	0.5 - 0.9

<sup>a</sup> only the night data were available      --- parameters not determined

Baseline optimization for the Amsterdam site (last row in Table 6.1) is shown in Figure 6.19. The optimal baseline is plotted as a function of  $f_o$  and  $f_1$ , and the hatched band corresponds to the appropriate range of observed  $f_o$ 's. If  $f = 100$  Hz and the lowest frequency of interest were  $f_1 = 1$  Hz, then the optimum baseline would be in the range of about 5 - 8 cm and 7 - 10 cm for 1st- and 2nd-order gradiometers, respectively. However, because of the need to correctly determine the data offset, the lowest frequency of interest, even for evoked responses, is usually less than 1 Hz. Then considering  $f_1$  in the

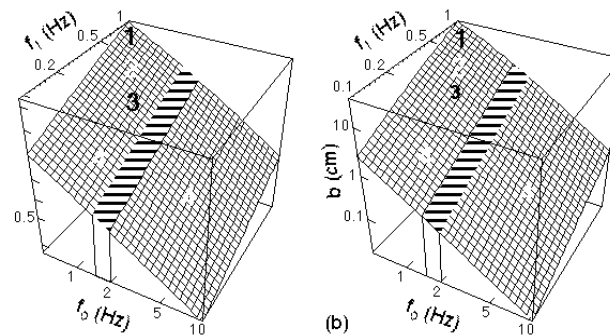


Figure 6.19. Plot of optimum baseline as a function of low-frequency noise onset  $f_o$  and the minimum frequency of interest,  $f_i$ .  $r = 10.7$  cm,  $a = 4$  cm,  $q = 50$  nA-m,  $n_w = 5$  fT rms/ Hz,  $d_o = 5$  cm,  $f = 20$  Hz,  $N_{ave} = 1$ . Regions 1:  $d > 15$  cm, 2:  $8$  cm  $< d \leq 15$  cm, 3:  $5$  cm  $< d \leq 8$  cm, 4:  $d \leq 5$  cm. (a)  $k = 1.85$ , 2nd-order gradiometer; (b)  $k = 2.6$ , 1st-order gradiometer. Adapted from reference [114].

range from 0.2 to 0.5 Hz, the optimal primary sensor baseline is about 1.5 - 3.5 cm and 2 - 6 cm for 1st- and 2nd-order gradiometers, respectively. Increasing the gradiometer order increases the optimal baseline, but even for 2nd-order gradiometers, the optimal baseline remains relatively short. For 1st-order gradiometers, the short optimal baseline also was suggested by ter Brake [116].

The baseline optimization for other MEG systems in Table 6.1 results in similarly short baselines. The optimization for 3rd-order synthetic gradiometers would lead to somewhat longer primary baselines (because the environmental noise is significantly reduced). However, such systems have not been discussed because long primary baselines would cause the 3rd-order gradiometers to have increased white-noise levels.

Comment on the selection of the lowest frequency of interest: The lowest frequency of interest depends on the measurement paradigm and will differ widely in different studies. However, the measurement of evoked signals is probably one of the more universally performed experiments and can serve as a model for discussion of the lowest frequency of interest. The width of the evoked signal is about 50 msec, Figure 6.20 (e.g., [22, 23]), and it corresponds to relatively high frequencies of about 3 Hz. However, it is not sufficient to determine the "high frequency" peak with good S/N ratio, it is also necessary to determine the signal offset level with good S/N ratio. The offset is determined from the pre-stimulus time interval, which is usually in the range from 0.2 to 0.5 sec and therefore corresponds to a frequency range from 0.3 to 0.8 Hz. Thus, even

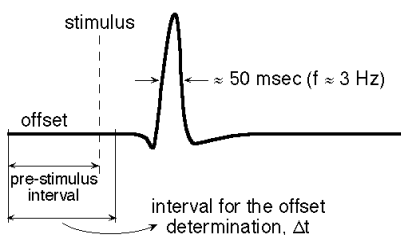


Figure 6.20. Stylized MEG evoked signal. Signal width is about 50 msec ( $\approx 3$  Hz), and signal offset is determined on a time interval  $\Delta t$ , roughly equal to the pre-stimulus interval.

though a relatively high-frequency signal is measured, it is necessary to have a good S/N ratio at low-frequencies and typically,  $f_1 < 1$  Hz.

The sensor baseline has been optimized by considering the interplay between the signal strength and the ability to reject environmental noise. The S/N ratio was deemed to be the most important sensor parameter, and the optimum baseline was defined by its maximum. The optimization was applied to the noise data from four existing MEG installations, and in all cases the optimal baseline was found to be short, less than 5 to 10 cm. The baseline optimization was performed assuming that the investigated systems are unconditionally rigid. However, the rigidity rapidly decreases with increasing baseline, and longer, less rigid baselines will lead to additional degradation of the S/N ratio. Thus, the requirements for short baselines also are consistent with common sense considerations of mechanical stability.

#### 6.4. RADIAL AND PLANAR GRADIOMETERS

Comparison of radial and planar gradiometer signal strengths as a function of the source depth is shown in Figure 6.21. An equivalent current dipole was positioned at a distance  $a$  from the center of a conducting sphere and magnetometer, radial and planar gradiometers were each located at a position of their maximum signal strength, Figure 6.21.a. In order to remove the steep dependence on the depth, the results were normalized by the peak magnetometer signal. Unless otherwise stated, all calculations were performed for "point" detectors, i.e., the radii of all flux transformer coils were assumed to be zero.

The plot of the normalized peak signals as a function of dipole depth is shown in Figure 6.21.b. The radial magnetometer corresponds to a horizontal line at the value of 1 (because the results were normalized by magnetometer peak signal). For radial gradiometers, as the baseline length decreases, the signal strength also decreases (similar to Figure 6.11.b). The planar gradiometers show a strong signal for superficial sources and fast signal decrease when the current source is deeper. This rapid loss of signal strength also is reflected in the dipole reconstruction accuracy,  $\xi$ , in Figure 6.22, when random noise is considered. For the most frequently-used radial and planar gradiometers,  $\xi$  is smaller (better reconstruction) for radial than for the planar gradiometers.

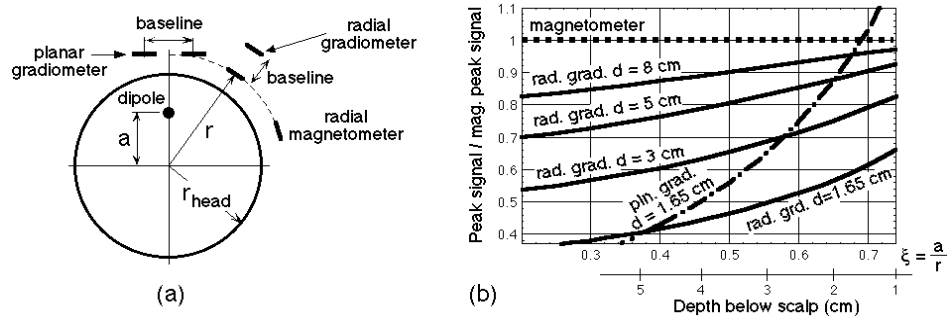


Figure 6.21. Comparison of detected signal strengths for various types of sensors. (a) geometry of the calculation, for each dipole position, each sensor is assumed to be located at a position of its maximum signal,  $r = 11$  cm,  $r_{\text{head}} = 9.1$  cm; (b) peak signals normalized by magnetometer peak signal as a function of normalized dipole position,  $a/r$ . Dashed line - magnetometer, solid lines - radial gradiometers with baselines of 8, 5, 3, and 1.65 cm, chain line - planar gradiometer with baseline of 1.65 cm.

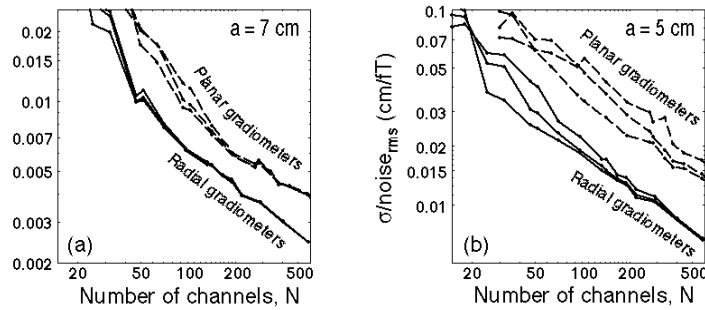


Figure 6.22. Comparison of dipole localization accuracy,  $\sigma/\text{noise}_{\text{rms}}$ , for radial and planar gradiometers and for random noise. Sensor shell radius  $r = 10.7$  cm, dipole magnitude,  $q = 10$  nA-m, radial gradiometer baseline  $d = 5$  cm, planar gradiometer baseline  $d = 1.65$  cm, radial gradiometers are uniformly distributed on the sensor shell surface at  $N$  sites, planar gradiometers are uniformly distributed at  $N/2$  sites (two orthogonal channels per site), noise values 15, 30, and 45 fT rms. Solid lines - radial gradiometers, dashed lines - planar gradiometers. (a)  $a = 7$  cm, shallow dipole; (b)  $a = 5$  cm, deep dipole.

A similar result also was obtained when the sensor array information content [117] was considered. The channel capacity of 122-channel planar gradiometer system was compared with an array of a 122-channel radial gradiometer system. It was found that the channel capacity grows approximately linearly with the number of channels, with the planar 122-channel array giving 10% less bits than the radial array [24].

When correlated brain noise is considered, it is found that the noise magnitude depends on the sensor type (radial or planar) and on the gradiometer baseline. Results from [24], recomputed for a larger range of baselines, are shown in Figure 6.23, where the correlated brain noise is plotted as a function of distance from the surface of the head. The magnetometer (radial gradiometer with  $d = 9$  cm) detects the largest noise, and as the radial gradiometer baseline length decreases, the detected brain noise also decreases. The brain noise rms value detected by the planar gradiometer with  $d = 1.65$  cm is about 1/2 of that detected by the radial gradiometer with baseline  $d = 5$  cm.

The differences between the dipole reconstruction accuracies,  $\sigma/\text{noise}_{\text{rms}}$ , for random and correlated noise and for different types of detectors are shown in Figure 6.24. The

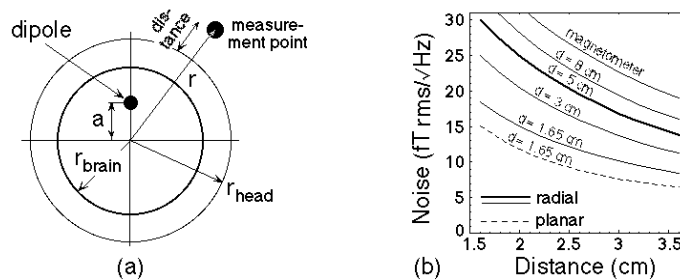


Figure 6.23. Simulated magnitudes of the correlated brain noise for magnetometers and radial and planar gradiometers with different baselines.  $r_{\text{head}} = 9.1$  cm,  $r_{\text{brain}} = 8$  cm, position of the measurement point varied in the range of  $r = 10.7$  to  $12.7$  cm. Results in this figure were computed as in [24] and expanded to a larger range of baselines. (a) geometry of computation; (b) simulated brain noise as a function of distance from the scalp surface. Solid lines - radial gradiometers, dashed line - planar gradiometer.

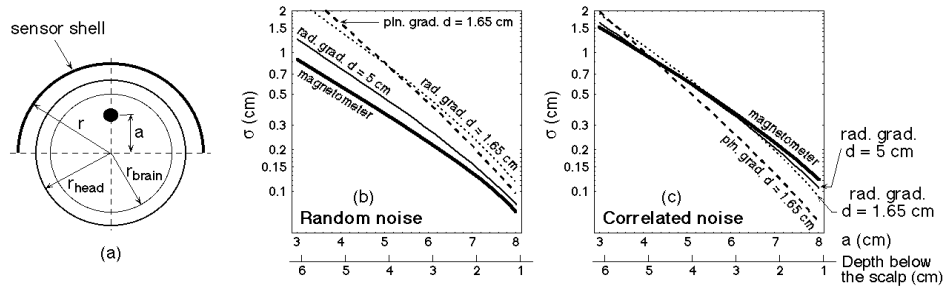


Figure 6.24. Standard deviation of the dipole reconstruction cluster as a function of dipole position for random and correlated noise and for magnetometer, radial gradiometers with 5 and 1.65 cm baselines, and planar gradiometer with 1.65 cm baseline. Sensor shell radius  $r = 11$  cm,  $r_{\text{head}} = 9.1$  cm,  $r_{\text{brain}} = 8$  cm. Magnetometer and radial gradiometer coil areas  $1.77 \times 1.77 \text{ cm}^2 = 3.14 \text{ cm}^2$ , planar gradiometer coil areas  $1.65 \times 3.3 \text{ cm}^2 = 5.44 \text{ cm}^2$ . (a) geometry for computation; (b) random noise,  $n_w = 5$  fT rms/ Hz, bandwidth = 100 Hz,  $N_{\text{ave}} = 1$ ,  $\text{noise}_{\text{rms}} = 50$  fT rms,  $N = 150$  channels,  $d_r = 12$  cm; (c) correlated noise, bandwidth = 100 Hz,  $N_{\text{ave}} = 100$ ,  $d_c = 2.5$  cm, and brain noise is dependent on the type of flux transformer, as in Figure 6.23. Considering the distance from the head of 1.9 cm,  $n_{\text{brain}} = 26$  fT rms/ Hz for radial gradiometer with  $d = 5$  cm and  $n_{\text{brain}} = 12.5$  fT rms/ Hz for planar gradiometer with  $d = 1.65$  cm.

random noise result is relevant in situations where the spontaneous signal is investigated and little or no averaging is done (the background brain "noise" is considered a signal), while the correlated noise result is relevant in situations where the evoked signals are investigated with data averaging (and the background brain signal is considered to be noise). Thus, no averaging was performed in the calculations in Figure 6.24.b for the random noise, and data from 100 collections were averaged in Figure 6.24.c for correlated noise.

For random noise in Figure 6.24.b, the dipole reconstruction accuracy,  $\sigma$ , for a planar gradiometer (dashed line) is worse than for the magnetometer or radial gradiometer with  $d = 5$  cm and is about equal to the radial gradiometer with  $d = 1.65$  cm. This behavior reflects the results already obtained in Figures 6.21 and 6.22. For correlated noise in Figure 6.24.c,  $\sigma$  for planar gradiometers is smaller than that for radial gradiometers or magnetometers, especially for superficial dipoles [24]. Thus, in the case of correlated noise, the reduced sensitivity of planar gradiometers to deep sources also results in lower detected brain noise levels, with the net result that the  $\sigma$  for planar gradiometers is smaller than for radial gradiometers or magnetometers (in fact, the magnetometer performance is worst in this regime). The calculations in Figure 6.24 were performed for flux-transformer coils with finite dimensions. However, the results were basically unchanged when "point" coils were used instead.

There are other source configurations which should be examined when comparing planar and radial gradiometers. First, consider quadrupole sources as in Figure 6.25, where the ratio of detected maximum signal strengths of radial and planar gradiometers is shown as a function of quadrupole distance from the sphere center,  $a$ . If the ratio is  $> 1$ , the signal strength of the radial gradiometers is larger, and if it is  $< 1$ , the signal strength of the planar gradiometers is larger. For comparison, the ratio for a single current dipole is shown by a thick line. The antiparallel "dipoles in line" in Figure 6.25.a favor planar gradiometers (the ratio is smaller than for a single dipole) and the antiparallel "side-by-side" dipoles in Figure 6.25.b strongly favor radial gradiometers (the ratio is larger than for a single dipole).

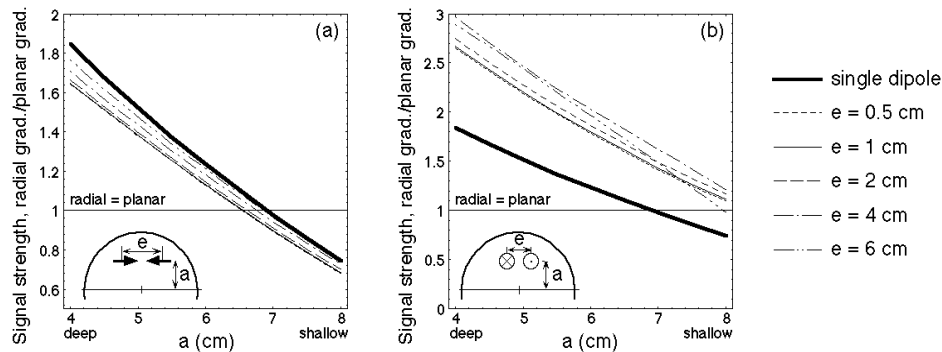


Figure 6.25. Ratio of signal strengths of radial to planar gradiometers for quadrupole sources. Radial gradiometer baseline  $d = 5$  cm, planar gradiometer baseline  $d = 1.65$  cm, each device is positioned at a point of its maximum signal. Distances between the quadrupole sources  $e = 0.5, 1, 2, 4,$  and  $6$  cm, dipole moments  $q = 10$  nA·m, radius of sensor shell  $r = 10.7$  cm. Thin horizontal line corresponds to the case when maximum signal strengths of radial and planar gradiometers are equal, thick solid line corresponds to a single dipole ratio. (a) two antiparallel dipoles "in-line"; (b) two antiparallel dipoles "side-by-side".

Second, consider the sensitivity to extended sources. A simple linearly-extended source was modeled as in Figure 6.26.a, and the maximum signal of radial and planar gradiometers was computed as a function of source length for various distances from the sphere center,  $a$ , Figure 6.26.b. The reduction of the detected signal strength as a function of the source length is larger for planar gradiometers (dashed lines in Figure 6.26.b) than for radial gradiometers. The ratio by which the planar gradiometers are less sensitive to the extended sources than the radial gradiometers is shown in Figure 6.26.c for different source positions,  $a$ .

The presence of extended sources decreases or eliminates the advantage of planar gradiometers in the case of correlated noise, and makes them even more disadvantageous in the case of random noise. This is shown in Figure 6.27, where the S/N ratio normalized by that of a radial gradiometer with 5-cm baseline is plotted as a function of the source depth below the scalp. The result in Figure 6.27.a corresponds to a very short source

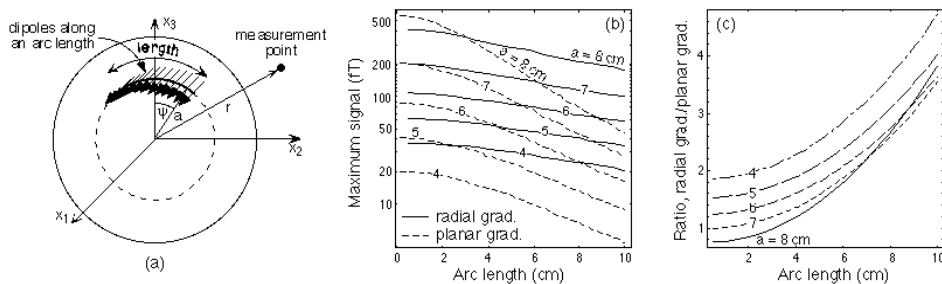


Figure 6.26. Difference between radial and planar gradiometers for linearly-extended sources as a function of source length. Radius of sensor shell  $r = 10.7$  cm, integrated dipole moment  $= 10$  nA·m,  $d_{rad} = 5$  cm,  $d_{plan} = 1.65$  cm. Source is a segment of an arc filled with a uniform density of dipoles perpendicular to the arc plane. (a) geometry of the calculation; (b) maximum signal as a function of the source length for dipole positions  $a = 4$  (deep) to  $8$  (shallow) cm. Solid lines - radial gradiometers, dashed lines - planar gradiometers; (c) ratio of radial to planar gradiometer maximum signal strength for  $a = 4$  to  $8$  cm.

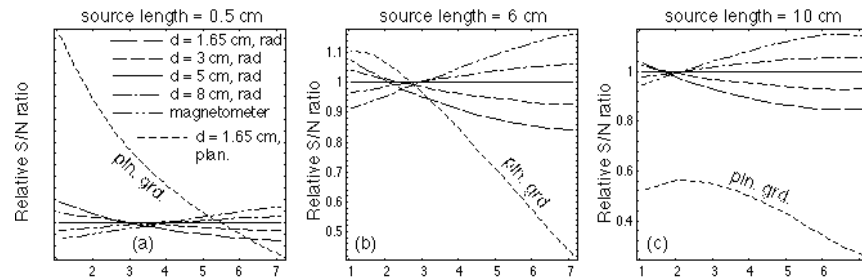


Figure 6.27. Relative S/N ratio for radial and planar gradiometers as a function of arc length and depth below the scalp for correlated noise. Radius of sensor shell  $r = 10.7$  cm,  $d_{\text{rad}} = 1.65, 3, 5, 8$  cm and magnetometer ( $d_{\text{plan}} = 1.65$  cm), all sensors are assumed to have "point" coils. The curves are normalized by radial gradiometer with baseline  $d_{\text{rad}} = 5$  cm for all depths. (a) short source with length of 0.5 cm, similar result as presented in [24]; (b) source length 6 cm; (c) source length 10 cm.

and is similar to that obtained for an equivalent current dipole in [24] or in Figure 6.24.c. However, as the source length increases, the advantage of the planar gradiometer decreases. For a source length of 6 cm and superficial sources, the planar gradiometer is comparable to the radial gradiometer, and for sources deeper than about 2.8 cm, the planar gradiometer becomes worse, Figure 6.27.b. For longer sources, the performance of radial gradiometers with any baseline is better than that of planar gradiometers for all source depths, Figure 6.27.c.

In summary: the signal strength detected by planar gradiometers is smaller than that of radial gradiometers or magnetometers (except for very superficial sources, where the planar gradiometer signal strength is larger). For situations where spontaneous brain signals are investigated and the noise is the random instrumental noise, the radial gradiometers give better results, and in situations where the evoked signals are studied and averaging is performed, the planar gradiometers give better results. For quadrupole sources, the exact configuration of the source determines whether planar or radial gradiometers are favored. For extended sources, the planar gradiometers are at a disadvantage, and even in the case of correlated noise, for extended sources the radial gradiometers give better results than the planar gradiometers.

## 6.5. CONCLUSIONS OF SENSOR DISCUSSION

It was assumed in this section that all sensor arrays have the same number of channels regardless of the sensor type. However, the sensor arrays may have different numbers of sensor sites, with multiple sensors at one site, e.g., a 150-channel system populated by radial gradiometers will have 150 sites, by planar gradiometers 75 sites, and by vector magnetometers 50 sites.

*Radial and vector magnetometers:* The radial magnetometers always give better results when random noise is considered. For correlated noise, radial and vector magnetometers are comparable when the sources are well within the sensor array, while vector magnetometers give better results when the sources are close to or outside the sensor array edge. Use of vector magnetometers (which also measure tangential field components) increases the sensitivity to volume currents and thus to the details of the model.

*Radial gradiometers (or magnetometers with remote reference):* Increasing the baseline increases the magnitude of the detected signal and also increases the sensitivity to environmental noise. As a result, there is an optimum baseline at which the S/N ratio is largest. Analysis of the noise measured at the existing shielded MEG sites shows that the optimum baseline is relatively short (1.5 to 10 cm). In addition, long baseline systems are more susceptible to vibrational noise.

*Radial and planar gradiometers:* The relative merits of the two sensor types depends on the detection situation. The radial gradiometers are favored for sources at all depths if random noise is considered, while planar gradiometers are favored if correlated noise and not very deep sources are considered. The advantage of planar gradiometers in the case of correlated noise quickly decreases or is completely eliminated if the sources are extended. Thus, if the sources are well localized, relatively superficial, and the background activity of the brain is of no interest, planar gradiometers give better results, while radial gradiometers give better results in all other cases, i.e., if the background activity of the brain is of interest, or if the sources are not well localized, or if the sources are deep. Similar conclusions are reached if instead of the dipole reconstruction accuracy the relative merits of planar and radial gradiometers are evaluated on the basis of angular resolution in the sensor space of two nearby sources in the presence of noise.

## 7. Miscellaneous system considerations

In this section, MEG system considerations not directly concerned with the SQUID magnetometer design will be discussed briefly: number of channels, head position location, co-registration with other modalities (e.g., MRI), EEG electrodes, patient handling, and stimulation equipment.

It was assumed in the previous discussions that there is a certain number of channels distributed around the head, but no criteria for channel spacing have been given (except in Section 6.1 where the sensor spacing limit was introduced for the sake of mathematical simplification of the dipole reconstruction expressions in the case of correlated noise). The number of channels can be determined from knowledge of the head area covered by the sensors, Figure 7.1, and the sensor spacing. One possible way to determine the sensor spacing is to require that it be compatible with the maximum signal spatial frequency for which the signal power spectrum is above the system noise [118, 119]. A

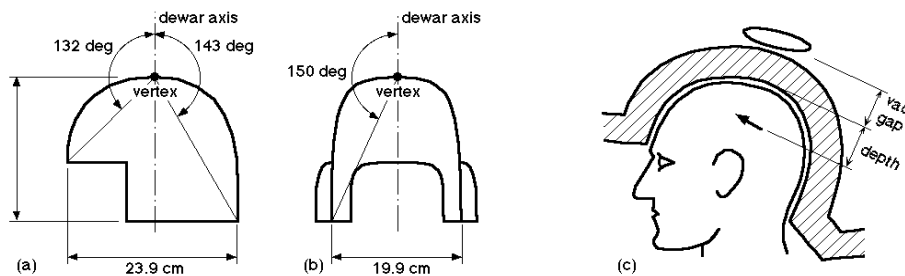


Figure 7.1. Determination of the inter-channel spacing. (a, b) example of head coverage for CTF MEG system, approximate surface area at the sensor level is 1160 cm<sup>2</sup>; (c) geometry for calculation of inter-channel spacing; sensor is separated from the head by vacuum gap of the dewar.

simple analysis of this problem for a current dipole source leads to a rule of thumb that the sensor spacing should be roughly equal to the source depth below the sensors when the power S/N ratio is less than about 30.

If the mean channel separation is  $e$ , then the area per sensor is  $e^2$  for sensors arranged in a square grid and  $(e^2 \sqrt{3})/2$  for a hexagonal grid. The source depth below the sensor shell consists of the vacuum gap in the dewar and the actual depth below the surface of the head, Figure 7.1.c. Using the above "rule of thumb," the channel spacing should be  $e = \text{gap} + \text{depth}$ , and the required numbers of channels,  $N$ , are shown in Table 7.1.

Table 7.1. Number of channels,  $N$ , for different source depths. Surface area of the sensor array at the sensor level is assumed to be  $1,160 \text{ cm}^2$ , vacuum gap = 1.5 cm.

depth (cm)	$e$ (cm)	$N$ (hexagonal lattice)
2	3.5	109
1.5	3	149
1	2.5	214

If, however, sources more complex than a single current dipole are used for estimation of the highest spatial frequency, or if different criteria are used (e.g., resolution of synthetic aperture magnetometry in Section 4.5), then the number of required channels will be larger than indicated in Table 7.1.

A photograph of a 143-channel sensor layout with mean sensor spacing of about 3.2 cm is shown in Figure 7.2. The primary sensors are hardware 1st-order radial gradiometers with 5-cm baseline, wound on the cylinders perpendicular to the structural shell.

Even though the subject's head is inserted in the dewar helmet, there is still some freedom to move it, and accurate measurement of the head position relative to the sensors is necessary. To accomplish this task, various 3D digitizing methods may be used [120], or the MEG system itself can be utilized for the head position determination. An example of such scheme is shown in Figure 7.3, where small coils are attached at specific anatomical locations on the head. The coils are activated by computer-controlled signal generators, their magnetic field is detected by the reference system and converted into positional information. Alternatively, the positional information also can be derived from the sensor signals.

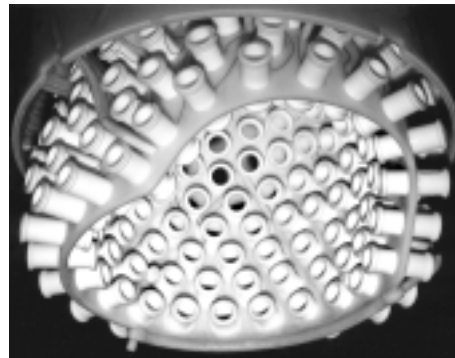


Figure 7.2. Photograph of 1st-order gradiometer sensors in the helmet area, 143 channels.

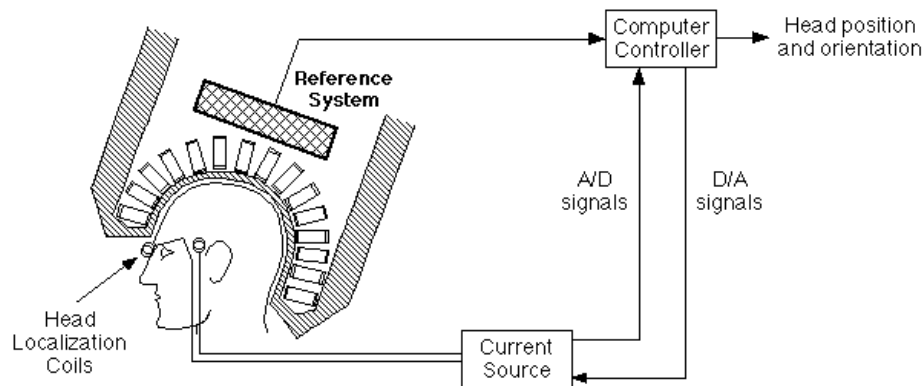


Figure 7.3. System for determination of head position used in CTF's MEG system. Small coils are placed at the nasion and preauricular points. Coils are energized by a computer-controlled current source, and signals are detected by the reference system and converted into coil positions.

The measuring procedure itself is probably the most accurate step in the determination of the head position. The actual repeatability of the positioning measurement determined using a static phantom was found to be about  $0.3 \pm 0.1$  mm in unshielded environments, and the absolute accuracy (given by the system calibration) is better than 2 mm. Larger errors are caused by inaccurate placement of the marker coils and by head motion during the measurement. It is estimated that the coils can be positioned on the head surface with accuracy of no better than about 2 to 3 mm, and the head motion is typically also of the order of 1 to 3 mm.

One goal of MEG is the localization of functional brain activity relative to anatomical structures obtained typically from MRI. Such localization requires the knowledge of a transformation matrix (rotation, scaling, translation) between the two modalities. There are different methods for determination of such transformations. The most common and simplest method uses a small number of anatomical marks that can be measured using both techniques (e.g., markers at the same locations as used for the MEG head position determination). This method is not too accurate because the placement errors of MEG and MRI markers are compounding. To reduce these problems, the partial- or whole-head surface is digitized in the MEG system of coordinates by a device mounted on the dewar, e.g., [120], or by magnetic sensors themselves, as in Figure 7.3 (using a method similar to that for measuring the EEG electrode positions - see below). In the MRI system of coordinates, the surface of the head is reconstructed from the MRI information. The transformation between the two systems is then determined by minimizing the difference between the two surfaces [121-123].

When EEG is used simultaneously with MEG, care must be taken to select electrodes with a low-level magnetic signature. The electrode positions can be determined either by a 3D digitizer, or magnetically as in Figure 7.3. In this case, 3 marker coils are placed at the anatomical landmarks, the head is withdrawn from the helmet such that its surface can be comfortably reached by hand, and a 4th energized coil is used to touch the electrodes and determine their positions in the MEG frame of reference. The currents in the EEG electrode wires due to EEG potentials usually do not interfere with magnetic measurements. Consider that the EEG electrode wires form a loop with radius  $r$ . The

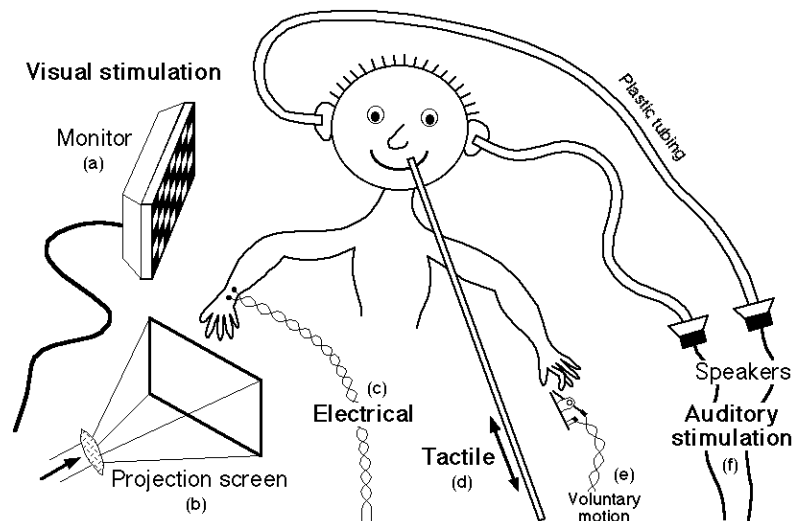


Figure 7.4. Schematic diagram of various stimulation methods. (a, b) visual stimulators; (c) electrical stimulator; (d) mechanical tactile stimulator; (e) switch for subject's response, e.g. voluntary motion; (f) auditory stimulation.

magnetic field at the center of the loop is  $B = \mu_0 I / (2r)$ , where  $I$  is the current in the loop. If it is required that  $B < 5$  fT, and if  $r = 5$  cm, then the current in the loop should satisfy  $I < 0.4$  nA. If the corresponding EEG voltage was assumed to be about  $200 \mu\text{V}$ , then the EEG amplifier impedance should be  $> 0.5$  M $\Omega$ . The EEG amplifiers usually satisfy this criterion, and the currents caused by the EEG signals are negligible from the MEG point of view.

Before the MEG measurement, the subject must be properly prepared. All potentially magnetic articles must be removed (correction glasses, various metal clips, zippers, buttons, watches, etc.) and the patient should be checked for magnetic contamination (dental braces, contaminated hair, etc.). Such precautions may be relaxed if effective noise cancellation is employed (e.g., synthetic aperture magnetometry, Section 4.5, allows a successful MEG measurement even when subjects with dental braces are asked to speak aloud). Where applicable, stimulus equipment is attached to the subject, and the subject is measured either in a seated or a reclining position, and in some cases, the head is fixed in the helmet by additional padding or inflatable bladders. All equipment and components near the sensitive end of the MEG system must have a sufficiently low-level magnetic signature in order to avoid magnetic noise and/or artifact generation.

MEG experiments are carried out with a wide range of stimulation equipment, Figure 7.4 (e.g., visual stimulation using projection screens and/or computer monitors, electrical stimulation, tactile stimulation, auditory stimulation, various switches for detection of subject's response, etc.). The wires of the electrical stimulators should be tightly twisted when they are close to the helmet region. The computer monitors, if used, must be tested for magnetic noise and synchronous artifacts - some monitors could be as close as 1.5 m from the magnetic sensors if 3rd-order gradiometer noise cancellation is used. All other magnetic components (speakers, switches, etc.) must be located sufficiently far from the sensitive end of the MEG system.

## 8. Examples of MEG applications

The discussion of MEG systems will be concluded by a few examples of the end results of the measurements. First two examples illustrate the use of MEG for pre-surgical mapping. Pre-surgical mapping is used to determine important centers in the brain, which in its diseased state may be distorted and may be difficult to recognize by a surgeon. The first example in Figure 8.1 is of Auditory Evoked Fields (AEF), where the subject is stimulated by sound to either one or both ears, as in Figure 7.4.f. The time traces of AEF signals were already shown in Figure 4.22.b, and the two dipoles overlaid on an MRI image are shown for a healthy brain in Figure 8.1.a [124]. The dipoles are located in the Sylvian fissure. The round dot indicates the estimated dipole position, and the short line, its orientation. In Figure 8.1.b [16] the AEF in a patient with glioma is shown. The closeness of the auditory cortex to the tumor suggested that only a limited resection should be done in order to preserve a possible language area behind the primary auditory cortex. One month after the surgery the verbal IQ returned to within a normal range.

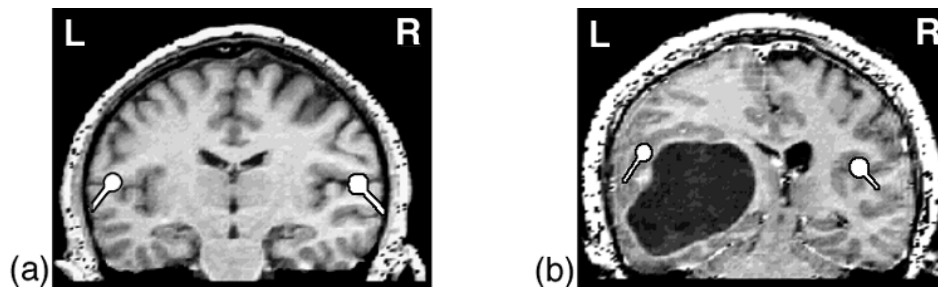


Figure 8.1. Auditory Evoked Fields. (a) normal male subject, estimated dipole positions for contra-lateral ear stimuli; (b) patient with glioma, N100 dipole indicated primary auditory cortex adjacent to the tumor. Adapted from references [16 and 124].

The second pre-surgical mapping example corresponds to Somatosensory Evoked Fields (SEF). A field map due to median nerve stimulation SEF (Figure 7.3.c) of a healthy subject was already shown in Figure 2.5.c. The pre- and post-operative locations of the SEF sources in the case of right frontal meningioma are shown in Figure 8.2 [124].

Temporal-lobe epilepsy recording in an unshielded environment [81] is shown in Figure 8.3. Even though the measurement was unshielded, the baseline drift was less than 0.6 pT (with 0.7 pT standard deviation over all channels) over a 540-sec period. In Figure 8.3 only a short data segment in the vicinity of an epileptic interictal spike is shown. In addition to the spikes, the frontal channels also exhibit high amplitude slow variations, while these variations are absent in the central channels.

The last example shows the application of MEG to functional neuroimaging mapping of the cortical response to language stimuli, either reading a story containing meaningful and nonsense words or object-naming tasks [125]. A region of focal suppression was observed in the left frontal cortex, slightly superior to Broca's area.

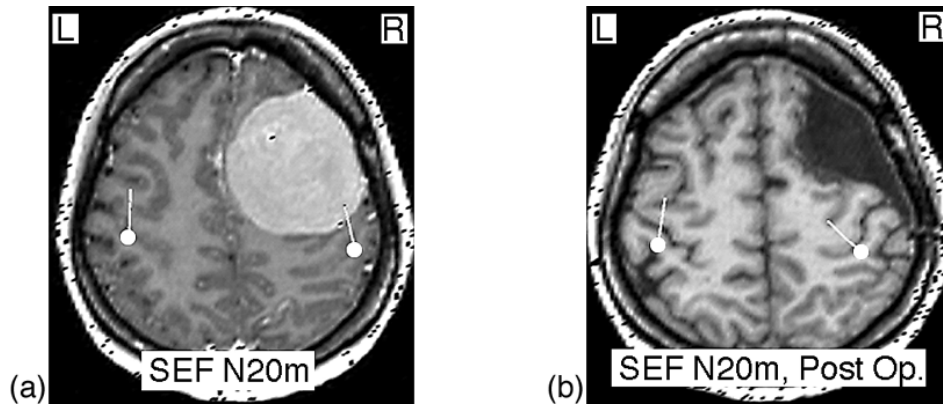


Figure 8.2. Median nerve stimulated Somatosensory Evoked Fields in the case of right frontal meningioma. (a) pre-operative SEF indicates shifted right central sulcus due to tumor mass effect; (b) post-operative SEF indicates normalized right central sulcus. Adapted from reference [124].

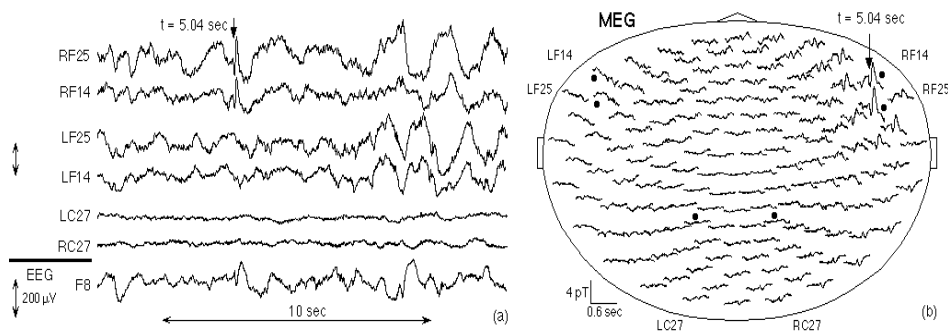
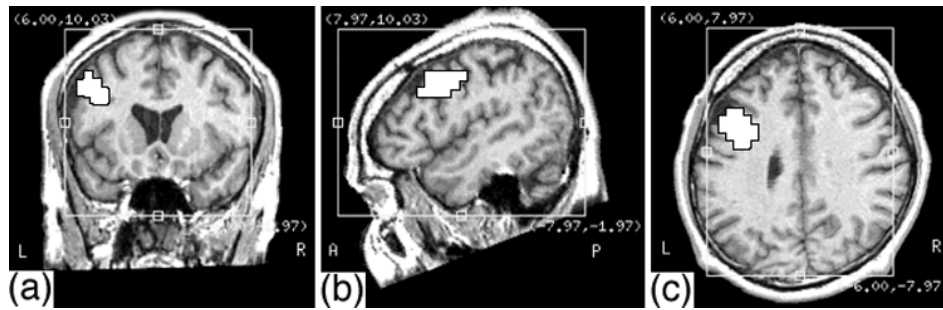


Figure 8.3. Temporal lobe epilepsy, complex partial seizures. (a) time traces of two of each left frontal, right frontal and central MEG channels and F8 EEG channel. An interictal spike is shown by an arrow; (b) traces for all channels, dots indicate time traces in (a) and arrow indicates the interictal spike. Adapted from [81].

## 9. Conclusions

The most successful application of biomagnetometers is presently MEG. Therefore, MEG systems were used as a model for discussion of biomagnetometer characteristics. MEG systems have evolved into sophisticated multichannel devices with good sensitivity to magnetic fields, even while they are exposed to considerable environmental noise. The presence of noise imposes certain specifications on the system's dynamic range, slew rate, linearity and matching between channels. It also stimulates development of special noise cancellation methods.

Noise in biomagnetic systems is handled by a variety of methods: shielding, active noise cancellation, synthetic noise cancellation and various spatial filtering methods. The shielding and active noise cancellation reduce the environmental noise magnitudes, and relax specifications on the biomagnetometer electronics. However, regardless of the



*Figure 8.4.* Differential current density map of a cortical response to language stimuli of a typical subject overlaid on the MRI. Three orthogonal views for a single run in 15- to 30-Hz frequency band. Region of focal suppression of source activity (white areas) appears in the left lateral frontal cortex. The peak intensity of the suppression is 6.4 nA·m, and the area shown has been thresholded at half amplitude. Adapted from [125].

shielding method used, residual noise always is present and must be eliminated by some noise cancellation method (perhaps with the exception of the whole-body superconducting shield with very low residual magnetic fields, Section 4.2).

Synthetic noise cancellation assumes the existence of reference channels in addition to the sensor channels. The reference channels are placed at some distance from the measured tissue, and they mostly detect environmental noise. The references and sensors are combined synthetically to eliminate noise from the sensing channels. The coefficients of this synthetic system can be determined to represent either higher-order gradiometers, or simply correspond to an adaptive process. There is a clear distinction between the two types of noise cancellation. Gradiometers of order  $n$  are designed to cancel field and all gradients of orders up to  $n-1$ , and are sensitive to the gradient of order  $n$  (and also affected by higher gradients). On the other hand, adaptive systems minimize the outputs for all gradient orders. Adaptive systems of order  $n$  may not completely cancel all gradients of orders less than  $n$ , but this incomplete cancellation of lower-order gradients is compensated by additional partial cancellation of gradiometers of order  $n$  and higher. Adaptive systems perform better than gradiometer systems during the time period for which the noise character remains constant. However, their performance quickly deteriorates when the noise character changes. In practice, it was found that the time period during which noise remains constant can be as short as several seconds.

Gradiometer systems are characterized by universal or "fixed" coefficients, i.e., the coefficients are independent of the noise character and, therefore, of the time of the day, system orientation or location. On the other hand, the adaptive coefficients are not universal and cannot be transported to different environments.

For all practical measurement situations, the output of both gradiometer and adaptive systems is proportional to their dimension or baseline. In a simple 1st-order system the baseline is the distance between the sensing coil and the reference system.

The sensor space filtering methods rely on the observation that different signal or noise sources are represented by vectors pointing in different directions in a multidimensional space, where the number of dimensions is equal to the number of channels. The noise cancellation further assumes that the noise and signal vectors are not collinear and that they can be separated. These methods can provide cancellation of far-field environmental noise as well as noise from physically near sources (e.g., the activity in one part

of the brain can be separated from the activity in other parts of the brain, or heart signals can be separated from brain signals, etc.). Simultaneous use of the sensor space filtering and synthetic noise cancellation methods can be beneficial; the synthetic noise cancellation can be used to remove the noise and reduce the data dynamic range before the sensor space filtering methods are applied.

Sensing coils, or flux transformers, are exposed to the measured fields and noise, and their configuration determines the characteristics of the biomagnetometer system. Several flux-transformer types were examined and compared using the equivalent current dipole reconstruction accuracy as a measure of the flux-transformer performance:

*Magnetometers:* Radial and vector magnetometers were compared. It was shown that, generally, radial magnetometers are a better choice than vector magnetometers. Radial magnetometers always give better results when random noise is considered. For correlated noise, the radial and vector magnetometers are equivalent when the sources are well within the sensor array, and the vector magnetometers are better when the sources are close to or outside the sensor array edge. However, if the vector magnetometers were used, their tangential components would introduce greater sensitivity to volume currents, and through it, to the details of the model.

*Radial gradiometers (hardware or synthetic):* The dependence of S/N ratio on the baseline was examined. It was concluded that the best S/N ratio exists for a certain optimum baseline length, given by an interplay between the detected signal strength and the sensitivity to environmental noise. The conditions for the optimum baseline were calculated and investigated experimentally. At all experimentally investigated MEG sites, the optimum baseline was found to be quite short (about 1.5 to 10 cm). In comparison with magnetometers, gradiometers with near optimum baseline are a better choice.

*Planar gradiometers:* The relative merit of radial and planar gradiometers depends on the type of measurement performed. If general brain activity is of interest, or if the sources are not well localized (i.e., are extended) or the sources are deep, radial gradiometers perform better. On the other hand, if general brain activity is of no interest, or if the sources are known to be well localized, or are shallow, planar gradiometers perform better.

In addition to the optimization of the sensing-coil configurations and the SQUID electronics, biomagnetometers also contain other important elements, e.g., head positioning system, EEG electrodes, patient support system, miscellaneous stimulation equipment, etc. For successful and low-noise operation of biomagnetometers, all peripheral equipment must be magnetically clean and must be harmoniously integrated with the SQUID detectors.

## Acknowledgment

I would like to express my gratitude to Drs. D. Cheyne and A.A. Fife for reviewing the manuscript and for their constructive comments. I would like to thank my colleagues at CTF Systems Inc., K. Betts, J. Box, M.B. Burbank, T. Cheung, D. Cheyne, A. A. Fife, S. Govorkov, G. Haid, V. Haid, C. Hunter, P.R. Kubik, S. Lee, W. Ludwig, J. McCubbin, J. McKay, D. McKenzie, D. Nonis, E. Reichl, S. Robinson, C. Schroyen, P. Spear, B. Taylor, M. Tillotson and S. White for their enthusiastic support, help with experiments, analysis and simulations; Dr. W. Ludwig for suggesting to investigate de-

tection of quadrupoles; Dr. H. Weinberg and Dr. D. Cheyne for guidance and help with human experiments; Dr. H. Wilson, EDRD, Victoria, B.C. for help and discussion regarding conventional magnetometers; Dr. D. Cheyne of CTF and Dr. N. Nakasato of Kohnan Hospital, Sendai, Japan for suggesting several figures in Section 2; and Dr. K.C. Squires, Mr. G. Haid, and Dr. A. Ahonen for providing Figures 3.5 to 3.7.

## References

- [1]Waller, A.D. (1887) A demonstration on man of electromotive changes accompanying the heart's beat, *J. Physiol.* **8**, 229-234.
- [2]Einthoven, W. (1903) Ein neues Galvanometer, *Ann. Phys.* **12** (4), 1059-1071; Einthoven, W. (1908) Weiteres uber das Elektrokardiogramm, *Pfluegers Arch.* **122**, 517-584.
- [3]Baule, G.M. and McFee, R. (1963) Detection of the magnetic field of the heart, *Am. Heart. J.* **66**, 95-96.
- [4]Berger, H. (1929) Uber das Electrenkephalogramm des Menschen, *Arch. Psychiat. Nervenkr.* **7**, 527-570.
- [5]Cohen, D. (1968) Magnetoencephalography: evidence of magnetic fields produced by alpha-rhythm current, *Science* **161**, 784-786.
- [6]Josephson, B.D. (1962) Possible new effects in superconductive tunneling, *Phys. Lett.* **1**, 251-253.
- [7]Jaklevic, R., Lambe, R.C., Silver, A.H., and Mercereau, J.E. (1964) Quantum interference effects in Josephson tunneling, *Phys. Rev. Lett.* **12**, 159-160.
- [8]Zimmerman, J.E. and Silver, A.H. (1964) Quantum effects in type II superconductors, *Phys. Lett.* **10**, 47-48.
- [9]Silver, A.H. and Zimmerman, J.E. (1967) Quantum states and transitions in weakly connected superconducting rings, *Phys. Rev.* **157**, 317-341.
- [10]Zimmerman, J.E., Thiene, P., and Harding, J.T. (1970) Design and operation of stable rf-biased superconducting point-contact quantum devices, and a note on the properties of perfectly clean metal contacts, *J. Appl. Phys.* **41**, 1572-1580.
- [11]Mercereau, J.E. (1970) Superconducting magnetometers, *Rev. Phys. Appl.* **5**, 13-20.
- [12]Cohen, D., Edelsack, E.A. and Zimmerman, J.E. (1970) Magnetocardiograms taken inside a shielded room with a superconducting point-contact magnetometer, *Appl. Phys. Lett.* **16**, 278-280.
- [13]Cohen, D. (1972) Magnetoencephalography: Detection of the brain's electrical activity with a superconducting magnetometer, *Science* **175**, 664-666.
- [14]Nakaya, Y. and Mori, H. (1992) Magnetocardiography, *Clin. Phys. Physiol. Meas.* **13**, 191-229.
- [15]Wiskwo, J.P.Jr. (1995) SQUID Magnetometers for Biomagnetism and Nondestructive Testing: Important Questions and Initial Answers, *IEEE Trans. Appl. Supercond.* **5**, 74-120.
- [16]Nakasato, N., Seki, K., Kawamura, T., Ohtomo, S., Kanno, A., Fujita, S., Hatanaka, K., Fujiwara, S., Kayama, T., Takahashi, A., Jokura, H., Kumabe, T., Ikeda, H., Mizoi, K. and Yoshimoto, T. (1996) Cortical Mapping Using an MRI-Linked Whole Head MEG System and Presurgical Decision Making, *Electroencephalogr. Clin. Neurophysiol. Suppl.* **47**, 333-341.
- [17]Nakasato, N., Levesque, M.F., Barth, D.S., Baumgartner, C., Rogers, R.L. and Sutherling, W.W. (1994) Comparisons of MEG, EEG, and ECoG source localization in neocortical partial epilepsy in humans, *Electroencephalogr. Clin. Neurophysiol.* **171**, 171-176.
- [18]Vieth, J. B., Kober, H., Stippich, C., Kassubek, J.R., and Hopfengaertner, R. (1997) Time Course of Abnormal MEG Activity Associated with Transient Ischemic Attack, in C. Aine et al (eds.), *Biomag96: Advances in Biomagnetism Research*, Springer-Verlag, in press.
- [19]Vieth, J., Kober, H., Grummich, P., Pongratz, H., Ulbricht, D., Brigel, C., and Daun, A. (1995) Slow wave and beta wave activity associated with white matter structural brain lesions, localized by the dipole density plot, in C. Baumgartner et al (eds.), *Biomagnetism: Fundamental Research and Clinical Applications*, Elsevier Science, IOS Press, pp.50-54.
- [20]Lewine, J.D., Davis, L.E., Hart, B.L., Davis, J.T., Orrison, W.W.Jr. (1997) Neuromagnetic Evaluation of Ischemic Lesions, in C. Aine et al (eds.), *Biomag96: Advances in Biomagnetism Research*, Springer-Verlag, in press.
- [21]Lewine, J.D., Orrison, W.W.Jr., Astur, R.S., Davis, L.E., Knight, J.E., Maclin, E.L., and Reeve, A. (1995) Explorations of pathophysiological spontaneous activity by magnetic source imaging, in C. Baumgartner et al (eds.), *Biomagnetism: Fundamental Research and Clinical Applications*, Elsevier Science, IOS Press, pp.55-59.
- [22]Cheyne, D., Vrba, J., Crisp, D., Betts, K., Burbank, M., Cheung, T., Fife, A.A., Haid, G., Kubik, P., Lee, S., McCubbin, J., McKay, J., McKenzie, D., Spear, P., Taylor, B., Tillotson, M., Weinberg, H., Basar, E., and Tsutada, T. (1992) Use of an unshielded, 64-channel whole-cortex MEG system in the study of normal and pathological brain function. *Proc. Satellite Symposium on Neuroscience and Technology*, Proc. IEEE-EMBS, Lyon, France.

- [23] Vrba, J., Betts, K., Burbank, M.B., Cheung, T., Fife, A.A., Haid, G., Kubik, P.R., Lee, S., McCubbin, J., McKay, J., McKenzie, D., Spear, P., Taylor, B., Tillotson, M., Cheyne, D., and Weinberg, H. (1993) Whole Cortex, 64 Channel SQUID Biomagnetic System, *IEEE Trans. Appl. Supercond.* **3**, 1878-1882.
- [24] Knuutila, K.E.T., Ahonen, A.I., Hamalainen, M.S., Kajola, M.J., Laine, P.P., Lounasmaa, O.V., Parkkonen, L.T., Simola, J.T.A., and Tesche, C.D. (1993) A 122-channel whole-cortex SQUID system for measuring the brain's magnetic fields, *IEEE Trans. Mag.* **29**, 3315-3320.
- [25] Biomagnetic Technologies, Inc. 9727 Pacific Heights Blvd., San Diego, CA 92121-3719, USA.
- [26] CTF Systems Inc., 15-1750 McLean Ave, Port Coquitlam, B.C., Canada, V3C 1M9.
- [27] Neuromag Ltd., Elimaenkatu 22 A, P.O. Box 68, FIN-00511 Helsinki, Finland.
- [28] Pflieger, M.E., Simpson, G.V., Ahlfors, S.P. and Ilmoniemi, R.J. (1997) Superadditive Information from Simultaneous MEG/EEG data, in C. Aine et al (eds.), *Biomag96: Advances in Biomagnetism Research*, Springer-Verlag, in press.
- [29] Cohen, D. and Cuffin, B.N. (1987) A method of combining MEG and EEG to determine the sources, *Phys. Med. Biol.* **32**, 85-89.
- [30] ter Brake, H.J. M., Flokstra, J., Jaszczuk, W., Stammers, R., van Ancum, G.K., and Martinez, A. (1991) The UT 19-channel dcSQUID based neuromagnetometer, *Clin. Phys. Physiol. Meas.* **12B**, 45-50.
- [31] Becker, W., Dickmann, V., Jurgens, R. and Kornhuber, C. (1993) First experiences with a multichannel software gradiometer recording normal and tangential components of MEG, *Physiol. Meas.* **14**, A45-A50.
- [32] Dieckmann, V., Jurgens R., Becker, W., Elias, H., Ludwig, W. and Vodel, W. (1996) RF-SQUID to DC-SQUID Upgrade of a 28-Channel Magnetoencephalography (MEG) System, *Meas. Sci. Technol.* **7**, 844-852.
- [33] Matlashov, A.N., Slobodchikov, V.Y., Bakharev, A.A., Zhuravlev, Yu., and Bondarenko, N. (1995) Biomagnetic Multichannel system built with 19 cryogenic probes, in C. Baumgartner et al (eds.), *Biomagnetism: Fundamental Research and Clinical Applications*, Elsevier Science, IOS Press, pp.493-496.
- [34] Drung, D., Absmann, Curio, G., Mackert, B.-M., Matthies, K.-P., Matz, H., Peters, M., Scheer, H.-J. and Koch, H. (1995) The PTB 83-SQUID System for Biomagnetic Applications in a Clinic, *IEEE Trans. Appl. Supercond.* **5**, 2112-2117.
- [35] Dossel, O., David, B., Fuchs, M. Kruger, J., Ludeke, K.-M., and Wischmann, H.-A. (1993) A 31-channel SQUID system for biomagnetic imaging, *Appl. Supercond.* **3**, 1813-1825.
- [36] Yoshida, Y., Arakawa, A., Kondo, Y., Kajihara, S., Tomita, S., Tomita, T., Matsuda, N., and Takanashi, Y. (1997) A 129 Channel Vector Neuromagnetic Imaging System, in C. Aine et al (eds.), *Biomag96: Advances in Biomagnetism Research*, Springer-Verlag, in press.
- [37] Ueda, M., Kandori, A., Ogata, H., Takada, Y., Komuro, T., Kazami, K., Ito, T. and Kado, H. (1995) Development of a biomagnetic measurement system for brain research, *IEEE Trans. Appl. Supercond.* **5**, 2465-2469.
- [38] Sata, K., Fujimoto, S., Fukui, N., Haraguchi, E., Kido, T., Nishiguchi, N., and Kang, Y.M. (1997) Development of a 61-Channel MEG System Cooled by a GM/JT Cryocooler, in C. Aine et al (eds.), *Biomag96: Advances in Biomagnetism Research*, Springer-Verlag, in press.
- [39] Fujimoto, S., Sata, K., Fukui, N., Haraguchi, E., Kido, T., Nishiguchi, K., and Kang, Y.M. (1997) A 32-channel MCG System Cooled by a GM/JT Cryocooler, in C. Aine et al (eds.), *Biomag96: Advances in Biomagnetism Research*, Springer-Verlag, in press.
- [40] Itozaki, H., Kugai, H., Nagaishi, T., Toyoda, H., Hirano, T., Haruta, Y., Tanaka, S., and Kado, H. (1997) 32 Channel High Tc SQUID System for Biomagnetism, in C. Aine et al (eds.), *Biomag96: Advances in Biomagnetism Research*, Springer-Verlag, in press.
- [41] Talairach, J. and Tournoux, P. (1988) *Co-Planar Stereotactic Atlas of the Human Brain*, G. Thieme Medical Publishers, Stuttgart, New York. Or an electronic version CD-rom, digitized number of paper brain atlases published by Thieme-Verlag: Talairach, J. and Tournoux, P. (1988) *Co-Planar Stereotactic Atlas of the Human Brain*; Schaltenbrand, G., Hassler, R., and Wahren, W. (1977) *Atlas of Stereotaxy of the Human Brain*; selected patterns from Ono M., Kubik M.D., and Abernathy C.D. (1990) *Atlas of the Cerebral Sulci*. CieMed, Center for Information-enhanced Medicine, jointly set up in 1994 by Johns Hopkins University and the Institute of Systems Science of the National University of Singapore, Heng Mui Keng Terrace, Kent Ridge, 0511, Singapore 119597, Republic of Singapore, [http://ciemed.iss.nus.sg/research/brain/brain\\_cd.html](http://ciemed.iss.nus.sg/research/brain/brain_cd.html).
- [42] Hiriyannaiah, H.P. (1997) X-ray Computed Tomography for Medical Imaging, *IEEE Signal Processing* **14**, No.2, 42-59.
- [43] Wright, G.A. (1997) Magnetic Resonance Imaging, *IEEE Signal Processing* **14**, No.1, 56 - 66.
- [44] Deans, S.R. and Roderick, S. (1983) *The Radon Transform and some of its applications*, Wiley, New York.
- [45] Smith, S.L. (1985) Magnetic Resonance Imaging, *Anal. Chem.* **57**, A595-A607.
- [46] Kumar, A., Welti, D., and Ernst, R.R. (1975), NMR Fourier Zeugmatography, *J. Magn. Reson.* **18**, 69-83.
- [47] Lauterbur, P.G. (1973), Image Formation by Induced Local Interactions: Examples Employing Nuclear Magnetic Resonance, *Nature* **242**, 190-191.
- [48] Ollinger, J.M. and Fessler, J.A. (1997) Positron-Emission Tomography, *IEEE Signal Processing* **14**, No.1, 43-55.

- [49] Gilardi, M.C., Rizzo, G., Lucignani, G., and Fazio, F. (1996) Integrating Competing Technologies with MEG, in H. Weinstock (ed.), *SQUID Sensors: Fundamentals, Fabrication and Applications*, NATO ASI Series E: Applied Sciences, Vol. 329, Kluwer Academic Publishers, Dordrecht, pp.491-516.
- [50] Leichner, P.K., Morgan, H.T., Holdeman, K.P., Valentino, F., Lexa, R., Kelly, R.F., Hawkins, W.G. and Dalrymple, G.V. (1995) SPECT imaging of Fluorine-18, *J. Nucl. Med.* **36**, 1472-1475.
- [51] Forzaneh, F., Riederer, S.J., and Pelc, N.J. (1990) Analysis of T2 Limitations and Off-Resonance Effects on Spatial Resolution and Artifacts in Echo-Planar Imaging, *Magn. Reson. Med.* **14**, 123-139.
- [52] Bruder, H., Fischer, H., Reinfelder, H.E., and Schmitt, F. (1992) Image Reconstruction for Echo Planar Imaging with Nonequidistant k-Space Sampling, *Magn. Reson. Med.* **23**, 311-323.
- [53] Bandettini, P.A., Jesmanowicz, A., Wong, E.C., and Hyde, J.S. (1993) Processing Strategies for Time-Course Data Sets in Functional MRI of the Human Brain, *Magn. Reson. Med.* **30**, 161-173.
- [54] George, J.S., Schmidt, D.M., Mosher, J.C., Aine, C.J., Ranken, D.M., Wood, C.C., Lewine, J.D., Sanders, J.A., and Belliveau, J.W. (1997) Dynamic Neuroimaging by MEG, Constrained by MRI and fMRI, in C. Aine et al (eds.), *Biomag96: Advances in Biomagnetism Research*, Springer-Verlag, in press.
- [55] Ioannides, A.A., Taylor, J.G., and Muller-Gartner, H.W. (1997) MFT based investigation of MEG congruence with fMRI, in C. Aine et al (eds.), *Biomag96: Advances in Biomagnetism Research*, Springer-Verlag, in press.
- [56] Partridge, L.D. and Partridge, L.D. (1993) *The Nervous System, Its Function and Its Interaction with the World*, A Bradford Book, The MIT Press, Cambridge, Massachusetts.
- [57] Wikswo, J.P.Jr. (1989) Biomagnetic Sources and their Models, in S.J. Williamson et al (eds.), *Advances in Biomagnetism*, Plenum Press, New York and London, pp.1-18.
- [58] Taccardi, B. (1982) Electrophysiology of excitable cells and tissues, with special consideration of the heart muscle, in S.J. Williamson, G.L. Romani, L.Kaufman, and I.Modena (eds.), *NATO ASI Biomagnetism, An Interdisciplinary Approach*, Series A: Life sciences, Vol.66, Plenum Press, New York and London, pp.141-171.
- [59] Carpenter M.B. (1985) *Core Text of Neuroanatomy*, Williams & Wilkins, Baltimore, London, Sydney.
- [60] Okada, Y.C., Papuashvili, N., and Xu, C. (1997) Maximum current dipole moment density as an important physiological constraint in MEG inverse solutions, in C. Aine et al (eds.), *Biomag96: Advances in Biomagnetism Research*, Springer-Verlag, in press.
- [61] Nakasato, N., Fujita, S., Seki, K., Kawamura, T., Matani, A., Tamura, I., Fujiwara, S., and Yoshimoto, T. (1995) Functional localization of bilateral auditory cortices using an MRI-linked whole head magnetoencephalography (MEG) system, *Electroencephalogr. Clin. Neurophysiol.* **94**, 183-190.
- [62] Grynszpan F. and Geselowitz, D.B. (1973) Model studies of the magnetocardiogram, *Biophysical Journal* **13**, 911-925.
- [63] Sarvas, J. (1987) Basic Mathematical and Electromagnetic Concepts of the Biomagnetic Inverse Problem, *Phys. Med. Biol.* **32**, 11-22.
- [64] Williamson, S.J. and Kaufman, L. (1981) Biomagnetism, *J. Mag. Mag. Materials* **22**, 129-201.
- [65] Williamson, S.J. and Kaufman, L. (1981) Biomagnetic Fields of the Cerebral Cortex, in S.N. Erne et al (eds.), *Biomagnetism*, Walter de Gruyter, Berlin and New York, pp.353-402.
- [66] Cheyne, D., Roberts, L.E., Gaetz, W., Bosnyak, D., Weinberg, H., Johnson, B., Nahmias, C., and Deecke, L. (1997) EEG and MEG Source Analysis of Somatosensory Evoked Responses to Mechanical Stimulation, in C. Aine et al (eds.), *Biomag96: Advances in Biomagnetism Research*, Springer-Verlag, in press.
- [67] Clarke, J. (1993) SQUIDS: theory and practice, in H. Weinstock and R.W. Ralston (eds.), *The New Superconducting Electronics*, Kluwer Academic Publishers, Dordrecht, pp.123-180.
- [68] Clarke, J. (1996) SQUID Fundamentals, in H. Weinstock (ed.), *SQUID Sensors: Fundamentals, Fabrication and Applications*, NATO ASI Series E: Applied Sciences, Vol. 329, Kluwer Academic Publishers, Dordrecht, pp.1-62.
- [69] Braginski, A.I. (1996) Fabrication of high-temperature SQUID magnetometers, in H. Weinstock (ed.), *SQUID Sensors: Fundamentals, Fabrication and Applications*, NATO ASI Series E: Applied Sciences, Vol. 329, Kluwer Academic Publishers, Dordrecht, pp.235-288.
- [70] Vrba, J. (1996) SQUID gradiometers in real environments, in H. Weinstock (ed.), *SQUID Sensors: Fundamentals, Fabrication and Applications*, NATO ASI Series E: Applied Sciences, Vol. 329, Kluwer Academic Publishers, Dordrecht, pp.117-178.
- [71] McKay, J., Vrba, J., Betts, K., Burbank, M.B., Lee, S., Mori, K., Nonis, D., Spear, P., and Uriel, Y. (1993) Implementation of a Multi-Channel Biomagnetic Measurement System Using DSP Technology, *Proceedings of 1993 Canadian Conference on Electrical and Computer Engineering*, vol. II, pp.1090-1093.
- [72] Ripka, P. (1992) Review of fluxgate sensors, *Sensors and Actuators*, **A33**, 129-141.
- [73] Nielsen, O.V., Petersen, J.R., Primdahl, F., Brauer, P., Hernandot, B., Fernandez, A., Merayo, J.M.G., and Ripka, P. (1995) Development, construction and analysis of the "Oersted" fluxgate magnetometer, *Meas. Sci. Technol.* **6**, 1099-1115.
- [74] Le Garrec, A., Leger, J.M., Pureur, D., Douay, M., Bernage, P., Niay, P., and Delevaque, E. (1994) A tunable fiber laser for application to helium optically pumped magnetometer, *Journal de Physique IV*, **4**, C4:695-698.

- [75] Carelli, P., Modena, I., and Romani, G.L. (1982) Detection coils, in S.J. Williamson, G.L. Romani, L. Kaufman, and I. Modena (eds.), *NATO ASI Biomagnetism, An Interdisciplinary Approach*, Series A: Life sciences, Vol.66, Plenum Press, New York and London, pp.85-95.
- [76] Katila, T. (1989) Principles and applications of SQUID sensors, in S.J. Williamson et al (eds.), *Advances in Biomagnetism*, Plenum Press, New York and London, pp.19-32.
- [77] Katila, T. (1981) Instrumentation for biomedical applications," in *Biomagnetism*, Proceedings of the Third International Workshop on Biomagnetism, in S.N. Erne et al (eds.), *Biomagnetism*, Walter de Gruyter, Berlin and New York, pp.3-31.
- [78] Kelha, V.O. (1981) Construction and performance of the Otaniemi magnetically shielded room, in S.N. Erne et al (eds.), *Biomagnetism*, Walter de Gruyter, Berlin and New York, pp.33-50.
- [79] Sullivan, G.W. and Flynn, E.R. (1987) Performance of the Los Alamos shielded room, in K. Atsumi et al (eds.), *Biomagnetism'87*, Tokyo Denki University Press, Tokyo, pp.486-489.
- [80] Vrba, J., Betts, K., Burbank, M., Cheung, T., Cheyne, D., Fife, A.A., Haid, G., Kubik, P.R., Lee, S., McCubbin, J., McKay, J., McKenzie, D., Mori, K., Spear, P., Taylor, B., Tillotson, M., and Xu, G. (1995) Whole cortex 64 channel system for shielded and unshielded environments, in C. Baumgartner et al (eds.), *Biomagnetism: Fundamental Research and Clinical Applications*, Elsevier Science, IOS Press, pp.521-525.
- [81] Vrba, J., Angus, V., Betts, K., Burbank, M.B., Cheung, T., Fife, A.A., Haid, G., Kubik, P.R., Lee, S., Ludwig, W., McCubbin, J., McKay, J., McKenzie, D., Robinson, S.E., Smith, M., Spear, P., Taylor, B., Tillotson, M., Cheyne, D., and Weinberg, H. (1997) 143 channel whole-cortex MEG system, in C. Aine et al (eds.), *Biomag96: Advances in Biomagnetism Research*, Springer-Verlag, in press.
- [82] Knuutila, J. and Hamalainen, M. (1987) Characterisation of brain noise using a high sensitivity 7-channel magnetometer, in K. Atsumi et al (eds.), *Biomagnetism'87*, Tokyo Denki University Press, Tokyo, pp.186-189.
- [83] Huotilainen, M., Ilmoniemi, R.J., Tiitinen, H. Lavikainen, J., Alho, K., Kajola, M., and Naatanen, R. (1995) The projection method in removing eye-blink artefacts from multichannel MEG measurements, in C. Baumgartner et al (eds.), *Biomagnetism: Fundamental Research and Clinical Applications*, Elsevier Science, IOS Press, pp.363-367.
- [84] Zimmerman, J. E. (1977) SQUID instruments and shielding for low level magnetic measurements, *J. Appl. Phys.* **48**, 702-710.
- [85] Stroink, G., Blackford, B., Brown, B. and Horacek, M. (1981) Aluminum Shielded Room for Biomagnetic Measurements. *Rev. Sci. Instrum.* **52**(3), 463-468.
- [86] Vacuumschmelze GmbH, Hanau, Germany; Shielded Room model AK-3.
- [87] Amuneal Manufacturing Corp., 4737 Darrah Street, Philadelphia, PA 19124, USA.
- [88] Tokin Corporation, 6-7-1 Koriyama Tihakuku, Sendai-City, Miyagi-pref, 982, Japan.
- [89] Sullivan, G. W. and Flynn, E. R. (1987) Performance of the Los Alamos Shielded Room, in K. Atsumi et al (eds.), *Biomagnetism'87*, Tokyo Denki University Press, Tokyo, pp.486-489.
- [90] Erne, S. N., Hahlbohm, H.-D., Scheer, H. and Trontelj, Z. (1981) The Berlin Magnetically Shielded Room (BMSR) Section B - Performances, in S.N. Erne et al (eds.), *Biomagnetism*, Walter de Gruyter, Berlin and New York, pp.79-87.
- [91] Matsuba, H., Shintomi, K., Yahara, A., Imai, K., Irisawa, D., and Matsuda, M. (1997) High Tc superconducting shielded biomagnetometer system, in C. Aine et al (eds.), *Biomag96: Advances in Biomagnetism Research*, Springer-Verlag, in press.
- [92] Matsumoto, K., Yamagishi, Y., Wakusawa, A., Noda, T., Fujioka, K., and Kuraoka, Y. (1992) SQUID based active shield for biomagnetic measurement, in M. Hoke et al (eds.), *Biomagnetism: Clinical Aspects*, Elsevier Science Publishers B.V., Excerpta Medica, Amsterdam, London, New York, Tokyo, pp.857-861.
- [93] Malmivuo, J., Lekkala, J., Kontro, P., Suomaa, I., and Vihinen, H. (1987) Improvement of the properties of an eddy current magnetic shield with active compensation, *J. Phys. E: Sci. Instrum.* **20**, 151-164.
- [94] Kelha, V.O., Pukki, J.M., Peltonen, R.S., Penttinen, V.J., Ilmoniemi, R.J., and Heino, J.J. (1982) Design, construction, and performance of a large volume magnetic shield, *IEEE Trans. Magn.* **18**, 260-270.
- [95] ter Brake, H.J.M., Wieringa, H.J., and Rogalla, H. (1991) Improvement of the performance of a  $\mu$ -metal magnetically shielded room by means of active compensation, *Meas. Sci. Techn.* **2**, 596-601.
- [96] ter Brake, H.J.M., Huonker, R., and Rogalla, H. (1993) New results in active noise compensation for magnetically shielded rooms, *Meas. Sci. Techn.* **4**, 1370-1375.
- [97] Vrba, J. and McCubbin, J. (1983) First-gradient balancing of higher-order gradiometers, *Il Nuovo Cimento* **2D**, 142-152.
- [98] Vrba, J., Fife, A.A., and Burbank, M.B. (1982) Spatial discrimination in SQUID gradiometers and third-order gradiometer performance, *Can. J. Phys.* **60**, 1060-1073.
- [99] Vrba, J., McCubbin, J., Lee, S., Fife, A.A., and Burbank, M.B. (1989) Noise cancellation in biomagnetometers, in S.J. Williamson et al (eds.), *Advances in Biomagnetism*, Plenum Press, New York and London, pp.733-736.
- [100] Vrba, J., Haid, G., Lee, S., Taylor, B., Fife, A.A., Kubik, P., McCubbin, J., and Burbank, M.B. (1991) Biomagnetometers for unshielded and well shielded environments, *Clin. Phys. Physiol. Meas.* **12 B**, 81-86.

- [101] Bruno, A. C., Dolce, C. S., Soares, S. D. and Ribeiro, P. C. (1989) Spatial Fourier Technique for Calibrating Gradiometers, in S.J. Williamson et al (eds.), *Advances in Biomagnetism*, Plenum Press, New York and London, pp.709-712.
- [102] Drung, D. (1991) Performance of an Electronic Gradiometer in Noisy Environments, in H. Koch and H. Lubbig (eds.), *SQUID'91, Superconducting Devices and their Applications*, Berlin, June 18-21, 1991, *Springer Proceedings in Physics*, **64**, pp.542-546.
- [103] Bendat, J. S. and Piersol, A. G. (1986) *Random Data*, John Wiley & Sons, New York, Chichester, Brisbane, Toronto, Singapore.
- [104] Uusitalo, M.A. and Ilmoniemi, R.J. (1997) Signal-Space Projection method for separating MEG or EEG into components, *Med. & Biol. Eng. & Comp.* **35**, 135-140.
- [105] Huottilainen, M., Ilmoniemi, R.J., Tiitinen, H., Lavikainen, J., Alho, K., Kajola, M., Simola, J., and Naatanen, R. (1995) The projection method in removing eye-blink artefacts from multichannel MEG measurements, in C. Baumgartner et al (eds.), *Biomagnetism: Fundamental Research and Clinical Applications*, Elsevier Science, IOS Press, pp.363-367.
- [106] Parker, L.R. (1994) *Geophysical inverse theory*, Princeton University Press, Princeton, NJ.
- [107] Robinson, S.E. and Rose, D.F. (1992) Current source image estimation by spatially filtered MEG, in M. Hoke et al (eds.), *Biomagnetism: Clinical Aspects*, Elsevier Science Publishers B.V., Excerpta Medica, Amsterdam, London, New York, Tokyo, pp.761-765.
- [108] Robinson, S.E. (1989) Theory and properties of lead field synthesis analysis, in S.J. Williamson et al (eds.), *Advances in Biomagnetism*, Plenum Press, New York and London, pp.599-602.
- [109] Vrba, J. and McKay, J. (1997) Character and acquisition of multichannel biomagnetic data, abstract submitted to ISEC'97, June 25-28, Berlin, Germany.
- [110] Vrba, J., Fife, A.A., Burbank, M.B. (1981) Digital SQUID electronics in geophysical applications, in H. Weinstock and W.C. Overton, (eds.), *SQUID Applications to Geophysics*, Tulsa, Oklahoma: The Society of Exploration Geophysicists, pp.31-34.
- [111] Lutkenhoner, B. (1996) Current dipole localization with an ideal magnetometer system, *IEEE Trans. Biomed. Eng.* **43**, 1049-1061.
- [112] Matsuba, H., Vrba, J., and Cheung, T. (1997) Current Dipole Localization Error as a Function of System Noise and the Number of Sensors, in C. Aine et al (eds.), *Biomag96: Advances in Biomagnetism Research*, Springer-Verlag, in press.
- [113] Vrba, J., Cheung, T., and Robinson, S. (1996) Simulation of dipole reconstruction accuracy, *CI-683-1096*, unpublished CTF internal report.
- [114] Vrba, J. (1997) Baseline optimization for noise cancellation systems. Submitted to *IEEE-EMBS*, Chicago, Oct 30 to Nov 2.
- [115] Vrba, J., Taylor, B., Cheung, T., Fife, A.A., Haid, G., Kubik, P.R., Lee, S., McCubbin, J., and Burbank, M. (1995) Noise cancellation by a whole-cortex SQUID MEG system, *IEEE Trans. Appl. Supercond.* **5**, 2118-2123.
- [116] ter Brake, H.J.M., Sensing-coil optimization based on signal-to-noise ratio, *private communication*. The paper was presented at the New York Biomagnetism Conference 1989, but was not published.
- [117] Kempainen, P.K. and Ilmoniemi, R.J. (1989) Channel capacity of multichannel magnetometers, in S.J. Williamson et al (eds.), *Advances in Biomagnetism*, Plenum Press, New York and London, pp.635-638.
- [118] Kuc, R. (1996) Magnetometer spacing criterion for biomagnetic source current imaging, *IEEE Trans. Biomed. Eng.* **43**, 1125-1127.
- [119] Ahonen, A.I., Hamalainen, M.S., Ilmoniemi, R.J., Kajola, M.J., Knuutila, J.E.T., Simola, J.T., and Vilkmann, V.A. (1993) Sampling theory for neuromagnetic detector arrays, *IEEE Trans. Biomed. Eng.* **40**, 859-869.
- [120] Polhemus Inc., 1 Hercules drive, PO Box 560, Colchester, VT, 05446, USA.
- [121] Bamidis, P.D. and Ioannides, A.A. (1997) Combination of point and surface matching techniques for accurate registration of MEG and MRI, in Aine, C., Okada, Y., Stroink, G., Swithenby, S., and Wood, C. (eds.), *Biomag96: Advances in Biomagnetism Research*, Springer-Verlag, in press.
- [122] Abraham-Fuchs, K., Lindner, L., Wegener, P., Nestel, F., and Schneider, S. (1991) Fusion of biomagnetism with MRI or CT images by contour-fitting, *Biomed. Eng.* **36** (Suppl), 88-89.
- [123] Kober, H., Grummich, P., and Vieth, J. (1995) Fit of the digitized head surface with the surface reconstructed from MRI-tomography, in C. Baumgartner et al (eds.), *Biomagnetism: Fundamental Research and Clinical Applications*, Elsevier Science, IOS Press, pp.309-312.
- [124] Nakasato, N., Fujita, S., Matani, A., Tamura, I., Fujiwara, S., and Yoshimoto, T. (1995) Clinical application of the whole head MEG: auditory evoked response in patients with intracranial structural lesions, in C. Baumgartner et al (eds.), *Biomagnetism: Fundamental Research and Clinical Applications*, Elsevier Science, IOS Press, pp.186-190.
- [125] Robinson, S.E., Weinberg, H., Cheyne, D., Vrba, J., and Jantzen, K.J. (1997) Functional imaging of cerebellar activity during a simple differential reading task by whole-head magnetoencephalography, 3rd International Conference on Functional Mapping of the Human Brain, Copenhagen, May 19-23, 1997.
- [126] Rabiner, L.R. and Gold, B. (1975) *Theory and application of digital signal processing*, Prentice-Hall, Inc., Englewood Cliffs, New Jersey.

